

①

June 1990

THESIS/~~DISSERTATION~~

Entry Vehicle Performance Analysis and Atmospheric  
Guidance Algorithm for Precision Landing on Mars

Todd A. Dierlam

AFIT Student Attending: Massachusetts Institute of  
Technology

AFIT/CI/CIA- 90-131

AFIT/CI  
Wright-Patterson AFB OH 45433-6583

Approved for Public Release IAW 190-1  
Distributed Unlimited  
ERNEST A. HAYGOOD, 1st Lt, USAF  
Executive Officer

DTIC  
ELECTE  
FEB 07 1991  
S B D

AD-A231 585

AD-A231 585

**CSDL-T-1053**  
**ENTRY VEHICLE PERFORMANCE  
ANALYSIS AND ATMOSPHERIC GUIDANCE  
ALGORITHM FOR PRECISION LANDING ON MARS**

by

**Todd A. Dierlam**

**June 1990**

**Master of Science Thesis  
Massachusetts Institute of Technology**

**Approved for public release;  
distribution unlimited.**

NASA-JSC 6/11/90



**The Charles Stark Draper Laboratory, Inc.**

555 Technology Square  
Cambridge, Massachusetts 02139

91 2 06 098

Entry Vehicle Performance Analysis  
and Atmospheric Guidance Algorithm  
for Precision Landing on Mars

by

2Lt Todd Allen Dierlam  
B.S.A.E., United States Air Force Academy  
(1988)

Submitted in Partial Fulfillment  
of the Requirements for the  
Degree of  
Master of Science  
in Aeronautics and Astronautics  
at the  
Massachusetts Institute of Technology  
June, 1990

© Todd Allen Dierlam, 1990

Signature of Author Todd A. Dierlam  
Department of Aeronautics and Astronautics  
June, 1990

Certified by Richard H. Battin  
Professor Richard H. Battin  
Department of Aeronautics and Astronautics  
Thesis Supervisor

Certified by Kenneth M. Spratlin 5/16/90  
Kenneth M. Spratlin  
Technical Supervisor, CSDL

Accepted by \_\_\_\_\_  
Professor Harold Y. Wachman  
Chairman, Departmental Graduate Committee

# Entry Vehicle Performance Analysis and Atmospheric Guidance Algorithm for Precision Landing on Mars

by

2Lt Todd Allen Dierlam

Submitted to the  
Department of Aeronautics and Astronautics  
on May 18, 1990 in partial fulfillment of the requirements  
for the Degree of Master of Science.

## Abstract

Future missions to Mars may require pin-point landing precision, possibly on the order of tens of meters. The ability to reach a target while meeting a dynamic pressure constraint to ensure safe parachute deployment is complicated at Mars by low atmospheric density, high atmospheric uncertainty, and the desire to employ only bank angle control. The vehicle aerodynamic performance requirements and guidance necessary for a 0.5 to 1.5 lift-to-drag ratio vehicle to maximize the achievable footprint while meeting the constraints are examined.

A parametric study of the various factors related to entry vehicle performance in the Mars environment is undertaken to develop general vehicle aerodynamic design requirements. The combination of low lift-to-drag ratio and low atmospheric density at Mars results in a large phugoid motion involving the dynamic pressure which complicates trajectory control. Vehicle ballistic coefficient is demonstrated to be the predominant characteristic affecting final dynamic pressure. Additionally, a speed brake is shown to be ineffective at reducing the final dynamic pressure.

An adaptive precision entry atmospheric guidance scheme is presented. The guidance uses a numeric predictor-corrector algorithm to control downrange, an azimuth controller to govern crossrange, and an analytic control law to reduce the final dynamic pressure. Guidance performance is tested against a variety of dispersions, and the results from selected test cases are presented. Precision entry using bank angle control only is demonstrated to be feasible at Mars.

**Thesis Supervisor:** Dr. Richard H. Battin

**Title:** Adjunct Professor of Aeronautics and Astronautics

**Technical Supervisor:** Kenneth M. Spratlin

**Title:** Section Chief, The Charles Stark Draper Laboratory, Inc.

# Acknowledgements

I'm truly grateful for the opportunity I've had to work here at Draper and pursue my studies at MIT. It's been a growing time for me, academically as well as personally. Thank you Dr. Battin for your guidance and the contagious love of astrodynamics (and Gauss) that you have. Thanks also goes to Ken Spratlin for his technical advice, Doug Fuhry for his continuous support and patience, and the rest of those on the Draper staff who helped me along the way. I'm deeply indebted to all of you.

I've met so many friends here in Boston that it's going to be tough to leave. Here's to my officemate and all the late nights and weekends that we spent here at the Lab. It wouldn't have been the same without you, Tony. I'm glad we got through this together. Thanks also goes to Craig Niiya for his wisdom, friendship, and willingness to give of himself, and to Jesse Gossner for his listening and understanding of a naive second lieutenant.

Next, I'd like to express my gratitude to the Park Street gang for seeing me through this and for being a special part of my stay in Boston. I'm not the same person that I was when I came here because of all of you. I'd also like to let my three roommates, Bill, Tom, and John, know that the last two years with them have been a lot of fun, and I'd do it all over again. (Not the school, but the living arrangement!)

Dad, Mom, Scott, Tish, Bob, Aces, and the Baby— thanks for being family, and just being there. I've been blessed to have your love and support through the years. Especially Dad, thanks for all your love and concern. I probably would have worried even more if I didn't have you worrying for me.

And to Tracy Bradley, without whom, something will be missing in my life. Thanks for trying to understand me during these tough times and for your willingness to so freely share with me. I love you.

ORIN  
RECEIVED

Accession For	
NTIS GRA&I	<input checked="" type="checkbox"/>
DTIC TAB	<input type="checkbox"/>
Unannounced	<input type="checkbox"/>
Justification	
By _____	
Distribution/	
Availability Codes	
Dist	Avail and/or Special
A-1	

This report was prepared at The Charles Stark Draper Laboratory, Inc. under NASA Contract NAS9-18147.

Publication of this report does not constitute approval by the Draper Laboratory or the sponsoring agency of the findings or conclusions contained herein. It is published for the exchange and stimulation of ideas.

I hereby assign my copyright of this thesis to The Charles Stark Draper Laboratory, Inc., Cambridge, Massachusetts.

---

Todd A. Dierlam

Permission is hereby granted by The Charles Stark Draper Laboratory, Inc., to the Massachusetts Institute of Technology to reproduce any or all of this thesis.

# Contents

<b>1</b>	<b>Introduction</b>	<b>21</b>
1.1	Mission Overview . . . . .	22
1.2	Entry Requirements . . . . .	24
1.3	Trajectory Control . . . . .	27
1.4	Thesis Overview . . . . .	30
<b>2</b>	<b>Simulation</b>	<b>33</b>
2.1	Introduction . . . . .	33
2.2	Mars Environment Models . . . . .	34
2.3	Entry Vehicle Models . . . . .	41
<b>3</b>	<b>Entry Vehicle Capabilities</b>	<b>45</b>
3.1	Introduction . . . . .	45
3.2	Method of Performance Analysis . . . . .	45
3.3	General Performance . . . . .	52
3.3.1	Ranging Capability . . . . .	52
3.3.2	Final Dynamic Pressure . . . . .	59

3.4	Vehicle M Performance . . . . .	68
3.5	Divert Capability . . . . .	77
<b>4</b>	<b>Guidance Design</b>	<b>81</b>
4.1	Previous Work . . . . .	81
4.2	Guidance Scheme . . . . .	87
4.3	Downrange Control . . . . .	94
4.3.1	Corrector . . . . .	96
4.3.2	Predictor . . . . .	100
4.4	Crossrange Control . . . . .	110
4.5	Dynamic Pressure Control . . . . .	113
4.5.1	Gain Determination . . . . .	115
<b>5</b>	<b>Guidance Performance</b>	<b>121</b>
5.1	Nominal Performance . . . . .	122
5.2	Dispersed Performance . . . . .	124
5.3	Speed Brake Performance . . . . .	150
5.4	Dynamic Pressure Control Performance . . . . .	151
5.5	Estimator Performance . . . . .	153
<b>6</b>	<b>Conclusions</b>	<b>161</b>
6.1	Summary of Results . . . . .	161
6.2	Future Research . . . . .	164

# List of Figures

1.1	Range of Entry Vehicle Configurations . . . . .	28
1.2	Typical Biconic Vehicle . . . . .	29
2.1	Comparison of Mars and Earth Atmospheric Densities . . . . .	36
2.2	Mars Cool-Low and Warm-High Density Variation . . . . .	38
2.3	Viking 1 Profile Density Variation . . . . .	39
2.4	Viking 2 Profile Density Variation . . . . .	40
3.1	Comparison of Optimal Entry Bank Profiles . . . . .	48
3.2	Shuttle Optimal Bank Profile . . . . .	49
3.3	Linear Bank Profile . . . . .	51
3.4	Maximum Ranging Capability: Effect of L/D . . . . .	53
3.5	Maximum Ranging Capability: Effect of Ballistic Coefficient . . . . .	55
3.6	Maximum Ranging Capability: Effect of Entry Flight Path Angle . . . . .	56
3.7	Maximum Ranging Capability: Effect of Constant Density Biases . . . . .	58
3.8	Typical Dynamic Pressure Response During Entry . . . . .	60
3.9	Final Dynamic Pressure Range: Effect of L/D . . . . .	62

3.10	Final Dynamic Pressure Range: Effect of Ballistic Coefficient . . . . .	63
3.11	Final Dynamic Pressure: Effect of Ballistic Coefficient for a Particular Bank Profile . . . . .	64
3.12	Final Dynamic Pressure Range: Effect of Constant Density Biases . . .	66
3.13	Final Dynamic Pressure Range: Effect of Entry Flight Path Angle . . .	67
3.14	Vehicle M Lift Coefficient Curve . . . . .	69
3.15	Vehicle M Drag Coefficient Curve . . . . .	70
3.16	Vehicle M L/D Curve . . . . .	71
3.17	Vehicle M: Ranging Performance Comparison of Two Angles of Attack — Front and Back Side of L/D Curve . . . . .	73
3.18	Vehicle M: Effect of Angle of Attack on Final Dynamic Pressure . . .	74
3.19	Vehicle M: Effect of Angle of Attack on Maximum Ranging Capability	76
3.20	Divert Capability . . . . .	79
4.1	Linear Bank Profile with Minimum Bank Angle . . . . .	91
4.2	Downrange Error Definition . . . . .	107
4.3	Azimuth Error Corridor . . . . .	111
5.1	Guidance Coverage of Open-Loop Footprint . . . . .	123
5.2	Closed-Loop Bank History for the Nominal Target — No Dispersion Case . . . . .	135
5.3	Closed-Loop Bank History for the Minimum Downrange Target — No Dispersion Case . . . . .	136

5.4	Closed-Loop Bank History for the Maximum Downrange Target — No Dispersion Case . . . . .	137
5.5	Closed-Loop Bank History for the Maximum Crossrange Target — No Dispersion Case . . . . .	138
5.6	Closed-Loop Azimuth Error History for the Nominal Target — No Dispersion Case . . . . .	139
5.7	Closed-Loop Azimuth Error History for the Minimum Downrange Target — No Dispersion Case . . . . .	140
5.8	Closed-Loop Azimuth Error History for the Maximum Downrange Target — No Dispersion Case . . . . .	141
5.9	Closed-Loop Azimuth Error History for the Maximum Crossrange Target — No Dispersion Case . . . . .	142
5.10	Closed-Loop Altitude History for the Nominal Target — No Dispersion Case . . . . .	143
5.11	Closed-Loop Velocity History for the Nominal Target — No Dispersion Case . . . . .	144
5.12	Closed-Loop Dynamic Pressure History for the Nominal Target — No Dispersion Case . . . . .	145
5.13	Closed-Loop Heating Rate History for the Nominal Target — No Dispersion Case . . . . .	146
5.14	Closed-Loop Crossrange History for the Nominal Target — No Dispersion Case . . . . .	147

5.15 Closed-Loop Downrange History for the Nominal Target — No Dispersion Case . . . . .	148
5.16 Closed-Loop Flight Path Angle History for the Nominal Target — No Dispersion Case . . . . .	149
5.17 Dynamic Pressure Response: Damped and Undamped Trajectories . .	152
5.18 Time Response of the Density Filter: No Wind Case . . . . .	155
5.19 Time Response of the L/D Filter: No Wind Case . . . . .	156
5.20 Time Response of the Density Filter: Wind Case . . . . .	159
5.21 Time Response of the L/D Filter: Wind Case . . . . .	160

# List of Tables

1.1	General Performance Requirements . . . . .	25
2.1	Mars Environment Constants . . . . .	35
3.1	Entry Interface Conditions . . . . .	46
5.1	Guidance I-Loads — Baseline Case (Nominal Target) . . . . .	122
5.2	Summary of Dispersions . . . . .	125
5.3	Nominal Target: Results of Dispersed Cases . . . . .	131
5.4	Minimum Downrange Target: Results of Dispersed Cases . . . . .	132
5.5	Maximum Downrange Target: Results of Dispersed Cases . . . . .	133
5.6	Maximum Crossrange Target: Results of Dispersed Cases . . . . .	134
5.7	Dynamic Pressure Controller Results . . . . .	151

# List of Symbols

Symbol	Description
$\vec{a}$	acceleration vector
$a$	magnitude of acceleration vector
AFE	Aeroassist Flight Experiment
$C_B$	vehicle ballistic coefficient
$C_D$	vehicle coefficient of lift
cg	center of gravity
$C_L$	vehicle coefficient of drag
$\cos \phi_d$	downrange lift fraction
$C_{m_0}$	vehicle pitching moment coefficient
CR	crossrange
DR	downrange
ERV	Entry Research Vehicle
$f_m$	Mars planet-flattening term
$g$	magnitude of gravitational acceleration
$g_{begin}$	minimum acceleration for guidance turn-on

$h$	altitude
$h^*$	altitude about which linearization occurs
$h_{cf rz}$	altitude for freezing corrector
$h_{cf st}$	altitude for fast corrector rate
$h_{pquit}$	altitude at which prediction is terminated
$h_{\Delta t, sml}$	altitude for small predictor step size
$hs$	atmospheric scale height
Hz	hertz
$\vec{i}$	unit vector
IMU	inertial measurement unit
$J_2$	gravitational perturbation
$k$	term used to define planet oblateness
$K$	term in dynamic pressure control equation
$K_{const}$	constant portion of term in dynamic pressure control equation
$K_{vary}$	variable portion of term in dynamic pressure control equation
$K_{\frac{L}{D}}$	lift-to-drag ratio scale factor
$K_{\bar{q}}$	gain on dynamic pressure error in $\bar{q}$ control equation
$K_{\bar{q}_f}$	fraction used to determine when dynamic pressure controller is used
$K_{\dot{\bar{q}}}$	gain on dynamic pressure rate error in $\bar{q}$ control equation
$K_{\rho}$	density scale factor
$K_1$	gain in first-order filter for density smoothing
$K_2$	gain in first-order filter for L/D smoothing

$L/D$	vehicle lift-to-drag ratio
$L_v$	magnitude of vertical lift
$m$	vehicle mass
$M_i^{NED}$	transformation matrix from inertial to North-East-Down coordinates
$M_i^{PF}$	transformation matrix from inertial to planet-fixed coordinates
MRSR	Mars Rover Sample Return
NASA	National Aeronautics and Space Administration
$Q$	vehicle heat load
$\dot{Q}$	vehicle heating rate
$\bar{q}$	dynamic pressure
$\bar{q}_f$	final dynamic pressure
$\vec{r}$	inertial position vector
$r$	magnitude of inertial position vector
$r_{eq}$	planet equatorial radius
$r_g$	planet gravitational radius
$r_{pl}$	planet polar radius
$R_{fst}$	fast corrector execution rate
$R_{slw}$	slow corrector execution rate
$R_N$	vehicle nose radius
$S$	aerodynamic reference area
$S_\phi$	sign of current bank angle
$t$	time

$t_{ep}$	epoch time
$\vec{v}$	inertial velocity vector
$v$	magnitude of inertial velocity vector
$\vec{v}_{rel}$	planet-relative velocity vector
$v_{rel}$	magnitude of planet-relative velocity vector
$V_{damp}$	velocity below which dynamic pressure damping occurs
$V_{\Delta\phi_{lim}}$	velocity at which incremental bank limiting begins
$V_{\psi_{errmax}}$	velocity for maximum allowable heading error
$V_{\psi_{errmin}}$	velocity for minimum allowable heading error
W000	constant northerly wind
W090	constant easterly wind
W180	constant southerly wind
W270	constant westerly wind
$z$	geocentric colatitude of the position vector
$\alpha$	angle of attack
$\alpha_t$	trim angle of attack
$\delta$	small incremental change
$\delta(\cos\phi_{\bar{q}})$	change in lift fraction due to dynamic pressure control
$\Delta$	incremental change
$\Delta\phi_{lim}$	incremental limit in bank angle
$\gamma$	flight path angle

$\lambda$	longitude
$\mu_m$	Mars gravitational parameter
$\omega_m$	Mars angular rotation rate
$\omega_n$	natural frequency of dynamic pressure control response
$\phi$	bank angle
$\phi_{cmd}$	commanded bank angle
$\phi_d$	downrange bank angle
$\phi_{des}$	desired bank angle
$\phi_{\bar{q}}$	dynamic pressure bank angle
$\phi_{min}$	minimum bank angle
$\psi$	azimuth or heading angle
$\psi_{errmax}$	maximum allowable heading error
$\psi_{errmin}$	minimum allowable heading error
$\rho$	atmospheric density
$\rho_{sle}$	Earth sea level density
$\sigma$	standard deviation
$\tau$	time constant of filter
$\zeta$	damping ratio of dynamic pressure control response

## Subscripts

aero	aerodynamic
cmd	command
des	desired
drag	atmospheric drag term
e	earth
e	error
ei	entry interface
eq	equatorial
err	error
f	final
fst	fast
g	gravitational
gc	geocentric
gd	geodetic
I	inertial
IMU	inertial measurement unit
lift	aerodynamic lift term
lim	limiting value
L/D	lift-to-drag ratio
m	Mars

max	maximum
min	minimum
NED	north-east-down coordinate system
nom	nominal or standard
p	predicted
PF	planet-fixed coordinate system
pl	polar
⊥	perpendicular
pert	perturbed
pole	direction of north pole
$\bar{q}$	dynamic pressure
s	surface
sl	sea level
slw	slow
t	trim value
tgt	target
tot	total
vlift	vertical aerodynamic lift term
°	initial
$\rho$	atmospheric density

## Superscripts

/	previous value
^	estimate or unit value
'	first derivative
''	second derivative
+	thick atmosphere model, also latest value
-	thin atmosphere model, also previous value
cl	cool-low atmosphere model
es	early shear atmosphere model
ls	late shear atmosphere model
wh	warm-high atmosphere model
v1	Viking 1 atmosphere model
v2	Viking 2 atmosphere model



# Chapter 1

## Introduction

Future exploratory missions to the surface of Mars will require precise control of the terminal landing conditions. Current studies for a robotic mission, such as the Mars Rover Sample Return (MRSR) study [1], levy requirements of 100 meter accuracy in order to land in geologically interesting areas or to avoid hazards that have been detected from orbit. Later missions to Mars will most likely involve the emplacement of manned habitats and their subsequent resupply. The landing accuracy required for these missions will be on the order of 30 meters [2].

Precision entry and landing, such as the Space Shuttle frequently performs at Earth, has never been done at Mars. Relatively little work has been done to define vehicle and guidance requirements for such a mission. The task is complicated at Mars by a less dense atmosphere, the greater uncertainty in environmental conditions, and the need for a high degree of autonomy. This thesis attempts to define basic vehicle performance requirements for achieving entry and precision landing, and then presents a guidance algorithm that maximizes the achievable footprint for a given vehicle while

minimizing the landing errors.

In support of these goals, this chapter presents background regarding entry and formulates the entry problem. Section 1.1 discusses the different entry options available and provides an overview of the general entry mission. Given a specific mission, Section 1.2 then introduces the constraints and requirements which define a successful entry. There are several possible methods of controlling the vehicle in order to achieve these mission requirements. Section 1.3 discusses these possibilities and presents the chosen method of control. With the specific entry constraints and controls defined, the approach used to solve the entry problem and an overview of the thesis are contained in Section 1.4.

## 1.1 Mission Overview

The exploration of Mars has been of interest to man for many years. Current interest revolves around the human exploration of Mars, and President Bush's Lunar/Mars Exploration Initiative provides the framework by which this will take place. The plan calls for a series of missions which begins with unmanned probes, leads to the initial manned landing, and eventually achieves a permanent presence. However, many technological issues must be addressed before these missions become reality. Precision entry and landing is one of these issues.

Because little work has been done in this arena, there are no definite mission profiles to work with. In general, there are two ways that a vehicle on an interplanetary trajectory to Mars can reach the surface. The vehicle can enter directly from the hy-

peribolic approach orbit, or it can capture into a lower energy orbit and then deorbit to the surface. The capture approach uses more fuel, but it has several advantages. Besides reducing the entry velocity which lowers the heating rates and g-loads, this approach allows time for on-orbit determination of a safe landing site. This may be necessary for the early missions. Once landing sites and base camps are established later in the program, the capture approach may still be desirable based on mission planning considerations.

Once the vehicle reaches the atmosphere of Mars, there are two general classes of entry trajectories which can be flown. The trajectory can be lifting (employing a vehicle which creates aerodynamic lift) or non-lifting (using a vehicle which develops no lift). The non-lifting trajectory is generally shorter, subject to smaller dispersions, and thus more accurate. The original Minuteman Intercontinental Ballistic Missile warheads used this type of trajectory. However, the non-lifting trajectory results in entry and terminal conditions which are very severe, and it is not feasible for manned flight. The lifting entry trajectory, as used in the Apollo, Shuttle, and Viking programs, generally moderates the entry conditions at the cost of being more sensitive to dispersions. A larger lifting capacity allows greater reductions in the g-loads and final velocities by increasing control over the trajectory.

Although entry at Mars has been successfully demonstrated by the American Viking landers [3] and the Soviet probe Mars 6 [4], these entries were not precision entries by any means. The  $3\sigma$  landing error ellipse for the low-lift, open-loop guidance, Viking 1 trajectory was on the order of 120 km x 60 km [3]. In order to provide a low

terminal velocity, allow for precise targeting, and provide a more benign environment during entry, a guided mid-to-high lift-to-drag ratio (L/D) entry vehicle with the capability to significantly shape the trajectory is desired.

## 1.2 Entry Requirements

One landing scenario studied under the MRSR [1] mission includes a three phase profile for reducing the vehicle velocity while actively guiding to a landing site. This is the scenario assumed in this study, and the three successive phases are,

- Entry Phase
- Parachute Phase
- Powered Descent Phase

The entry phase begins once atmospheric forces start to affect the trajectory. During this stage, the vehicle uses its aerodynamic capabilities to fly towards the target while decelerating from orbital to near subsonic velocities. The entry phase ends when the vehicle deploys its parachute at some predetermined altitude or combination of altitude and velocity. The parachute phase is very short compared to the approximately one-half hour entry phase and lasts only about a minute. The purpose of the parachute phase is to further reduce the vehicle velocity. After the parachute is jettisoned, the descent engines are turned on, and the powered descent phase begins. During this phase, the descent engines remove the vertical velocity from the trajectory and maneuver the vehicle horizontally to the landing site. This study focuses

on vehicle capabilities and guidance performance during the first phase—the entry stage.

A set of entry conditions from [5] is used to define the requirements in this study. These requirements are summarized in Table 1.1 and explained in the following paragraphs. These requirements, composed of final conditions and continuous constraints, are subject to change and, at this point in mission development, should be regarded only as typical guidelines.

**Table 1.1. General Performance Requirements**

<p><i>Terminal Conditions</i></p> <p>Down Range Error &lt; 1 km Cross Range Error &lt; 1 km Final Dynamic Pressure &lt; 1000 Pascals Final Flight Path Angle between <math>-20^\circ</math> and <math>0^\circ</math></p> <p><i>Continuous Constraints</i></p> <p>G-loads &lt; 3 Earth g's Low Heating Rate Large Crossrange Capability</p>
--

The landing accuracy expected of the complete entry and landing profile varies, depending upon the specific mission requirements, and may be as small as 30 m [2]. This pin-point landing capability drives guidance accuracy during the entry phase. Since dispersions due to wind are expected during the parachute phase, and current plans call for less than 2 km of lateral maneuvering capability during the powered

descent phase [1], the entry phase must guide the vehicle to within approximately 1 km of the desired parachute deployment location.

The final dynamic pressure limitation ensures the structural integrity of the parachute and limits the opening shock experienced by the vehicle. The parachute is also a driver behind the flight path angle requirement. The entry guidance must leave the vehicle on a nearly horizontal trajectory in order to minimize variations in actual parachute deployment altitude and allow sufficient time for parachute inflation and vehicle deceleration.

The g-load limitation is intended to provide comfortable entry conditions for astronauts who might be in a weakened state following a long journey from Earth, as well as to maintain vehicle integrity. The heating rate must be kept low in order to reduce thermal protection subsystem requirements.

An additional requirement for entry is a large crossrange capability. A crossrange capability is necessary to reach landing sites at a higher latitude than the inclination of the orbit, or to reach landing sites not in the orbital plane at the time of deorbit. A greater crossrange capability increases the number of landing sites which can be reached on a given orbital pass. This increases the number of deorbit opportunities to a given landing site and enhances mission flexibility. Downrange capability is not included as a constraint because all vehicles have some inherent downrange ability and downrange targeting is easily changed by delaying the time of the deorbit burn.

### 1.3 Trajectory Control

The two major forces which act on the vehicle during entry are gravitational and aerodynamic. In order to modify the trajectory and meet the constraints, the entry vehicle must be able to modulate the two components of the aerodynamic force, lift and drag.

Figure 1.1 from [6] displays a general range of possible entry vehicles and their relative lift-to-drag ratio,  $L/D$ , and ballistic coefficient,  $C_B$ . The higher  $L/D$  vehicles are desirable because they provide a higher degree of trajectory control, but they have sharp leading edges or wings for which there are substantial component packaging and mass penalties. The lower  $L/D$  vehicles have excellent mass and packaging characteristics, but their spherical and simple cone shapes do not generate enough lift to greatly modify the trajectory. In between these vehicles is the general class which is being considered for Mars entry—the lifting biconics.

A biconic vehicle, as shown in Figure 1.2 [7], is axially symmetric and generates lift by the displacement of the center of gravity from the axis of symmetry. The amount of lift generated can be controlled by varying the angle of attack,  $\alpha$ , and this can be accomplished through the use of a body flap, reaction control jets or by movement of the center of gravity. The body flap adds weight and complexity, while the reaction control jet solution is expensive from a fuel standpoint. Additionally, the shifting of the center of gravity is difficult to control. This makes it desirable to avoid controlling the magnitude of the lift with the angle of attack and to simply fly at the constant trim angle of attack,  $\alpha_t$ , determined by the placement of the center

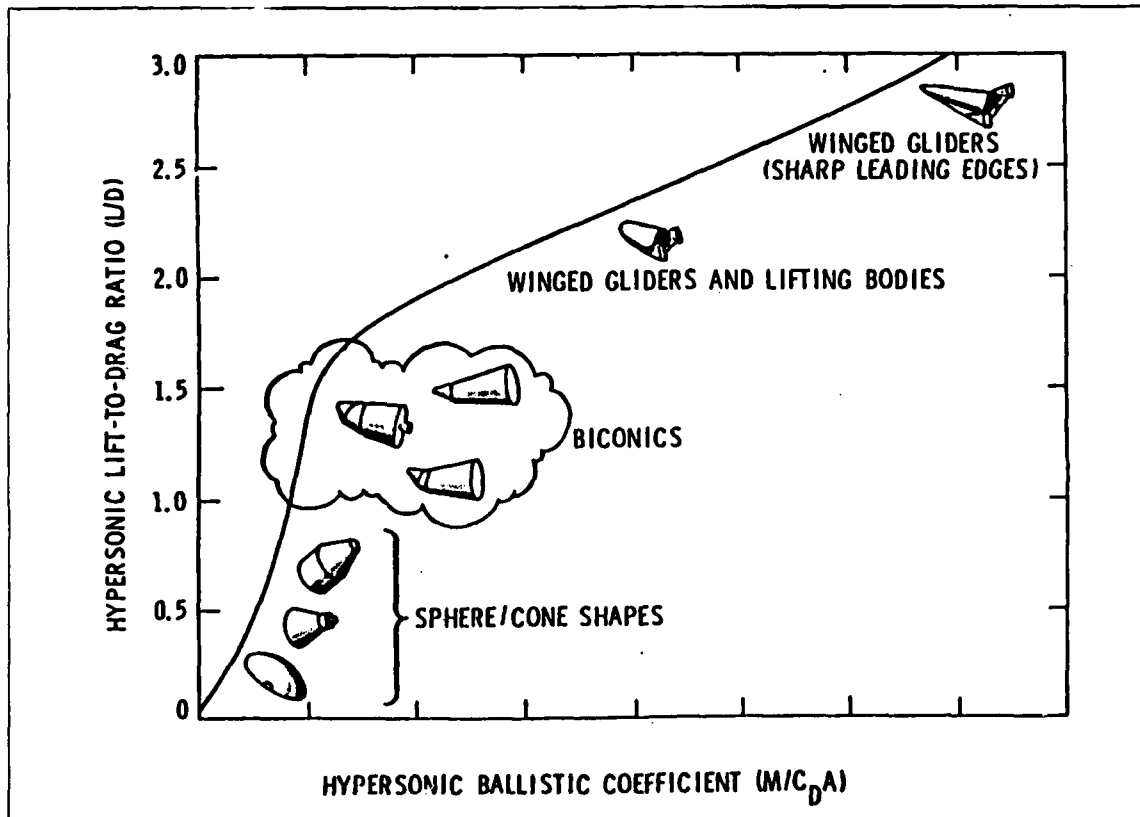


Figure 1.1. Range of Entry Vehicle Configurations

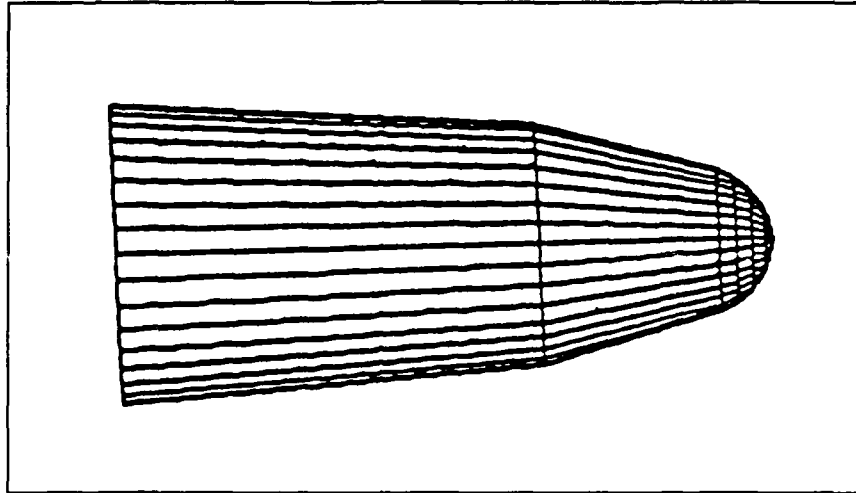


Figure 1.2. Typical Biconic Vehicle

of gravity.

If it is decided not to directly control the amount of lift being generated by modulating  $\alpha$ , it is still possible to control the trajectory of a biconic vehicle by simply varying the direction of the lift created. This is done by rotating the vehicle, and thus the lift vector, about the atmosphere-relative velocity vector, using reaction control jets or aerodynamic flaps. Reaction jets are the preferred method of controlling bank angle because they are effective when the aerodynamic forces are too low to generate the necessary rates, and because they will probably already be on the vehicle to provide control on-orbit. Thus, using only reaction control jets avoids an extra system.

The second component of the aerodynamic force, drag, can be directly affected by modulating the vehicle surface area or the coefficient of drag. A speed brake

can modify both of these, but at the cost of increased complexity. Drag control can be indirectly achieved by using the bank angle to vary the vertical lift, and thus the altitude and density at which the vehicle is flying. This form of drag control is desirable because it does not require structural additions to the vehicle.

Bank angle control alone allows control authority over both lift and drag during entry, without adding undue weight or complexity to the vehicle by requiring angle of attack control. Therefore, for the purposes of this report, the entry vehicle is assumed to be a biconic vehicle with bank angle control only. The extent of this authority and whether it is sufficient for precision landing is to be analyzed in this study.

## **1.4 Thesis Overview**

In analyzing the precision entry and landing problem, this thesis uses simulations of entry at Mars. The simulator and the models used to perform the presented analyses are described in Chapter 2.

After the development of the simulator, the thesis investigates two aspects of the precision entry and landing problem. The first aspect studied is the performance of entry vehicles in the Martian atmosphere. The ranging and maneuvering capabilities and final conditions, which are a result of various vehicle configurations, are analyzed in this portion of the thesis. From the performance, basic vehicle design requirements will be defined. Chapter 3 examines entry vehicle performance at Mars by parametrically varying vehicle and environment factors. The important parameters for achieving specific performance objectives are identified here, and this part serves

as an independent collection of knowledge concerning entry at Mars.

The second aspect of this thesis concerns the ability of a given entry vehicle to reach a target at Mars without violating the constraints. This part consists of the development and testing of a guidance algorithm for achieving precision entry at Mars. Chapter 4 describes previous research relevant to the guidance and then presents its design. The algorithm attempts to maximize the landing footprint for a given vehicle while controlling downrange, crossrange and final dynamic pressure. In Chapter 5, the performance of the guidance is stress-tested against severe dispersions in order to demonstrate the capabilities and disadvantages of using only bank angle control during entry.

The conclusions drawn from both parts of this thesis are summarized in Chapter 6. The lessons learned from this study are presented, and topics for future research are examined.



# Chapter 2

## Simulation

### 2.1 Introduction

This chapter describes the computer simulation and associated models used to perform the analyses presented in this thesis. Open-loop and closed-loop guided entry trajectories were generated using a three degree-of-freedom (3-DOF) digital simulator. The simulator was developed at The Charles Stark Draper Laboratory, Inc. using the MAC programming language on an IBM 3090 mainframe computer. Using a vehicle model and an environment model, the equations of motion are integrated in time from the prescribed initial conditions down to a designated terminal condition. The simulator uses a 4th-order Runge-Kutta integrator with a one second time step.

The simulator results are dependent upon the specific models used, and these models are described in the remainder of the chapter. Section 2.2 presents the Martian environment models used. Included in Section 2.2 are the physical characteristics of the planet, its atmosphere, and the expected dispersions. Descriptions of the two different methods of vehicle definition used and the associated vehicle dispersions are

contained in Section 2.3.

## 2.2 Mars Environment Models

The important parameters modeled in the environment are planet shape, gravity, atmospheric density, and winds. In the simulator, the vehicle altitude above the surface is determined relative to a reference ellipsoid which is defined by equatorial and polar planet radii. This same reference ellipsoid is used to determine a target vector based upon the landing site location on the planet surface. However, for the purpose of defining the final surface range between the vehicle and target, a spherical planet model is used. This is done for the sake of simplicity, and the error introduced is small because the planet is approximately circular for the short ranges considered. The expression which is used to model gravitational acceleration reflects the non-spherical nature of Mars by including  $J_2$  effects. The value of the gravitational constant,  $\mu_m$ , and other important physical constants used in the simulator are found in Table 2.1.

The atmospheric density at Mars varies with season, latitude and time of day, in addition to altitude. Despite these variations, it is important to have a standard density atmosphere with respect to altitude to serve as a reference. The simulator uses the revised Committee on Space Research (COSPAR) Northern Hemisphere mean Mars atmosphere, described in Reference [8], as a nominal density model. It is implemented as a table look-up. The Martian atmosphere is significantly less dense than Earth's atmosphere. As can be seen in the comparison between the Mars mean

**Table 2.1. Mars Environment Constants**

Gravitational Parameter	$\mu_m$	=	$4.28282804 \times 10^{13}$	$\frac{m^3}{s^2}$
Gravitational Radius	$r_g$	=	3393.4	km
Equatorial Radius	$r_{eq}$	=	3393.4	km
Polar Radius	$r_{pl}$	=	3375.8	km
Rotation Rate	$\omega_m$	=	$\frac{2\pi}{88643}$	$\frac{rad}{sec}$
Gravitational Perturbation	$J_2$	=	0.001965	

model and a standard Earth model in Figure 2.1 [8], Mars' surface density is only 1% of Earth's surface density. This lower density decreases the amount of aerodynamic forces produced by an entry vehicle at a given altitude and velocity, and thus reduces the ability of the vehicle to modify its trajectory to reach a target. Additionally, the decrease in drag causes difficulty in getting the vehicle to slow down.

In addition to planning for the lower density at Mars, entry designers must also deal with the lack of certainty concerning the actual density which will be encountered. Although data returned from Viking 1 and 2 and Mars 6 has greatly reduced the

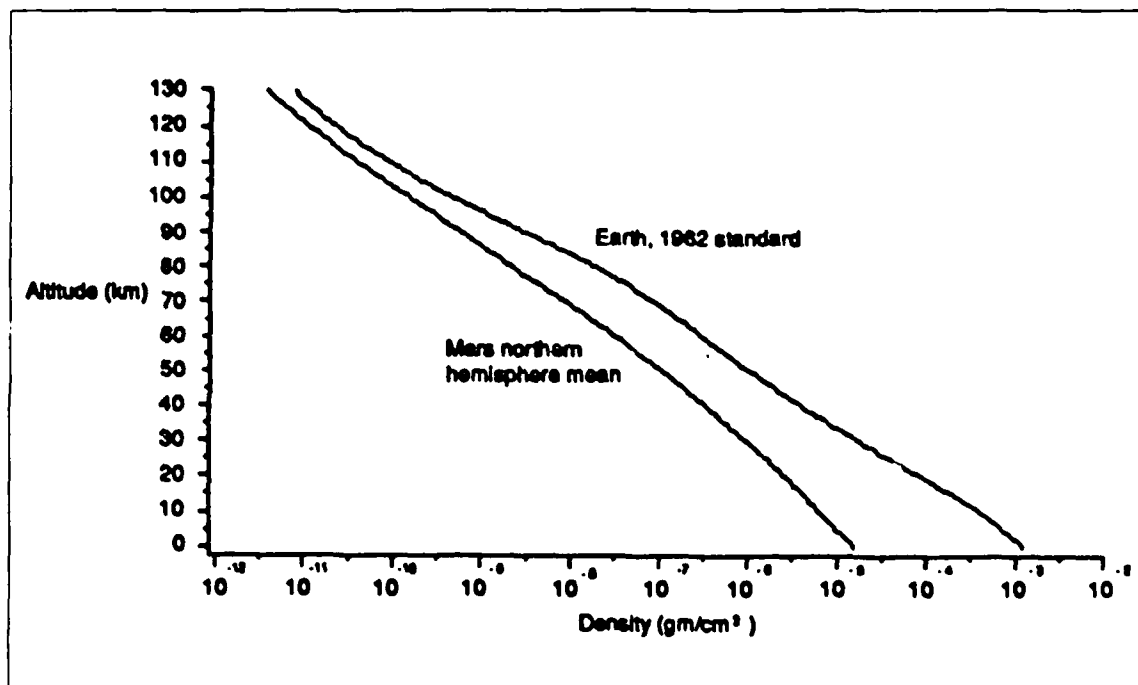


Figure 2.1. Comparison of Mars and Earth Atmospheric Densities

initial uncertainty in the density, these three missions constitute a limited data base, and the actual density could significantly vary from these estimates. Because of this, it is important to test vehicle and guidance performance over a large range of dispersed atmospheres. Additionally, the atmospheric density can experience large and unpredictable short-term variations from nominal value. It is important to test for these cases, too. The different profiles which will be used to analyze performance in off-nominal atmospheres are:

1. Revised COSPAR Cool-Low Model
2. Revised COSPAR Warm-High Model
3. Viking 1 Entry Trajectory Data
4. Viking 2 Entry Trajectory Data
5. Constant Density Bias—50% Thin Northern Hemisphere Mean Model
6. Constant Density Bias—100% Thick Northern Hemisphere Mean Model
7. Early Density Shear—25% Thin Northern Hemisphere Mean Model
8. Late Density Shear—10% Thin Northern Hemisphere Mean Model

The deviation of the Cool-Low and Warm-High models from the nominal density is shown in Figure 2.2, while the deviation of the Viking 1 and 2 profiles from nominal is contained in Figures 2.3 and 2.4. All of these figures are from Reference [8].

The density biases and shears are based on the Northern Hemisphere mean model. The early shear is defined by a 25% thin atmosphere from entry interface until 50 kilometers altitude—at which time the density abruptly returns to nominal. The late shear consists of a nominal atmosphere until 25 kilometers altitude where the density

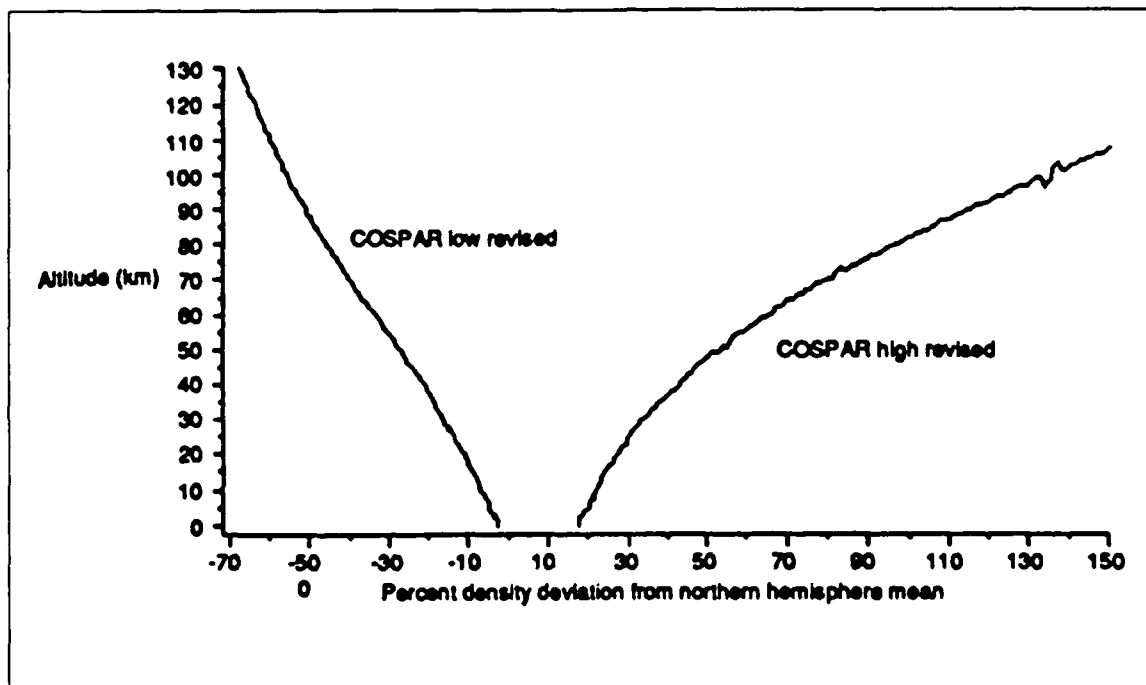


Figure 2.2. Mars Cool-Low and Warm-High Density Variation

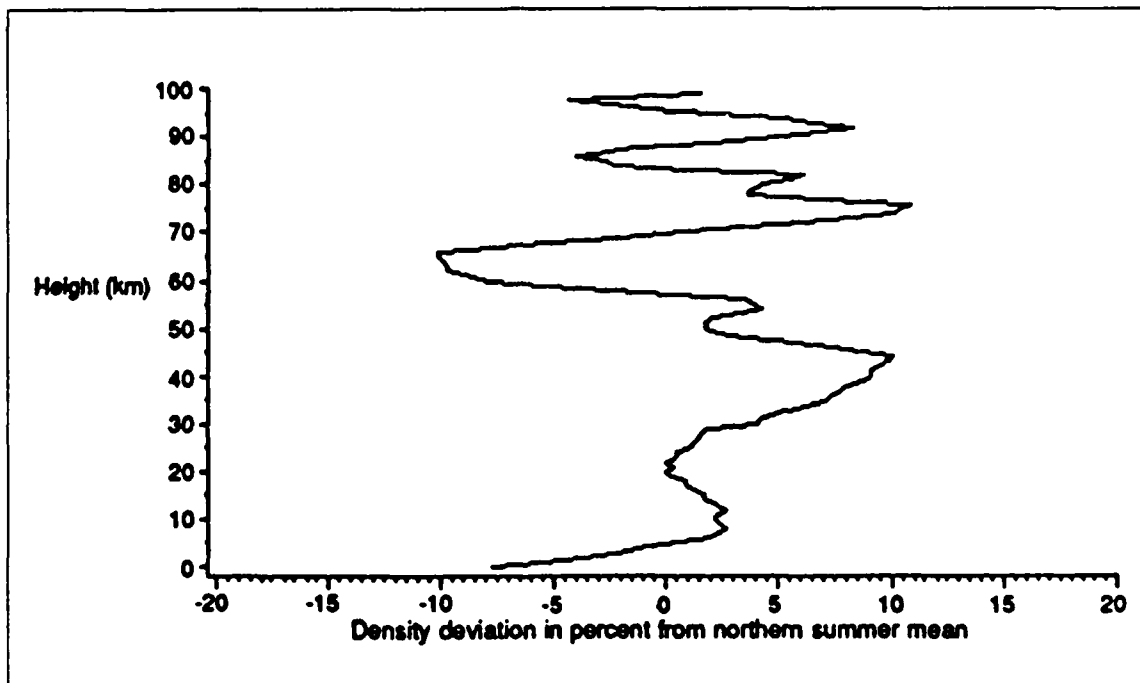


Figure 2.3. Viking 1 Profile Density Variation

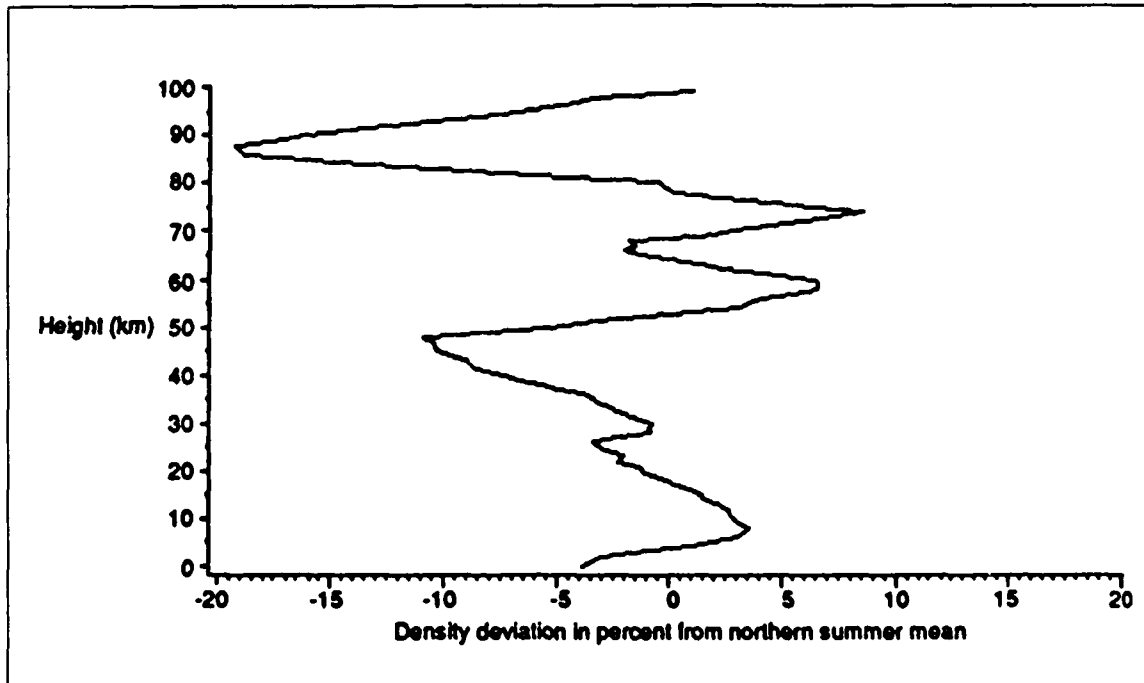


Figure 2.4. Viking 2 Profile Density Variation

becomes 10% thin and remains so down to the surface. The late shear is smaller percentage-wise than the early shear because larger shears are less likely at lower altitudes. However, the late shear has the potential to cause greater errors because the vehicle has little time remaining to correct for this dispersion.

For the nominal entry case, the entire atmosphere is assumed to be rotating uniformly with Mars, and no planet-relative winds are included. However, winds can be an important factor in vehicle performance, and dispersed wind test cases consisting of a constant 50 m/s wind from each of the four cardinal directions are used. The 50 m/s value was chosen as a reasonable value compromising between the high speed jet stream winds which the vehicle experiences for a brief period of time and the lower speed winds generally found elsewhere. Reference [8] indicates that for every season on Mars, the surface winds recorded by the Viking landers were less than 17 m/s ninety-nine percent of the time. Error analysis of the Viking 1 trajectory data indicates that the error due to wind is attributable to the equivalent of a constant 30 m/s wind from the east [3].

## 2.3 Entry Vehicle Models

Because there are two different studies described in this report—one parametrically exploring vehicle performance capabilities and the other examining guidance performance—it was desirable to employ two separate methods of defining the entry vehicle. One method defines a generic biconic lifting entry vehicle based solely on constant values of lift-to-drag ratio and ballistic coefficient. The other method uses

vehicle mass, surface reference area, and the aerodynamic coefficients,  $C_L$  and  $C_D$ , as a function of angle of attack for a specific configuration to distinguish the vehicle.

$L/D$  and  $C_B$  fully define the vehicle aerodynamic characteristics for the translational equations of motion and are therefore the most important parameters in assessing vehicle capability. The first method of vehicle definition is useful because it facilitates the parametric examination of different vehicle classes without access to specific configuration data. The general entry trajectory studies in Chapter 3 are performed using this generic vehicle. The second method requires more specific configuration information, but is useful in examining the performance that can be extracted from a particular vehicle. This method of vehicle definition is used later in Chapter 3 for just this purpose. The guidance performance analysis in Chapter 5 also uses this method of vehicle definition.

In order to realistically assess the guidance performance, the bank angle control response was modeled as a phase plane having bank rate and acceleration limits. In this model, the maximum roll rate was 20 degrees per second, and the maximum roll acceleration was 5 degrees per second squared.

Although the aerodynamic characteristics of the entry vehicle will be analytically and empirically predicted, the small errors expected in this knowledge can cause significant performance differences. The Viking lander axial force coefficients were only in error by approximately 1%, and this resulted in a 6 to 10 km range error [3]. If the Viking trajectories had been longer, as will future precision landing trajectories, the range error would have grown much larger. Since the entry flight regime is beyond

that of current wind tunnels, and computational fluid dynamics research has not sufficiently advanced to allow accurate prediction, there will be errors. There will also be a large uncertainty in the trim angle of attack, and this will induce a significant known L/D dispersion. Therefore,  $\pm 10\%$  dispersions in lift and drag coefficients will be considered.

The vehicle heating rate during entry is modeled by an empirical formula found in [9]. The equation estimates the stagnation heating rate on the nose of the entry vehicle, in W/sq cm, as,

$$\dot{Q} = \frac{542.01}{\sqrt{R_N}} \sqrt{\frac{\rho}{\rho_{sl_e}}} \left( \frac{v_{rel}}{3048} \right)^{3.5} \quad (2.1)$$

where  $R_N$  is the vehicle nose radius in units of meters and  $v_{rel}$  is in units of m/s. The values used in the simulator for the constants in the equation are,

$$R_N = 0.3048 \text{ m}$$

and

$$\rho_{sl_e} = 1.226 \text{ kg/m}^3$$

The integrated heat load during entry is then computed as the time integral of the heating rate equation as,

$$Q(t) = \int_0^t \dot{Q}(\tau) d\tau \quad (2.2)$$



# Chapter 3

## Entry Vehicle Capabilities

### 3.1 Introduction

The ability to land with pin-point precision is highly dependent on the entry vehicle capabilities. This chapter examines lifting vehicle entry trajectories at Mars and looks at the effect of different vehicle and environmental factors on performance. Section 3.2 describes how the studies in this chapter were performed. Section 3.3 examines the entry ranging and final dynamic pressure performance over a range of vehicle configurations, while Section 3.4 investigates the same performance for a specific vehicle. The last section examines the ability of a vehicle to divert late in the Mars entry trajectory in order to reach an updated target location.

### 3.2 Method of Performance Analysis

The performance criteria used in these evaluations are downrange and crossrange-ranging capability- and final dynamic pressure because they are the primary entry constraints and will be used as a basis of guidance design requirements. Downrange is

**Table 3.1.** Entry Interface Conditions

Altitude	125.0	km
Inertial Velocity	3550.0	m/s
Flight Path Angle	-3.3	deg
Latitude	0.0	deg
Longitude	0.0	deg
Heading	90.0	deg
Vacuum Apoapsis	500.0	km
Vacuum Periapsis	5.0	km

measured from the initial position vector to the projection of the final position vector on the initial orbital plane. Crossrange is measured as the perpendicular distance of the final position vector from the same orbital plane. All of these vectors are specified in a planet-fixed coordinate system.

Next, the initial and final conditions must be selected. For the purposes of this study, the vehicle is initially in a 500 km circular orbit and deorbits by targeting for a vacuum periapsis altitude of 5 km. This results in a flight path angle of  $-3.3^\circ$  and a velocity of 3550 m/s at entry interface (125 km altitude). For simplicity, the vehicle location is  $0^\circ$  longitude and  $0^\circ$  latitude at entry interface, and the vehicle heading is due east. These nominal initial conditions, summarized in Table 3.1, are used for all test cases in this chapter with the exception of those dispersed in initial flight path angle.

Since the aeromaneuvering trajectory is defined to end at parachute deployment,

this is where the terminal conditions are measured. For this study, the parachute is deployed at 5 km altitude, and this is chosen to be the trajectory termination condition.

Now that the initial and final conditions have been specified, a common control profile which demonstrates the full capabilities of the vehicle must be chosen. Flying constant full lift-up will provide the maximum downrange possible for a given vehicle, but trajectories with a constant bank profile do not achieve maximum crossrange performance. A vehicle flying a constant full lift out-of-plane ( $\phi = 90^\circ$ ) bank profile will turn quickly, but will fail to go far in crossrange because there is no vertical lift to extend the trajectory. A profile which optimizes the crossrange for a given downrange is needed.

In Reference [10], Spratlin chose to fly a linear bank angle with velocity profile for entry because this was shown to nearly maximize crossrange performance in [11] and [12]. Wagner [11] used several different optimization techniques to show that for a given  $L/D$ , the bank angle profile that maximizes crossrange is nearly linear with velocity. This can be seen in Figure 3.1 from [11]. This result is repeated in Reference [12] with a varying angle of attack for a simulated Shuttle entry. In this study, a generalized nonlinear programming technique called the Hybrid Nonlinear Programming method was used to determine the optimal bank angle profile seen in Figure 3.2. Although the linear bank profile is not optimal, it is a close approximation of the optimal profile and much easier to implement. An additional advantage of this profile is that it approaches full lift up at the end of the trajectory so that the

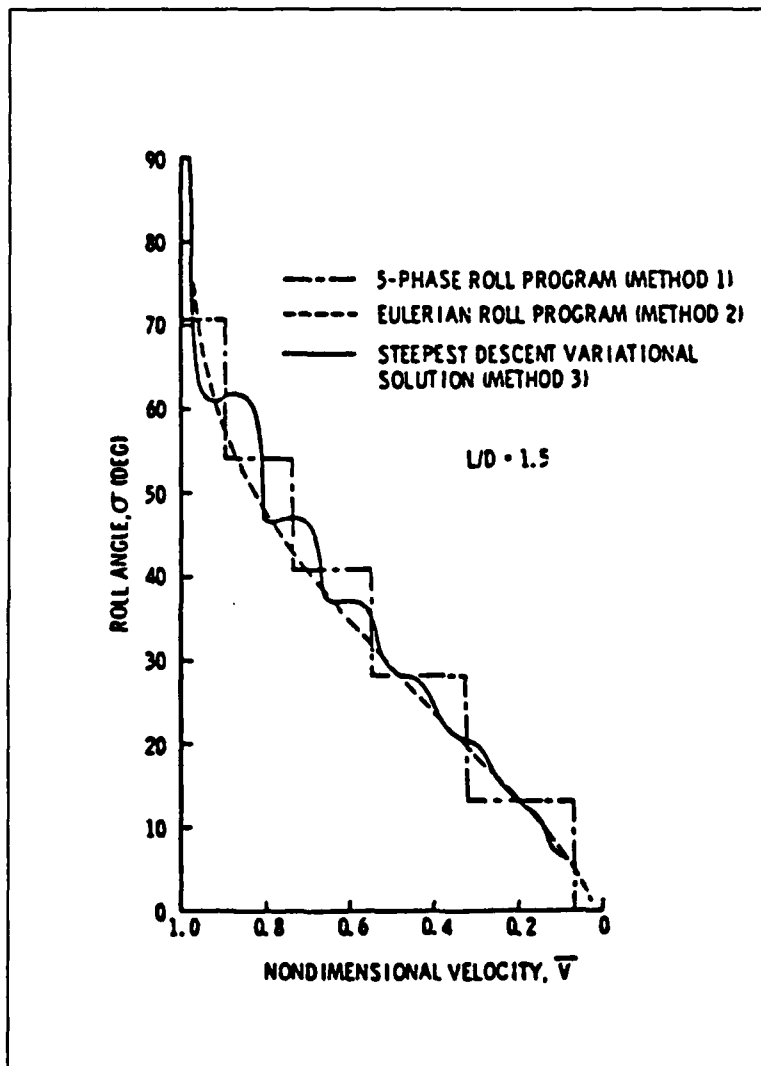
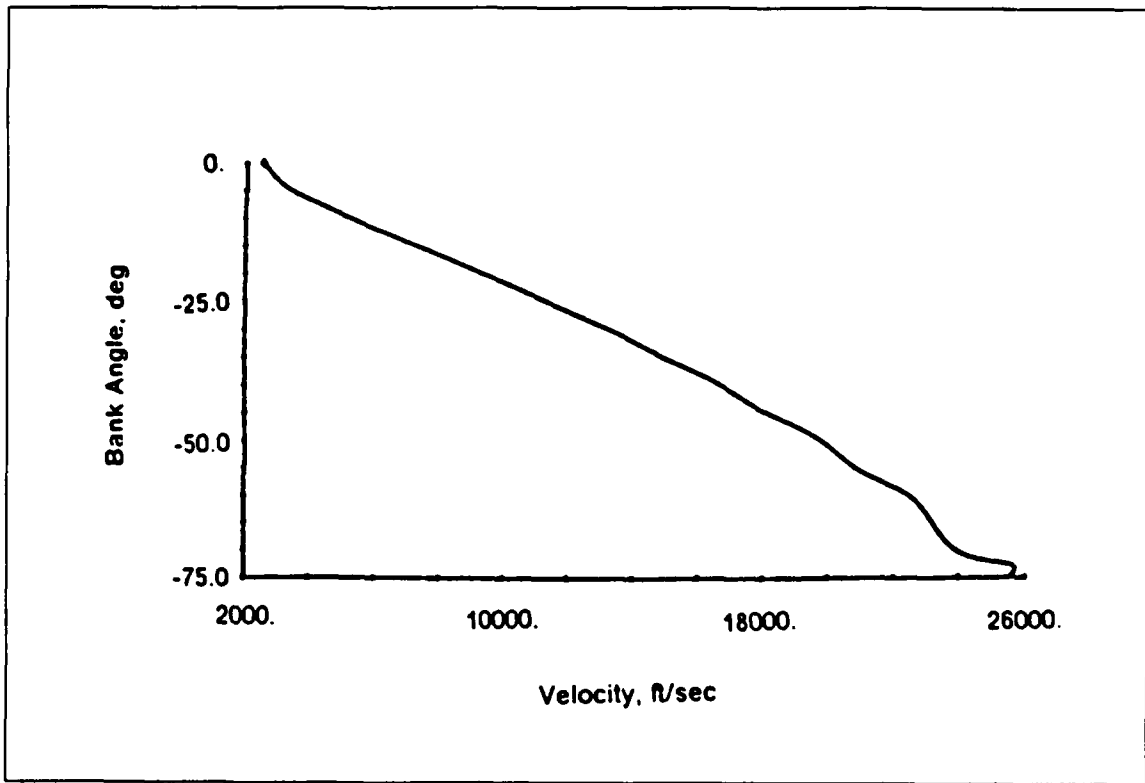


Figure 3.1. Comparison of Optimal Entry Bank Profiles



**Figure 3.2.** Shuttle Optimal Bank Profile

final flight path angle is relatively shallow, and this is one of the desired terminal conditions.

Based on the merits of the linear bank profile, it was chosen to be used to demonstrate vehicle capabilities. As seen in Figure 3.3, the bank angle decreases along the profile from an initial value at entry interface to zero degrees (full lift-up) at the estimated final velocity.

The equation which defines this profile is,

$$\phi_{cmd} = \phi_{des} \left( \frac{v - v_f}{v_{ei} - v_f} \right) \quad (3.1)$$

where,

- $\phi_{cmd}$  is the commanded bank angle
- $\phi_{des}$  is the initial or desired bank angle,
- $v$  is the current inertial velocity
- $v_{ei}$  is the entry interface velocity
- $v_f$  is a previously estimated final velocity

Protection is provided in case the inertial velocity decreases below  $v_f$ . If this occurs, the commanded bank angle is set to zero.

The initial bank angle determines the amount of vertical lift which will be used on a given trajectory, and thus defines the downrange achievable for a specific linear bank profile. For guidance purposes, the profile which will reach a target downrange is the "desired" profile, so the initial bank angle is referred to as the desired bank angle,  $\phi_{des}$ .

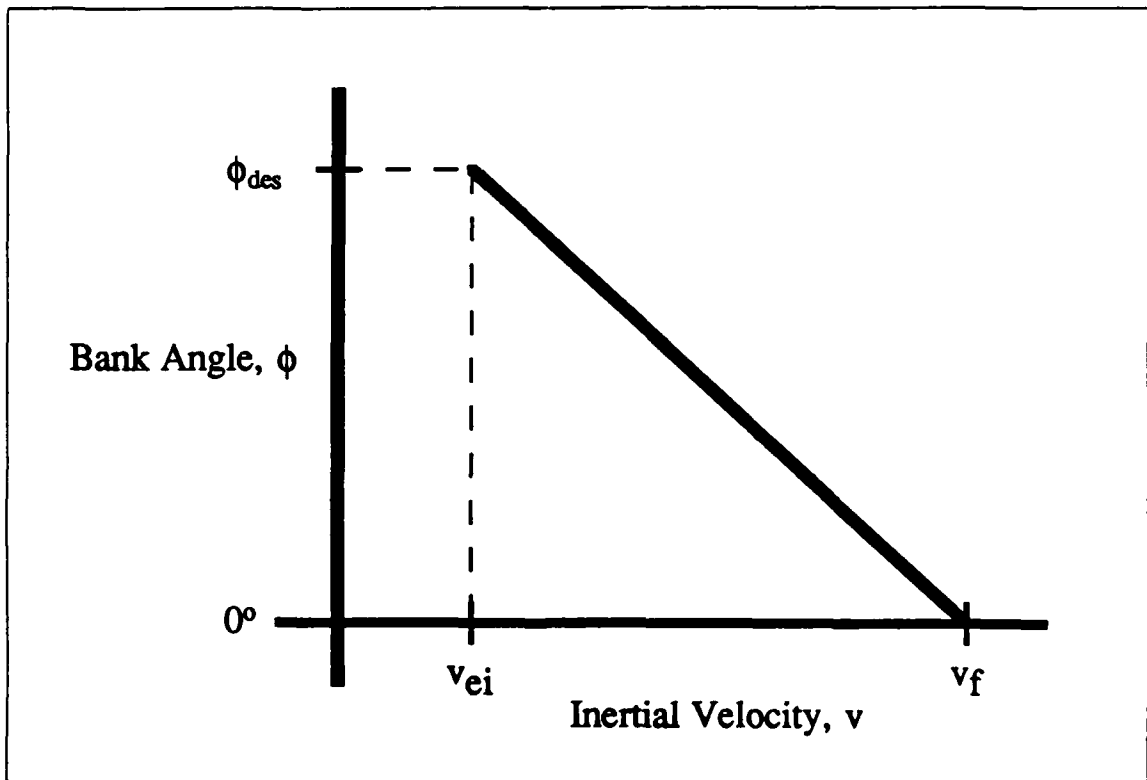


Figure 3.3. Linear Bank Profile

### 3.3 General Performance

The following two subsections examine the impact of important vehicle and environment factors on ranging capability and final dynamic pressure. The vehicles used are generic vehicles defined by a constant  $L/D$  and  $C_B$ . The different trajectories flown are obtained by varying the initial bank angle,  $\phi_{des}$ .

#### 3.3.1 Ranging Capability

Crossrange and downrange capability results are presented in terms of a maximum ranging capability footprint. This curve demonstrates the furthest point in a given direction that a vehicle can fly using the near optimal linear bank profile. The maximum ranging points which define this curve were obtained by flying the open-loop bank profile given by Equation 3.1 with various initial bank angles. Figure 3.4 shows the effect of  $L/D$  on ranging capability. Increased  $L/D$  has a large impact on both crossrange and downrange capabilities. As explained in Section 1.2, crossrange is the more limiting factor in mission flexibility. For a vehicle in a 500 km circular orbit, there is approximately 1800 km at the equator between adjacent groundtracks due to planet rotation. This requires a 900 km crossrange capability in order to reach any given target on a single series of orbital passes and ensure a deorbit possibility within a reasonable amount of time. As can be seen in Figure 3.4, an  $L/D$  of approximately 1.2 is necessary to achieve 900 km crossrange. This corresponds to an  $L/D$  approaching 1.4 to ensure this capability in the presence of dispersions.

The effect of vehicle ballistic coefficient,  $C_B$ , on ranging capability was examined

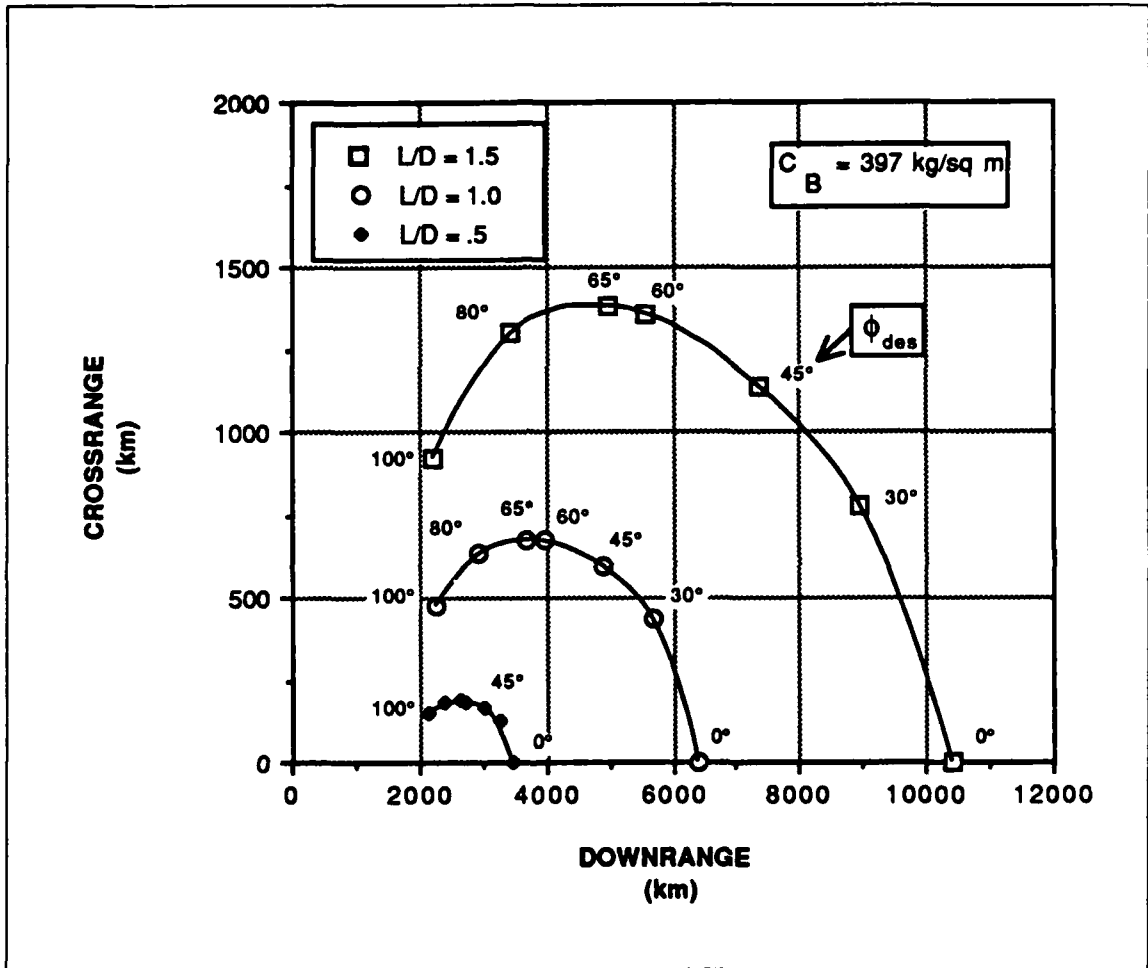


Figure 3.4. Maximum Ranging Capability: Effect of L/D

next. For a constant  $L/D$ , the crossrange capability was virtually independent of ballistic coefficient, and the downrange performance was only weakly dependent on this parameter. In general, vehicle ranging capability is not effected by  $C_B$  as supported by Figure 3.5.

The variation in ranging capability due to the coefficient of lift is the same as the variation due to  $L/D$  because changing  $C_L$  simply effects  $L/D$ . The variation in ranging capability due to the coefficient of drag is almost the same as the variation due to  $L/D$ . This is true, despite the fact that changing  $C_D$  also changes  $C_B$ , because ranging capability is essentially independent of  $C_B$ .

The only initial condition for which ranging performance is found to be sensitive is the entry flight path angle,  $\gamma_{ei}$ . Small changes in initial flight path angle greatly vary downrange performance, and also have a significant, although smaller, impact on crossrange capability. As seen in Figure 3.6, the downrange performance can be greatly increased by entering at a shallower flight path angle. However, this increase in downrange performance, which only slightly enhances guidance capability, comes with an increased risk of the vehicle skipping back out of the atmosphere. The maximum downrange (full lift-up) case with the shallow  $\gamma_{ei}$  came very close to skipping out, and any shallower flight path angle would probably skip. The crossrange is increased, but the risk associated with skipping and widely missing the target must be balanced with this.

The steeper  $\gamma_{ei}$  reduced both the downrange and crossrange maneuver capacity, but the change in ranging capability is not as large as it is for the shallower  $\gamma_{ei}$ .

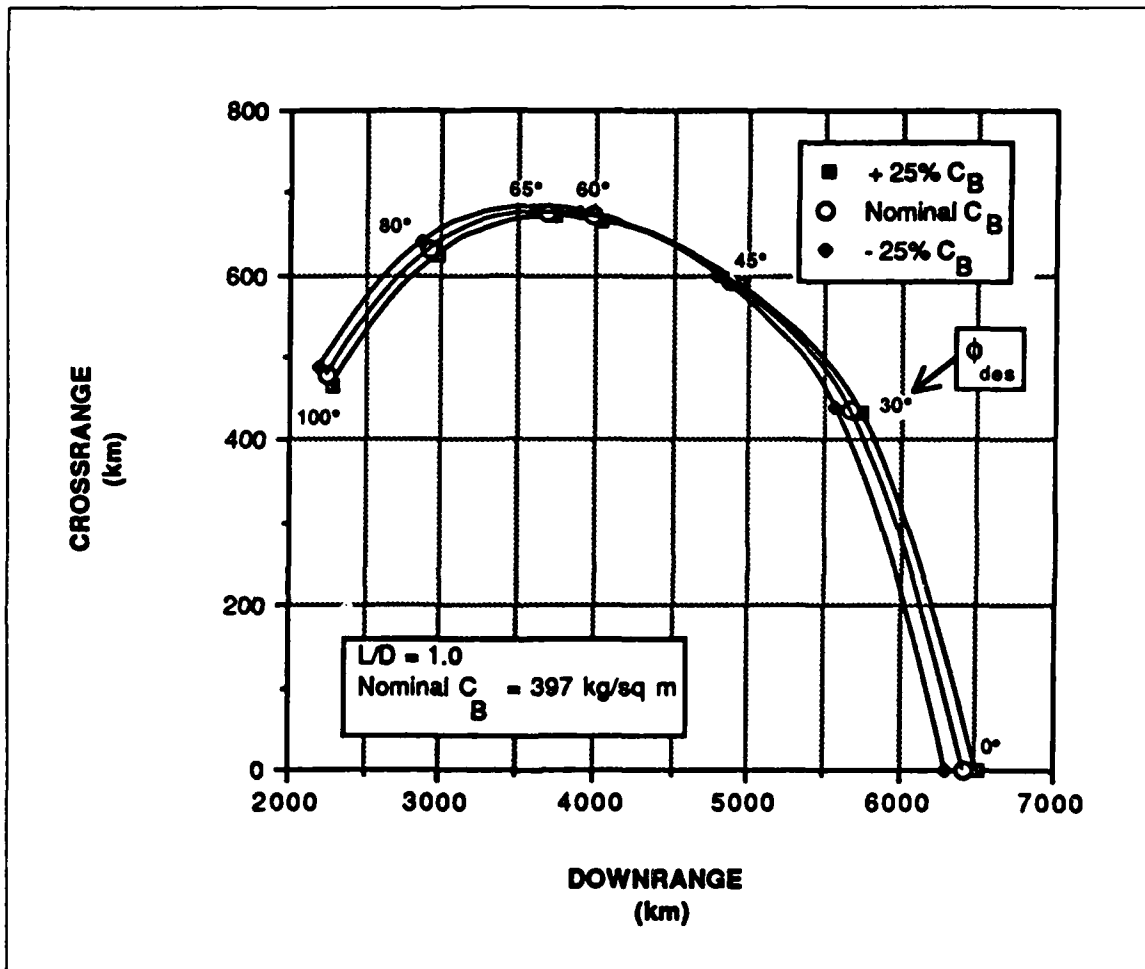


Figure 3.5. Maximum Ranging Capability: Effect of Ballistic Coefficient

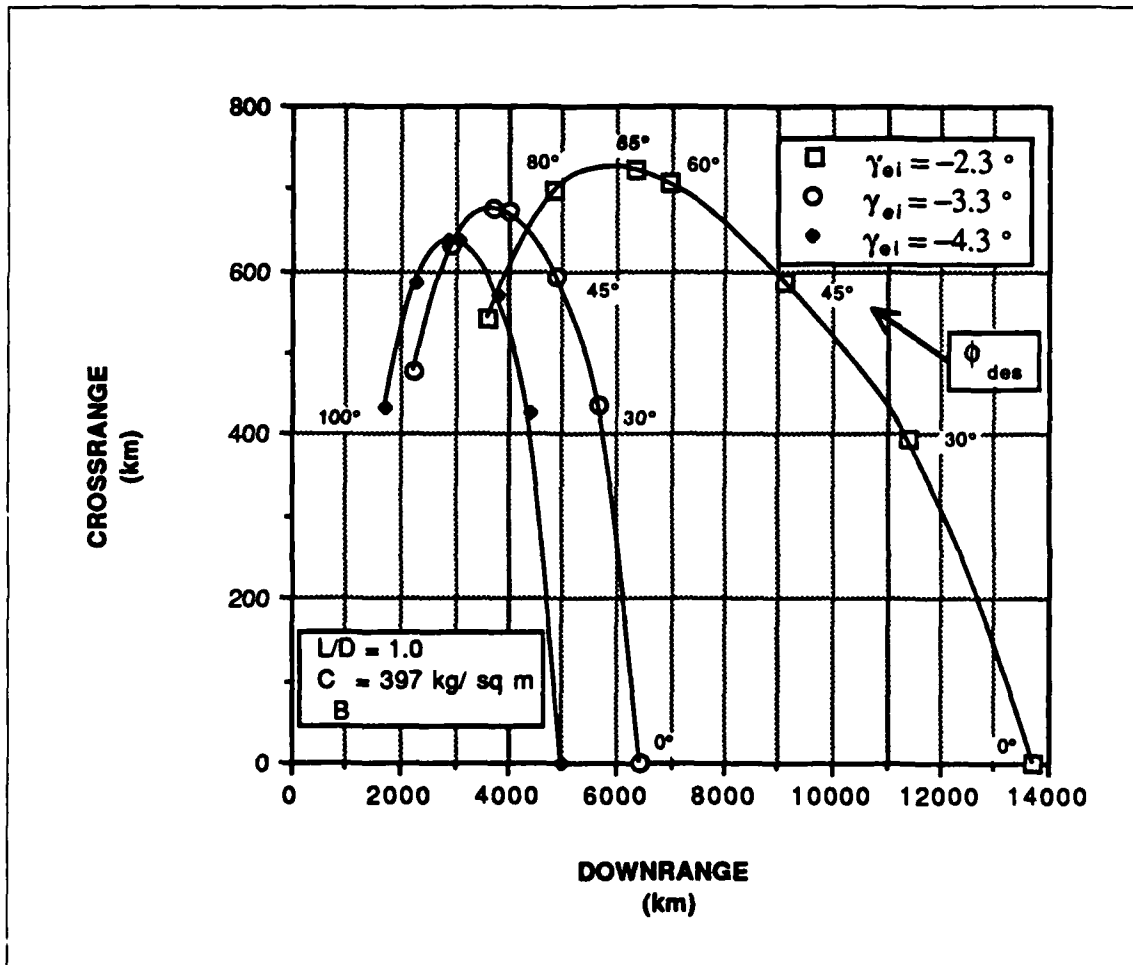


Figure 3.6. Maximum Ranging Capability: Effect of Entry Flight Path Angle

However, the difference is still significant as the reduction is approximately equivalent to a reduction in  $L/D$  from 1.0 to 0.9. The large variation in ranging capability for such small differences in  $\gamma_{ei}$  indicates that it will probably be important to hit the target value because there is a narrow entry corridor. The target entry flight path angle should be chosen as a compromise between maximizing ranging capability and minimizing the risk of skipping.

The two major environmental concerns during entry are atmospheric density and wind dispersions. Winds do not significantly affect the ranging performance as they might be expected to. For example, a headwind increases the lift of the vehicle so that it flies for a greater length of time, and this partially counters the effect reduced ground speed has on range. Crossrange is affected more than downrange because the vehicle crossrange velocity is slower relative to the wind than the downrange velocity. The decrease in crossrange caused by an opposing wind is noticeable, but not a major ranging factor.

Atmospheres which have variable densities that continually shift about the nominal density have a relatively small effect on ranging capability because the integrated effect is about the same as if the density had remained nominal. (While vehicle performance is not greatly affected, this type of atmosphere can profoundly influence guidance performance, as will be examined in Chapter 5.) It is large density biases which remain throughout the trajectory that can have a significant effect of ranging performance. This effect can be seen in Figure 3.7. An atmosphere which is consistently thinner than expected increases vehicle downrange capability because there is

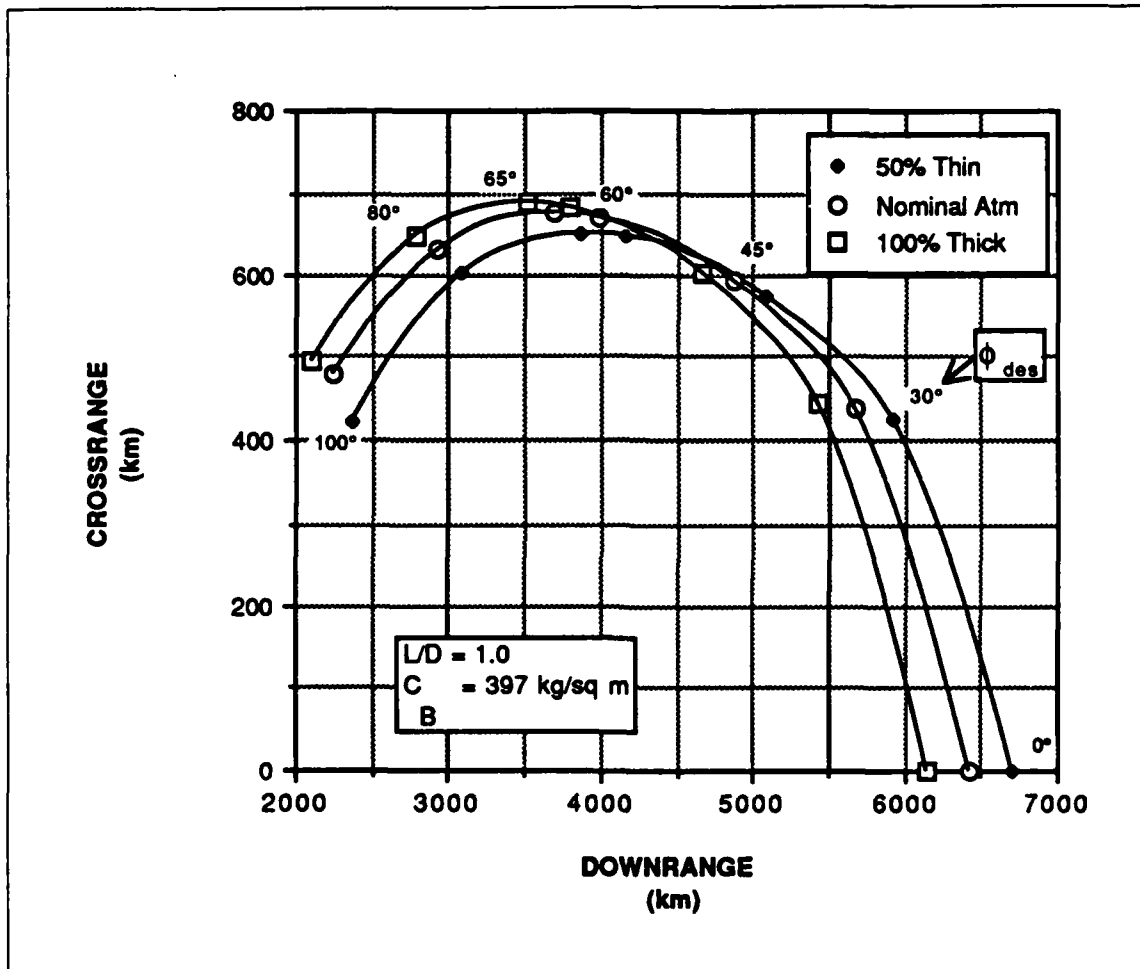


Figure 3.7. Maximum Ranging Capability: Effect of Constant Density Biases

less resistance, but at the same time, this atmosphere decreases crossrange capability because there is less atmosphere to turn the vehicle. A thick atmosphere decreases downrange performance and increases crossrange capability for the opposite reasons. It is interesting to note that a headwind acts much like a thick atmosphere and a tailwind acts like a thin atmosphere in regards to ranging performance, the difference being that the change due to winds is much smaller than the change due to density biases for the assumed dispersions.

### 3.3.2 Final Dynamic Pressure

The influence of vehicle design and environmental factors on final dynamic pressure,  $\bar{q}_f$ , is examined in this section. But first, the nature of the dynamic pressure variation during entry is presented.

The dynamic pressure history throughout entry was found to be analogous to a damped sinusoid as can be seen in an example in Figure 3.8. This is not unexpected as the dynamics of a constant  $L/D$  entry trajectory have been likened to the response of a simple second-order spring-mass-damper system in [13]. During the trade-off between potential and kinetic energy which occurs throughout entry, drag is a non-conservative force which provides damping to the system. Hence, the dynamic pressure appears to be driving to a final "steady-state" value with long-period (phugoid) oscillations about that value. The final dynamic pressure varies widely for a given vehicle design or dispersion because the magnitude of  $\bar{q}_f$  is dependent not only upon the "steady-state" value, but upon the point in the oscillation about that value that the entry maneuver terminates. The peaks and valleys in the typical trajectory shown in Figure 3.8

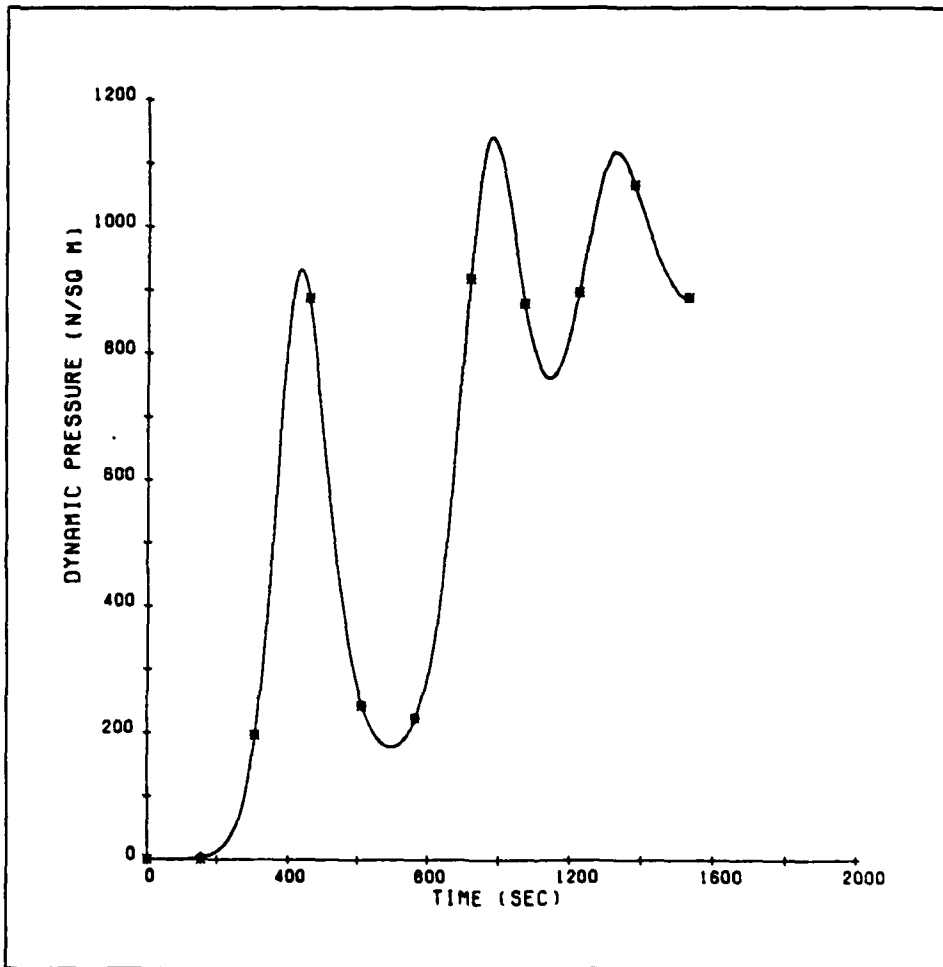


Figure 3.8. Typical Dynamic Pressure Response During Entry

range between 1150 and 800 N/sq m while the "steady-state" dynamic pressure is approximately 1000 N/sq m.

It is clear that the final dynamic pressure for a single trajectory is not sufficient to define the  $\bar{q}_f$  qualities associated with a given vehicle design or dispersion. For this reason, the range of final dynamic pressures for a wide selection of trajectories is necessary to characterize dynamic pressure performance. The various trajectories used to define the maximum ranging capabilities in the previous section conveniently provide a database of final dynamic pressures which is used in this analysis. The range of final dynamic pressures for a given parameter represents the magnitude of the oscillations about the "steady-state" value, while the median value in the range is a rough indicator of the "steady-state" final dynamic pressure.

The first vehicle characteristic analyzed for dynamic pressure performance was L/D. Increasing L/D was found to decrease final dynamic pressure as indicated in Figure 3.9. A higher L/D allows the vehicle to fly further through the atmosphere, and this means more atmosphere to decelerate the vehicle. This implies that the vehicle design L/D should be as large as feasible if final dynamic pressure is a concern.

Decreasing ballistic coefficient was found to also decrease final dynamic pressure as seen in Figure 3.10. The mean value, as well as the size of the range in values, decreased with  $C_B$ . In fact, for any given trajectory defined by its bank profile, the final dynamic pressure was found to be almost linearly dependent upon  $C_B$ . This result is demonstrated for a near-maximum crossrange trajectory which used an initial bank angle of  $65^\circ$  in Figure 3.11 . This implies that the entry vehicle design should

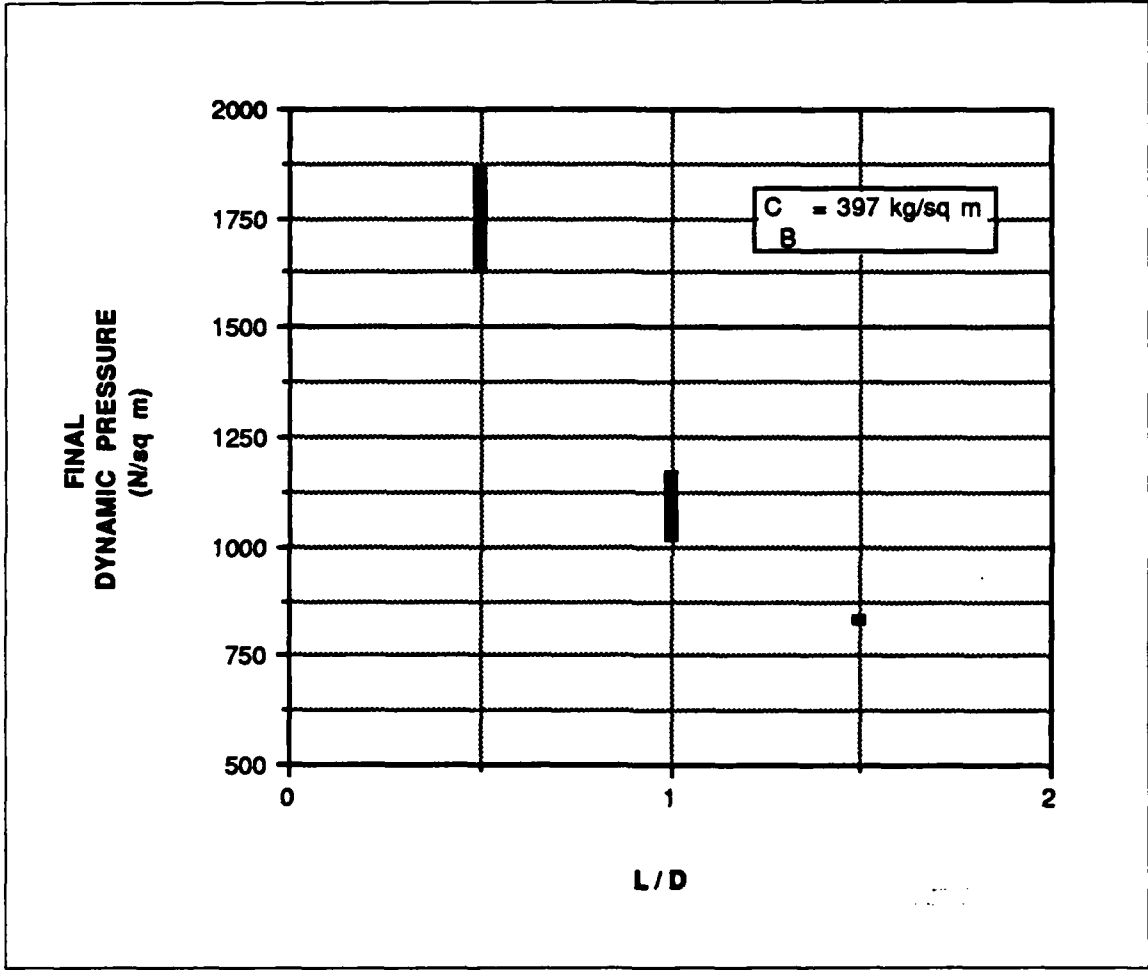


Figure 3.9. Final Dynamic Pressure Range: Effect of L/D

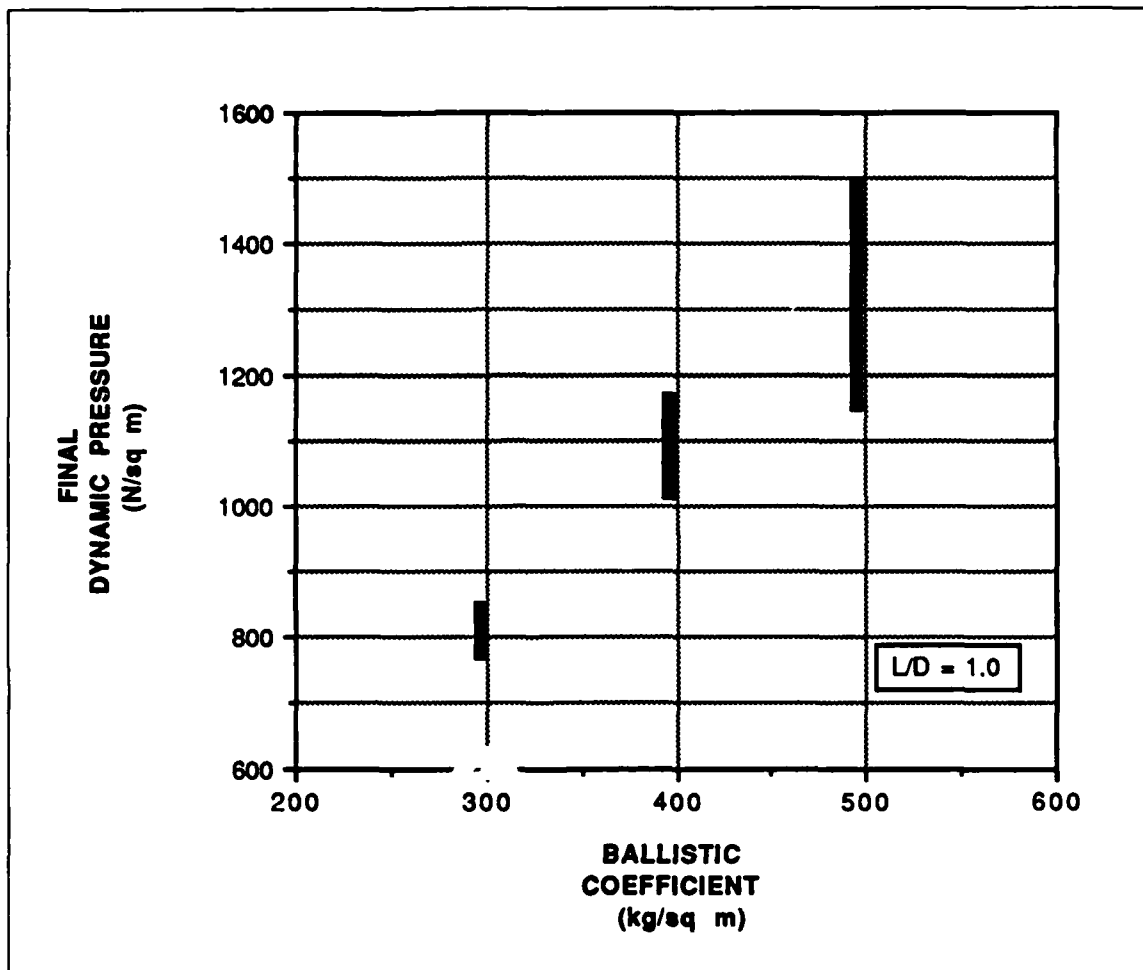


Figure 3.10. Final Dynamic Pressure Range: Effect of Ballistic Coefficient

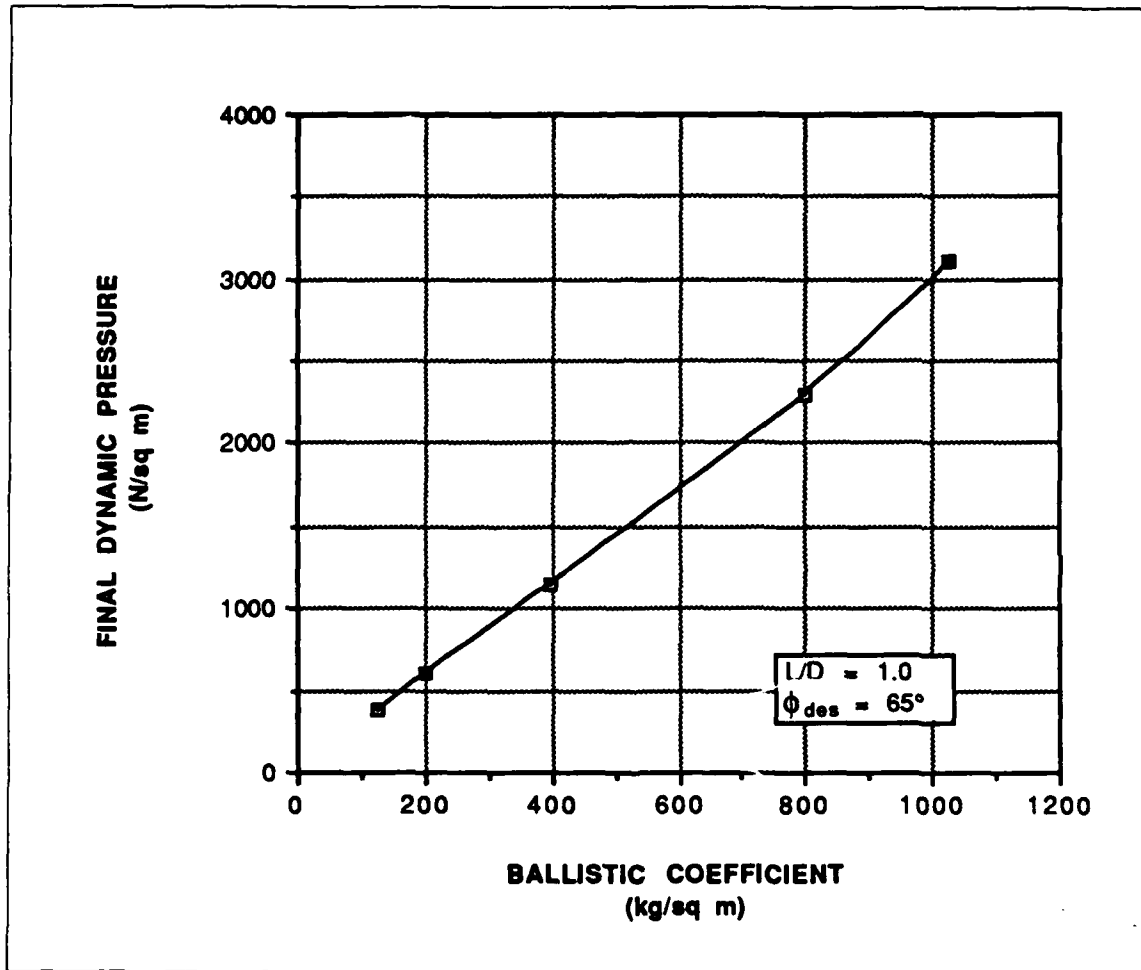


Figure 3.11. Final Dynamic Pressure: Effect of Ballistic Coefficient for a Particular Bank Profile

have as low as ballistic coefficient as possible when final dynamic pressure is a factor.

Next, the environmental effects on final dynamic pressure are analyzed. Winds were found to be a minor factor influencing final dynamic pressure. Regardless of the winds, the vehicle generally reached the target with approximately the same relative velocity, and hence the same  $\bar{q}_f$ . In fact, the primary environment characteristic affecting final dynamic pressure is density. An atmosphere with a constant thin bias does not permit generation of enough drag to allow the vehicle to sufficiently slow down, causing higher final dynamic pressures. A thick atmosphere has the opposite effect. It allows the vehicle to decelerate quickly and helps reduce final dynamic pressure. The dramatic effect variations in atmospheric density have on final dynamic pressure is evident in Figure 3.12. This is a concern because there is a relatively large amount of uncertainty regarding the density that will be encountered.

In the last portion of this study, the effect that dispersions in the entry flight path angle had on final dynamic pressure was examined. The results are presented in Figure 3.13. The steeper flight path angle caused a wider range in the final dynamic pressure, but the mean value remained the same regardless of the variation. Some caution must be used in interpreting this because these results are specific for a single  $\gamma_{ei}$ . Other entry flight path angles might be more sensitive, in terms of  $\bar{q}_f$ , to dispersions.

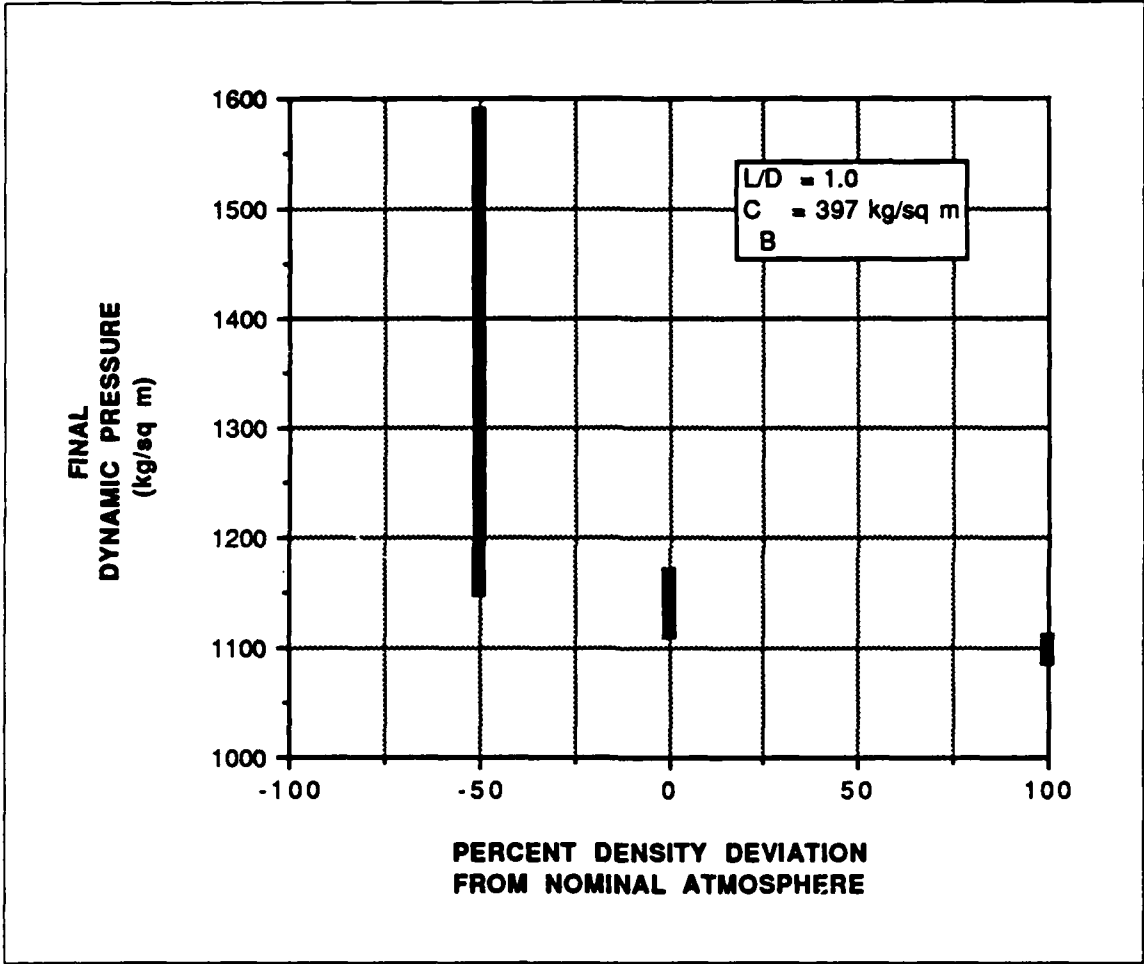


Figure 3.12. Final Dynamic Pressure Range: Effect of Constant Density Biases

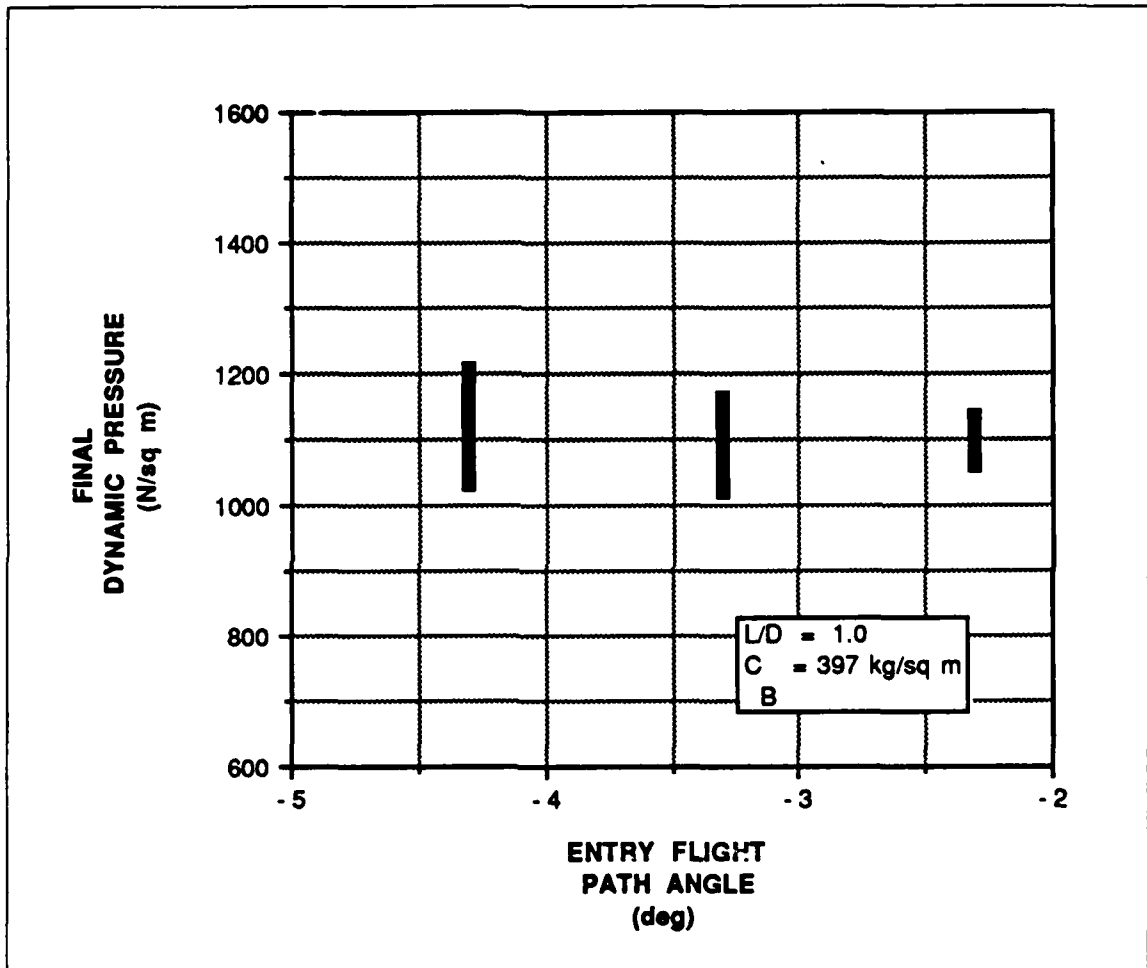


Figure 3.13. Final Dynamic Pressure Range: Effect of Entry Flight Path Angle

### 3.4 Vehicle M Performance

The design of entry vehicles is not driven by guidance considerations alone. Once a vehicle has been designed, a guidance must make do with the vehicle capabilities and limitations. So, given a particular vehicle, it is important to determine how the performance can be varied and what the maximum possible performance is. The vehicle that was used to demonstrate this analysis was a biconic lifting body, designated Vehicle M, baselined at NASA Johnson Space Center for the Mars Rover Sample Return program [1]. Vehicle M has a maximum L/D near 1.1, and at the trim angle of attack of  $26.04^\circ$ , Vehicle M has a 1.0 L/D. The lift coefficient, drag coefficient, and L/D curves which define this vehicle can be seen in Figures 3.14, 3.15, and 3.16.

In addition, the mass of Vehicle M is 4082 kg, and the surface reference area is 14.19 sq m. This reference area combines with the mass and the coefficient of drag at the trim angle of attack to give a ballistic coefficient of 397 kg/sq m.

For Vehicle M, the trim angle of attack is very sensitive to the location of the center of gravity. Near  $30^\circ$ , a 1% shift in center of gravity location along the length of the vehicle will cause a  $2.5^\circ$  shift in trim angle of attack [14]. Therefore, it is a relatively simple matter to change  $\alpha_t$ . Since changing  $\alpha_t$  varies the effective ballistic coefficient as well as changing the lift-to-drag ratio, the vehicle performance can be modified by small changes in the placement of the center of gravity.

The previous section showed that ranging capability is basically defined by the L/D at which the vehicle flies—the higher the L/D, the greater the ranging capability. To maximize the ranging capability of Vehicle M, the vehicle should be flown at the

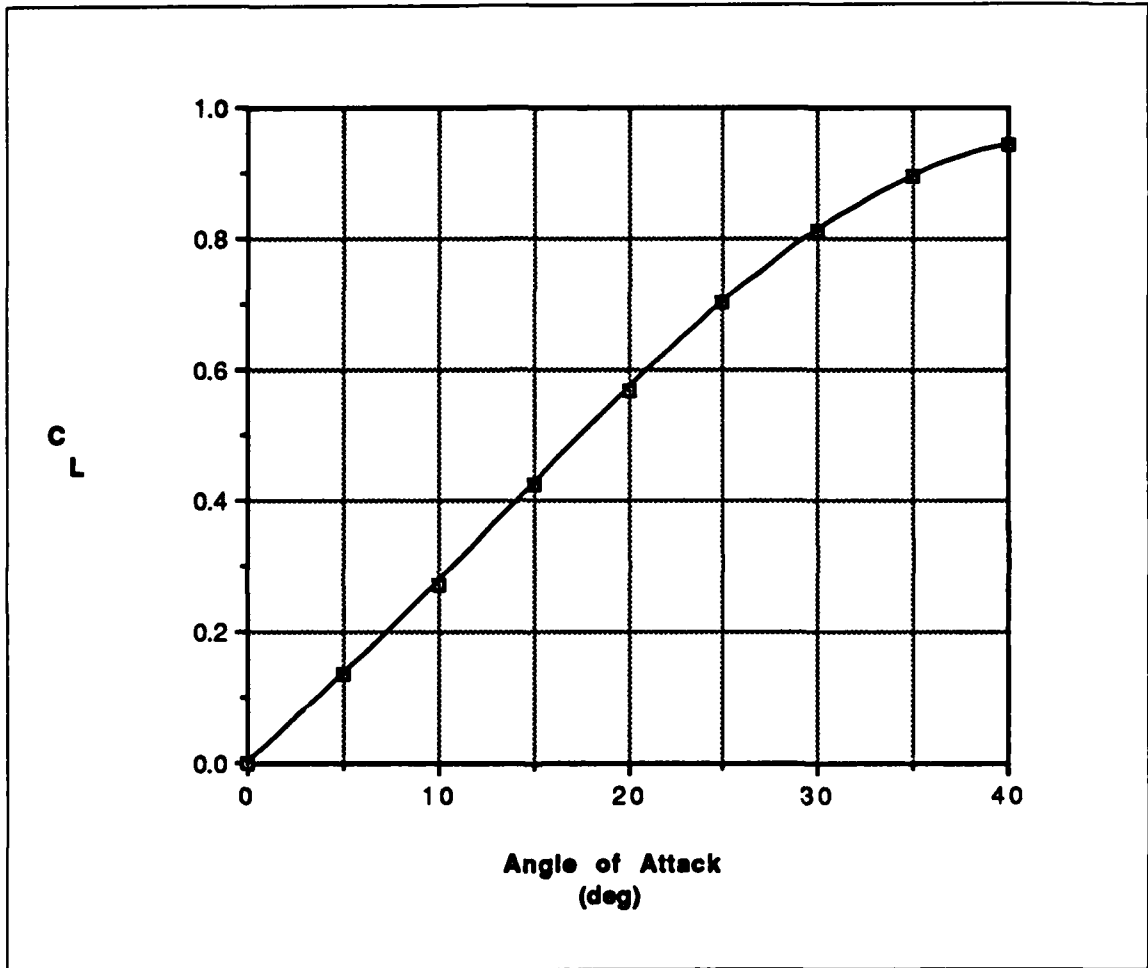


Figure 3.14. Vehicle M Lift Coefficient Curve

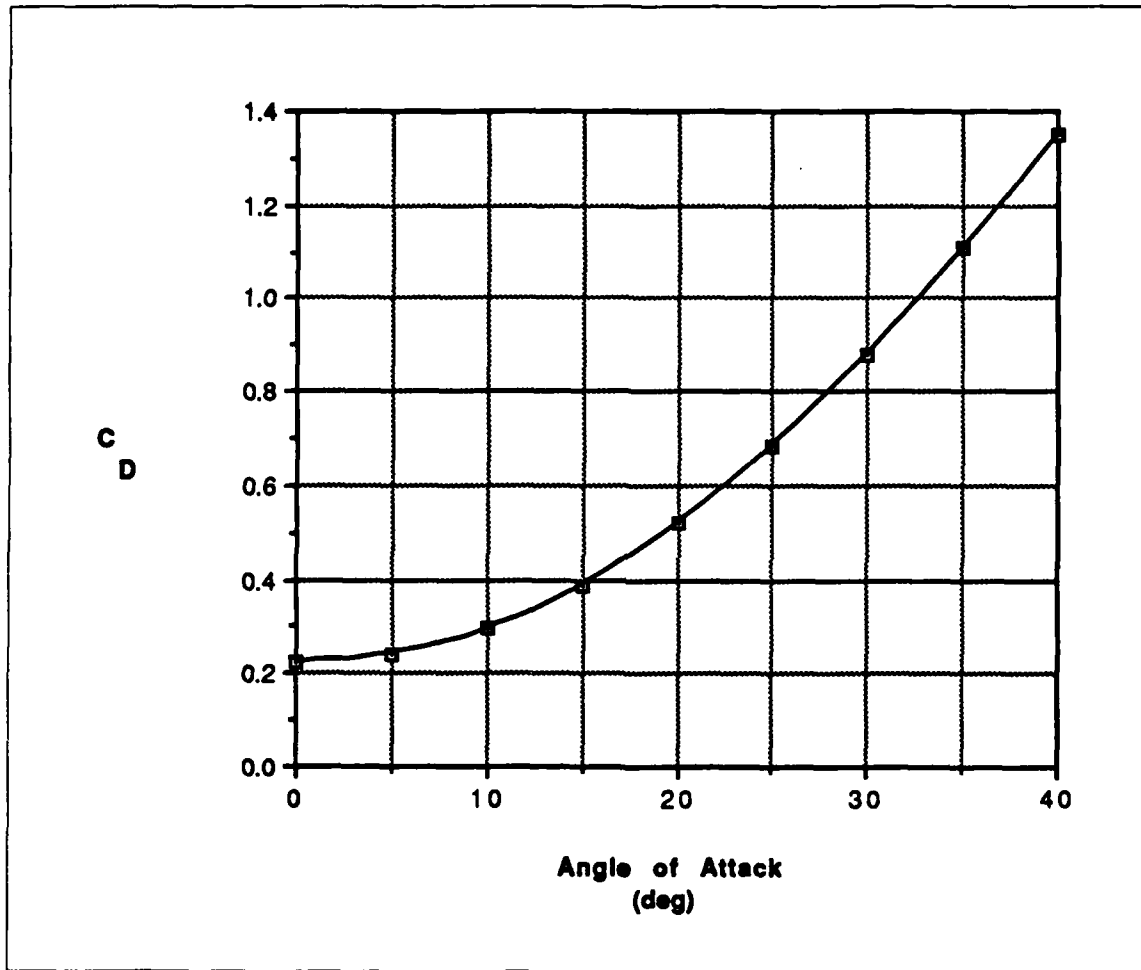


Figure 3.15. Vehicle M Drag Coefficient Curve

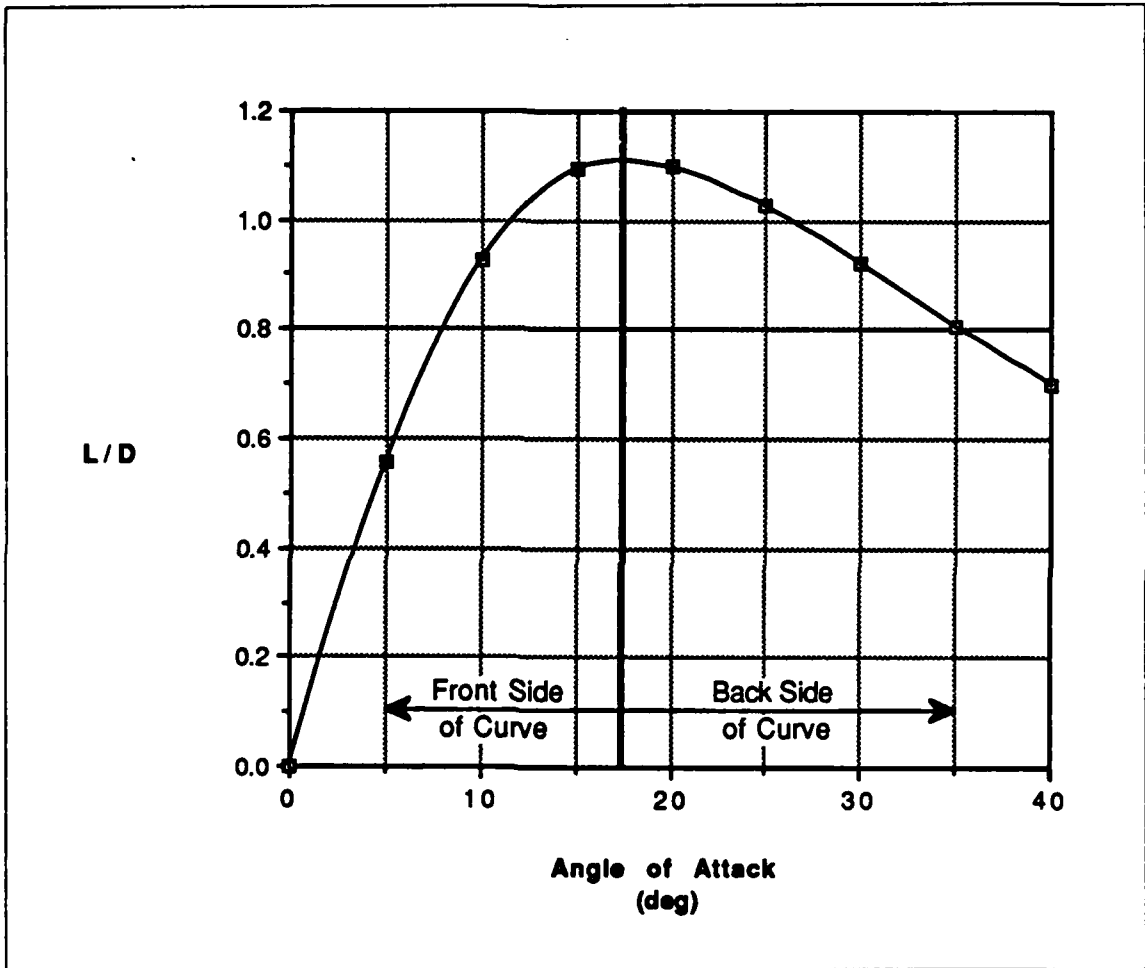


Figure 3.16. Vehicle M L/D Curve

trim angle of attack which corresponds to maximum L/D. It is also noted that if one is not flying at the maximum L/D, it is possible to fly the same L/D, and get approximately the same ranging performance, at two different angles of attack. This is illustrated for the trim angles of attack of  $12^\circ$  and  $26.04^\circ$  in Figure 3.17. The difference in ranging performance is just the small change caused by variation of ballistic coefficient that was noted in Section 3.3.1.

However, ranging capability is not the only performance requirement. Final dynamic pressure performance must also be considered when determining the trim angle of attack to be flown. The change in final dynamic pressure due to various trim angles of attack for Vehicle M is shown in Figure 3.18. It can be seen that the higher angles of attack result in lower final dynamic pressures. This is because the higher angles of attack increase the coefficient of drag which has the same effect on final dynamic pressure as reducing the ballistic coefficient. The reduction in final dynamic pressure (and final velocity) obtained by flying at the higher angles of attack is the reason that entry vehicles generally fly on the back side of the L/D curve. The back side of the L/D curve is where increasing angle of attack results in lower lift-to-drag ratios as seen in Figure 3.16. The Space Shuttle flies on the back side of its L/D curve until late in the trajectory when it transitions from a decelerating entry vehicle to a flying glider.

Besides final dynamic pressure considerations, there are several other reasons why it is desirable to fly at higher angles of attack. A higher angle of attack means a further aft center of gravity (cg) location. Reference [14] states that a further aft

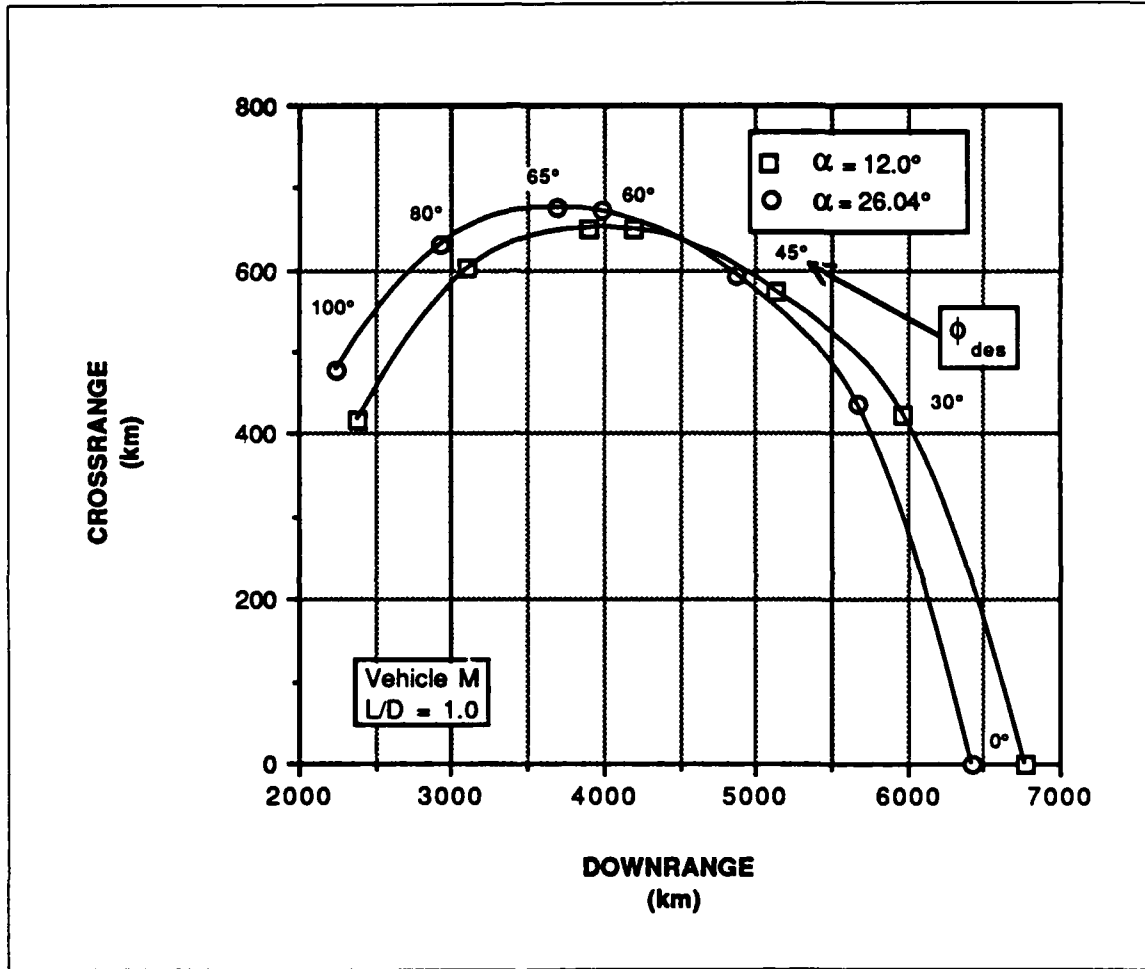


Figure 3.17. Vehicle M: Ranging Performance Comparison of Two Angles of Attack — Front and Back Side of L/D Curve

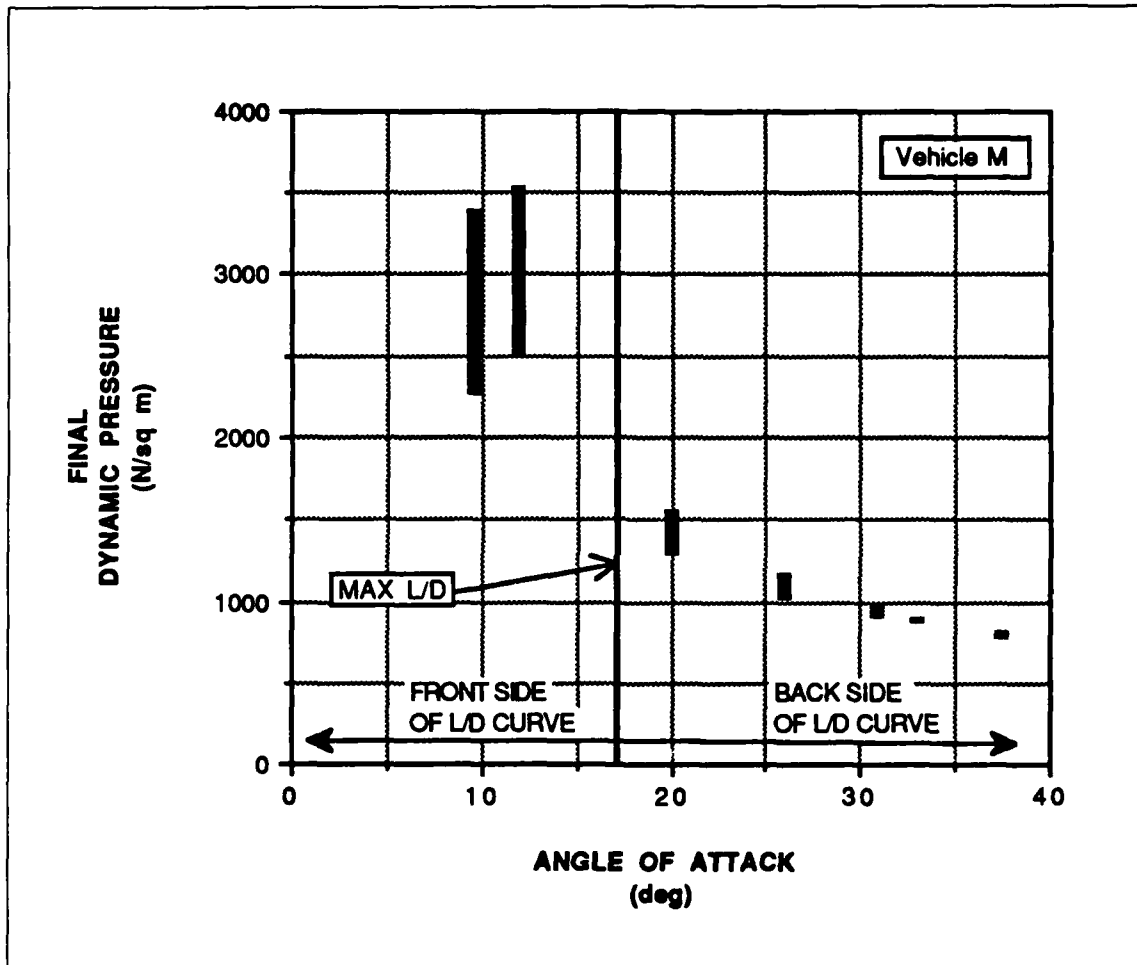


Figure 3.18. Vehicle M: Effect of Angle of Attack on Final Dynamic Pressure

cg is advantageous because 1) during launch, the cg is lower and closer to the base which provides better booster performance due to reduced booster loads and 2) it is much easier to package components in the large end of the vehicle cone. While the first advantage is specific to one candidate booster, the Centaur upper stage, the second is true of most any biconic vehicle. Additionally, a higher angle of attack is statically more stable which means that there is greater restoring force if the vehicle is perturbed from the nominal angle of attack. A final reason why a higher angle of attack is preferable is that it decreases the ballistic lift coefficient,  $m/C_L S$ , which means that the vehicle is more maneuverable and can effect faster turn rates.

While all of these factors favor a high angle of attack, it must be realized that on the back side of the L/D curve, L/D and ranging capability decrease with greater angles of attack. Because of this trade-off, Vehicle M should be flown only at a high enough angle of attack to sufficiently reduce  $\bar{q}_f$ . Further increases in  $\alpha_t$  are not justified in view of decreasing ranging performance. This decrease is quantified for Vehicle M in Figure 3.19. For the given constraints, an angle of attack of  $33^\circ$  is necessary to reduce the final dynamic pressure to within the general limits. As can be seen, this causes a significant reduction in ranging performance, illustrating the trade-off for fixed vehicle aerodynamic design between maximizing ranging capabilities and decreasing final dynamic pressure.

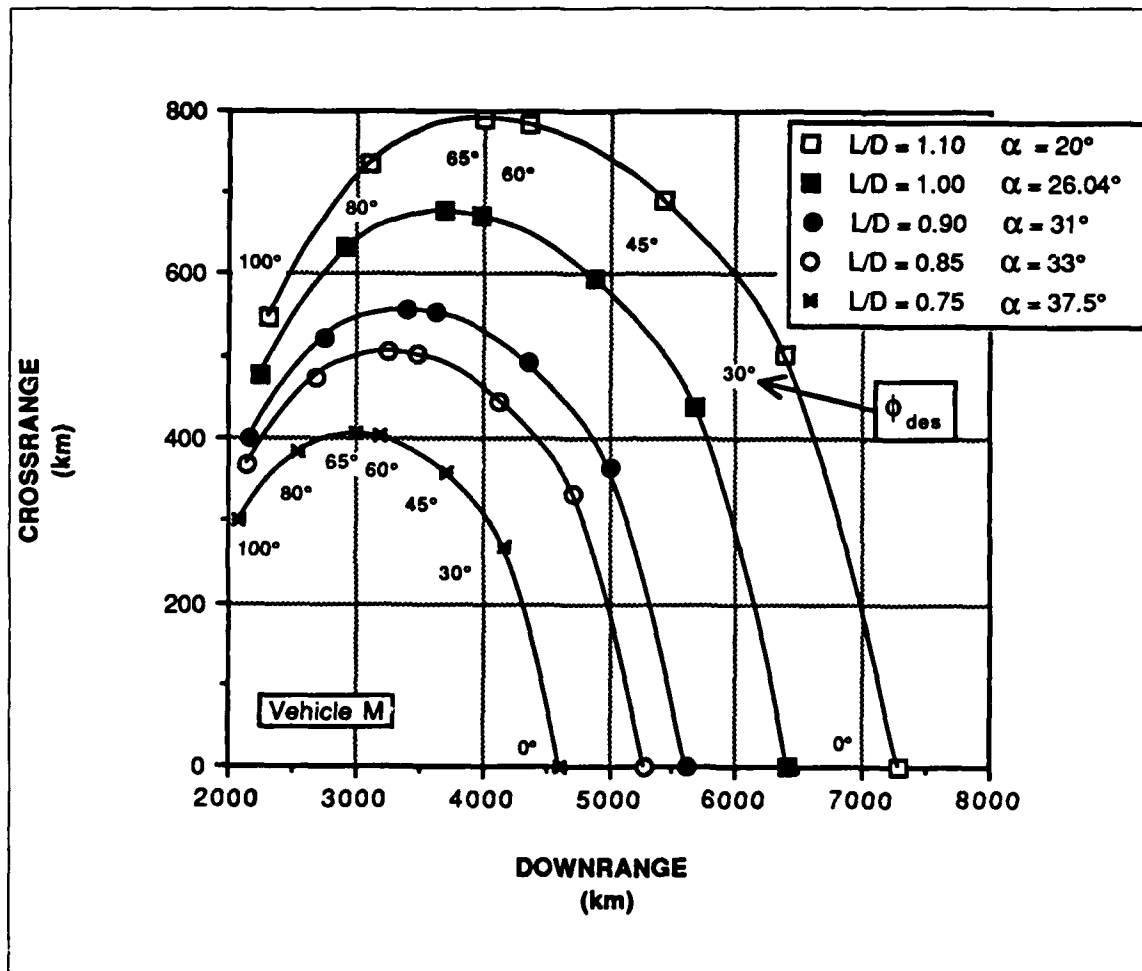


Figure 3.19. Vehicle M: Effect of Angle of Attack on Maximum Ranging Capability

### 3.5 Divert Capability

During entry, there will undoubtedly be inaccuracy in the vehicle navigation position estimate and in the knowledge of the target location due to significant errors in knowledge of the orientation of Mars in inertial space and in the ability to locate remote images on the globe. This will cause the guidance to aim for a point which is not actually the true target. In order to reduce these errors, a beacon may be placed at the target. Navigation updates provided by this beacon will help determine the location of the vehicle relative to the landing site, and in doing so will "move" the target relative to the vehicle. The vehicle must still be able to reach the target even though it was not initially aiming for it. This matter is complicated because this navigation aid only becomes visible late in the entry trajectory. Therefore, the ability of a vehicle to divert to the new target location late in the trajectory is important.

In order to investigate divert capability, an entry was flown to a typical target (DR 3500 km, CR 200 km). For this trajectory, the landing site became visible at a range of 468 kilometers. It was assumed for this study that the navigation beacon which provides improved knowledge of the landing site location also becomes visible at this point. From this possible divert point in the nominal trajectory, the open-loop ranging capabilities of Vehicle M ( $\alpha_t = 33^\circ$ ,  $L/D = 0.85$ ) were analyzed. In addition, the divert capability was tested at two later points in the trajectory—278 and 103 km from the target. The inertial velocity at each of these three points was approximately 1400, 1000, and 500 m/s greater than the nominal terminal velocity. The velocity prior to nominal termination is given because it is a more universal indicator of the

location of the vehicle in the trajectory. The results are shown in Figure 3.20.

The footprint shrinks rapidly as the vehicle nears the target. Immediately after signal acquisition (1400 m/s prior to ending), under ideal conditions the vehicle could reach any new location within a 45 km radius of the original target. Approximately 190 km and 400 m/s later, the footprint has shrunk to 20 km. Another 175 km and 500 m/s later, at a range of 103 km, the circle radius is only 7 km.

The larger divert bank angles cause the entry vehicle to dump a significant amount of vertical lift in order to reach a closer target. Since a loss in vertical lift initially causes a drop in altitude and an increase in velocity, the final dynamic pressure can be significantly increased by attempts to divert to short targets late in the trajectory. The increase in final dynamic pressure is not as great when the divert is earlier in the trajectory because the increased drag due to the higher velocity and density has time to act on the vehicle and reduce velocity. For the trajectory tested, the vehicle could divert anywhere within its ranging capability at signal acquisition without exceeding the final dynamic pressure limit. For the later diverts, some shorter targets are not reachable because of the final dynamic pressure limit. If divert capability is defined as the largest possible circle centered at the target which encompasses divert landing sites, the dynamic pressure limit does not really effect the divert capability. This is true because the size of this circle is bounded in the positive downrange direction by a limited ability to fly further.

Without any navigation updates from an orbiting vehicle or other ground beacons during entry, the  $3\sigma$  navigation position error relative to the landing site at

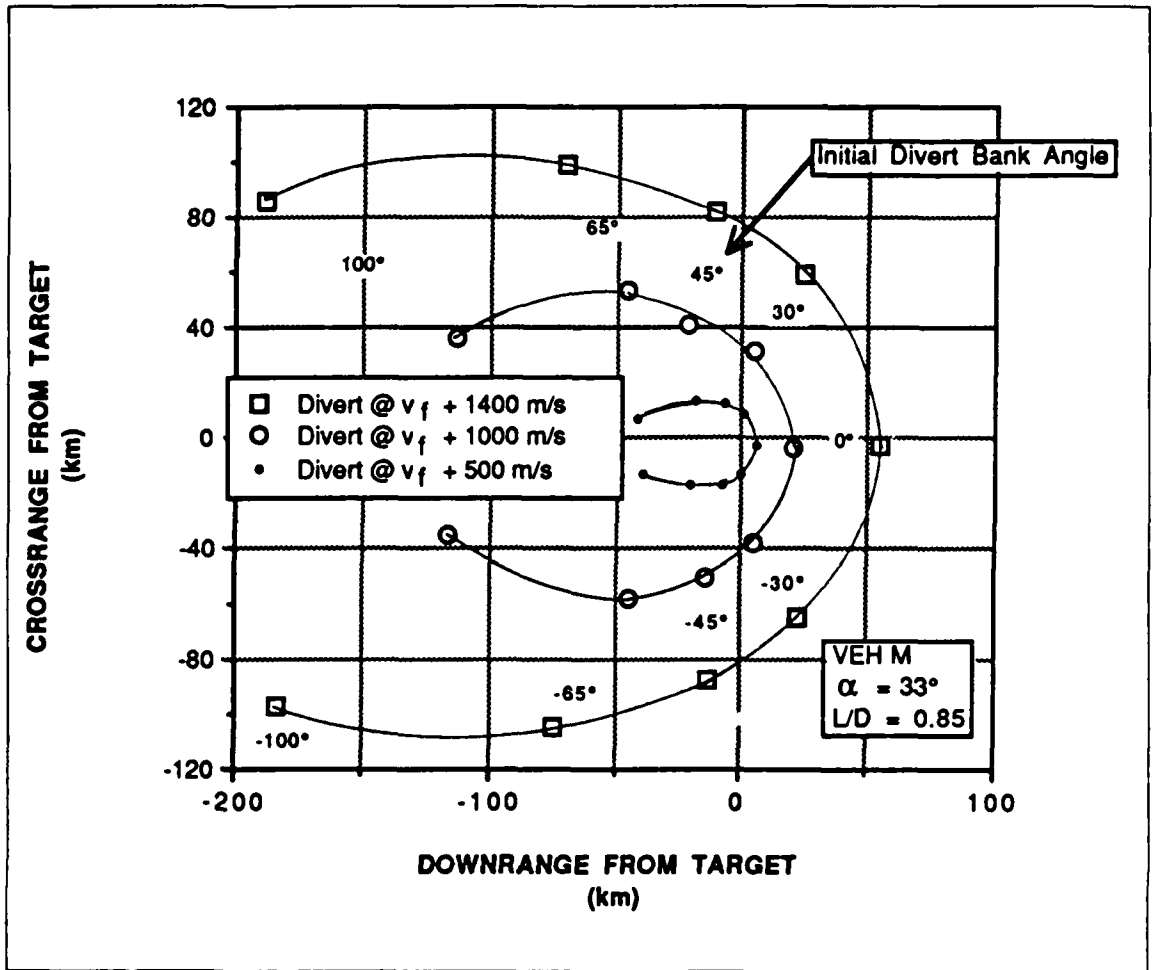


Figure 3.20. Divert Capability

parachute deployment is expected to be less than 5 km [15]. Provided that the need to divert is recognized soon after acquisition of signal, the divert capability for this low performance vehicle is well within expected navigation errors.

# Chapter 4

## Guidance Design

The guidance algorithm developed here uses bank angle control in order to meet downrange, crossrange, and final dynamic pressure constraints. This chapter examines previous work relevant to entry guidance in Section 4.1 and then presents the guidance and its motivation in Section 4.2. The derivation of each portion of the guidance algorithm follows in the remainder of the chapter with the downrange control explained in Section 4.3, the crossrange control detailed in Section 4.4, and the dynamic pressure control examined in Section 4.5.

### 4.1 Previous Work

The majority of precision landing guidance work has been concentrated on Earth entry, and relatively little guidance work has been done regarding precision entry at Mars. Although there are significant differences, such as a thinner, more uncertain Mars atmosphere and greater navigation errors, the two problems are similar enough for much of the Earth work to be applicable to Mars. Earth entry guidance designs

which are of interest include those for Apollo [16], the Space Shuttle Orbiter [17], and the Entry Research Vehicle (ERV) [10]. Also of interest is an aerobraking guidance algorithm developed for the Aeroassist Flight Experiment (AFE) [18].

The Apollo entry guidance was designed to obtain landing accuracy of 15 nautical miles using a very low L/D (0.3) vehicle [16]. This was achieved using one control variable, bank angle, to maintain a reference drag acceleration profile trajectory. This reference drag profile was analytically determined prior to flight to meet the downrange, heating, and g-load requirements. The crossrange requirements were met by varying the sign of the bank angle based on the current crossrange error. The low L/D of the vehicle, while providing relatively little control over the trajectory, also reduced the length of the trajectory. The shorter trajectory reduced the loss in accuracy due to poor control authority by subjecting the vehicle to fewer atmospheric dispersions.

The Shuttle entry guidance is designed to guide a mid L/D vehicle ( $L/D \approx 1.2$ ) from a low-Earth orbit to a runway landing. Although the Shuttle guidance has a much more aerodynamic vehicle to work with than Apollo, the accuracy requirements are much greater. The Shuttle guidance uses three control variables, bank angle, angle of attack, and a speed brake, to fly reference drag and altitude rate profiles. These reference profiles are analytically determined to attain the desired downrange and to avoid flight conditions which approach the heating and g-load limits. Assumptions concerning the vehicle performance and environment are used in determining these profiles prior to flight. The crossrange is controlled by bank reversals similar to

Apollo, but the reversals are based on the difference between the current heading and the heading to the target as opposed to the crossrange error.

Although not an entry guidance, Higgins' candidate aerobraking guidance for the Aeroassist Flight Experiment in [18] utilizes many concepts applicable to entry. The AFE vehicle enters the Earth's atmosphere from a high energy orbit comparable to a geosynchronous return orbit and skims through the upper portions of the atmosphere to reduce its energy. It then exits the atmosphere into a low Earth orbit. The aerobraking guidance uses only one control variable, bank angle, to target an apogee and plane for this orbit. A target orbital apogee is similar to a target downrange, while plane change capability is analogous to crossrange capability. This is because the desired apogee is dependent upon the magnitude of the in-plane lift just like downrange, and the change in orbital plane is effected by the lateral lift just like crossrange. This guidance uses the bank angle to control the magnitude of the in-plane lift to target to a desired apogee. Plane errors are corrected using any residual out-of-plane lift, and the direction of the out-of-plane lift is controlled by the sign of the bank angle. In this manner, the one control variable, bank angle, is used to affect two conditions.

In Higgins' guidance, the bank angle necessary to reach a target apogee is determined by a numeric predictor-corrector algorithm. A predictor-corrector algorithm computes control corrections based on predictions of the terminal conditions obtained by flying an assumed control profile. The use of a predictor-corrector implies a reference control profile (in the case of AFE, a constant bank angle profile), as opposed

to a reference trajectory. Reference trajectories, such as were used in the Apollo and Shuttle guidances, are excellent at controlling the vehicle energy state and reaching a target when there are few unknowns. However, this form of guidance can have difficulties if the vehicle deviates too far from the reference trajectory. This could happen if there are large variations from the expected conditions during entry, as is likely at Mars.

As implemented in the proposed AFE guidance, the predictor-corrector, using a reference bank profile, essentially recomputes a new reference trajectory each guidance cycle, and thus is able to better adapt to wide variations in atmospheric and vehicle conditions. A drawback of the reference control profile is that it guides the vehicle based on the predicted final state and does not concern itself with the intermediate states. The state of the vehicle at intermediate steps can be just as important as the terminal conditions, as there are continuous constraints, such as g-load and heating rate, which the guidance can violate while still achieving the desired terminal conditions.

The prediction algorithm used in the guidance could have been either analytic or numeric. An analytic predictor uses closed-form solutions of the equations of motion to predict the final state. However, in order to obtain the closed-form solutions, some simplifying assumptions must be made. This reduces the accuracy of the analytic predictions. The numeric predictor, which was chosen by Higgins for AFE, numerically integrates the equations of motion forward in time using assumed atmosphere and vehicle models and obtains highly accurate predictions. The cost of this accuracy is an

increased computational load. A numeric predictor-corrector can be very inefficient and computer-resource intensive if improperly designed. The numeric algorithm is now viable because computational abilities have greatly improved in the last decade, and more importantly, the basic algorithm was refined by Spratlin.

Spratlin recognized the capabilities of the numeric predictor-corrector type algorithm and applied this concept to entry with the Entry Research Vehicle in Reference [10]. The ERV was proposed to demonstrate synergetic plane change and precision entry capabilities with a high  $L/D$  ( $\approx 2.0$ ) vehicle at Earth. The ERV guidance is based upon linear bank angle with velocity and constant angle of attack control profiles. A numeric predictor-corrector determines the change in bank angle and angle of attack necessary to reach the desired crossrange and downrange. The commands are computed by solving a pair of simultaneous equations involving bank angle, angle of attack, and the sensitivity of these controls to the currently predicted downrange and crossrange errors. The heating rate is controlled explicitly during the short periods when heating is a problem. No attempt is made to control the energy level of the entry vehicle at the target.

A reference profile, if not closely followed, quickly diverges from the desired trajectory, so errors must be continuously fed back to recompute the commanded bank angle in an analytic reference trajectory guidance. Spratlin reasoned that the numeric predictor-corrector in the ERV guidance need not be called as frequently because the trajectory solution (the reference control profile) does not change as rapidly. The commanded bank angle is still determined every guidance cycle from the cur-

rent reference bank profile, but a new reference control profile is recomputed by the predictor-corrector at a much slower rate. This decreases the computational load. An additional improvement in the algorithm is the steps taken towards optimizing the guidance rate. The rate could be varied based on aerodynamic accelerations or time-to-go to produce a nearly constant load on the central processing unit. This allows the guidance scheme to be run at a slow rate early in the trajectory when the trajectory to be predicted is long and there is plenty of control margin. Later, when the time-to-go is short and control authority is small, thereby making frequent guidance updates necessary, the guidance should be run at a faster rate.

Previous Mars entry guidance studies have largely been devoted to low L/D entries such as those used by the Viking landers [19]. However, in Reference [5], Tigges has recently developed a precision entry scheme for a mid L/D vehicle at Mars. The guidance analytically predicts the equilibrium glide profile which gives the desired downrange. The crossrange is controlled by bank reversals based on the current crossrange error. The guidance consists of two phases. The first phase uses bank angle control only to meet the ranging constraints. Late in the trajectory, if the dynamic pressure limit is predicted to be exceeded, then the second phase is implemented. In the second phase, angle of attack modulation is used in addition to bank angle control to meet the ranging and dynamic pressure constraints.

## 4.2 Guidance Scheme

Precision landing requires robust control over the vehicle trajectory. As demonstrated in [5], the necessary control can be achieved at Mars by varying both the vehicle bank angle and angle of attack. However, because the ability to modify angle of attack adds complexity to an entry vehicle (as explained in Section 1.3), it is desirable to achieve precision entry using a vehicle with bank angle control only. Thus, this study has chosen to simplify the vehicle by reducing the control variables. The one remaining control variable has two components—the magnitude and sign of the bank angle—which must be used to reach the target and satisfy the constraints.

The constraints which must be met have been listed in Table 1.1. However, not all of the constraints must be actively controlled. For the entry initial conditions chosen (i.e. deorbit from a low circular orbit), g-loading and heating rate are not a major concern because the g-loads experienced during these entries are less than those expected upon launch at Earth, and the heating encountered is relatively benign and well within the capabilities of state of the art thermal protection systems. Active control of the final flight path angle was initially considered, but was later found unnecessary because shallow final flight path angles naturally resulted from the chosen guidance design.

The major constraints which the guidance must meet are final range from the target and final dynamic pressure. The final range error can be expressed as cross-range and downrange components. The two ranging components are assumed to be independently controllable in the guidance design, with the root-sum-squared of the

two errors at guidance termination indicating ranging performance. This results in a total of three constraints which the guidance must actively meet.

The guidance must not violate any of the listed constraints despite dispersions in the atmosphere and vehicle performance. The major dispersions which the guidance must be prepared to handle are off-nominal atmospheric densities, winds, and erroneous predictions in vehicle aerodynamics. The guidance must also maximize cross-range capability and conserve total ranging capability. As explained in Section 1.2, the crossrange capability is important to increase mission flexibility. The ability to conserve total ranging capability is also important because it is an indication of the ability of the guidance to handle dispersions later in the trajectory.

Prior to determining the general guidance scheme, it is necessary to know how the one control, bank angle, influences the constraints. The bank angle determines the orientation of the lift vector in the plane perpendicular to the relative velocity, and varying this angle apportions the lift between the in-plane (or vertical) and out-of-plane (or lateral) directions. The vertical lift affects both the downrange and final dynamic pressure. While the downrange distance is directly influenced by the vertical lift throughout the trajectory, the final dynamic pressure is not so obviously a result of the vertical lift. As discussed in Section 3.3.2, the dynamic pressure history during entry approximates a second-order system with a phugoid mode, and the final dynamic pressure is determined by the interaction of a number of factors, including bank profile (i.e. the vertical lift). The lateral lift affects the crossrange distance to be flown. Greater lateral lift, given the same vertical lift, results in greater crossrange.

However, vertical lift is also an important factor in crossrange because it determines how long the lateral lift has to act.

Since there are three constraints and only one control variable, trade-offs must be made. Design of the guidance begins with the downrange control. After control of the downrange constraint is established, control of the other two constraints will follow.

Downrange control is accomplished using a numeric predictor-corrector algorithm which controls the magnitude of the current bank angle based on the error in the final downrange obtained by flying an assumed bank history. The reference control profile and predictor-corrector algorithm were chosen over a reference trajectory guidance scheme based on the uncertainty in the Mars environment and the need for the adaptability that the predictor-corrector provides. The prediction was chosen to be performed numerically because of the increased accuracy over analytic predictions. Although not done here, the predictor-corrector execution rate and the prediction step size can both be optimized to reduce the computational load. With these upgrades, the computational requirements for the numeric predictor-corrector guidance are not excessive, and the scheme is a viable option for a Mars mission.

Given that the guidance will use a reference control profile, the type of reference control profile must be determined. The bank angle could be varied with time, but as explained in Section 3.2, a bank profile which varies linearly with velocity provides near maximum crossrange for a given downrange. This is the control profile which was used in [10] and chosen for this guidance. An added benefit of this profile is that

the vehicle flies near full lift up at the end of the trajectory, resulting in desirable shallow final flight path angles.

Crossrange control is achieved by using the lateral component of lift. The magnitude of the lateral component of lift is simply a by-product of the bank angle chosen by the downrange control logic. However, it is still possible to use whatever magnitude of lateral lift is available to meet the crossrange objectives by performing bank angle sign reversals. Changing the sign of the bank angle changes the direction of the lateral lift and allows the vehicle to control crossrange without placing demands on the magnitude of the bank angle.

The guidance uses an azimuth controller to constrain the crossrange. The controller determines the need for a roll reversal based on the current vehicle azimuth and azimuth to the target. A reversal is commanded when the difference between these values—the azimuth error—exceeds that which is necessary to ensure that the crossrange constraint will not be violated at the target. The allowable azimuth error decreases as the vehicle nears the target.

Since the crossrange controller uses lateral lift to satisfy its objectives, it is important that there always be some lateral lift available. The linear bank profile causes the vehicle to roll near full lift up at the end of the trajectory and eliminates the lateral component of lift at a very critical time. In order to ensure crossrange authority throughout the trajectory, the basic linear bank profile is modified to provide a minimum bank angle, as depicted in Figure 4.1. The minimum bank angle,  $\phi_{min}$ , ensures that there is always some lateral component of lift. This reduces the amount of ver-

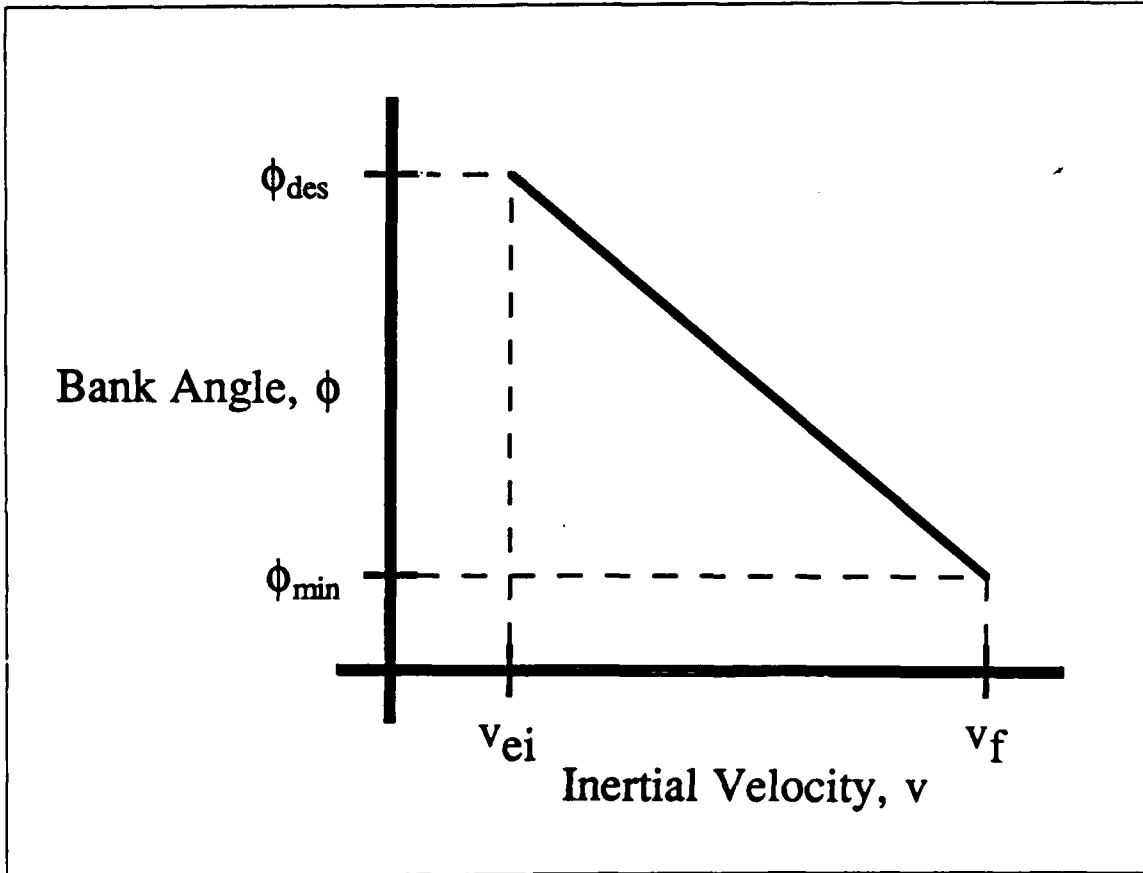


Figure 4.1. Linear Bank Profile with Minimum Bank Angle

tical lift which can be used to reach the downrange target by not allowing the vehicle to fly full lift-up, and decreases the vehicle maximum ranging capability. However, a minimum bank angle of  $15^\circ$  results in the loss of less than 4% of the vertical lift while maintaining approximately 25% of the available lift for lateral control. Therefore, downrange capability is only slightly affected, and the trade-off is advantageous.

The final dynamic pressure is the last constraint for which control is designed. As was seen in Chapter 3, final dynamic pressure is highly dependent on the vehicle design. Decreasing the vehicle ballistic coefficient will reduce the "steady-state" or median value of the final dynamic pressure, and if the vehicle is designed with a sufficiently small ballistic coefficient, the final dynamic pressure can be controlled passively. However, because decreasing the ballistic coefficient generally involves decreasing the lift-to-drag ratio and vehicle ranging capability, it is desirable to reduce the ballistic coefficient as little as necessary.

Another method of controlling the final dynamic pressure, as mentioned earlier in this chapter, is by varying the bank angle. However, the final dynamic pressure is relatively insensitive to the bank profile. The different bank profiles used to generate Figures 3.9 and 3.10 in Chapter 3 produced limited changes in the final dynamic pressure. Most of the variation in  $\bar{q}_f$  is due to the phugoid nature of the dynamic pressure during entry.

Because the "steady-state" value of final dynamic pressure is so highly vehicle dependent and relatively independent of the bank angle, significant changes cannot be effected by varying the bank angle. However, smaller changes in  $\bar{q}_f$  could be

accomplished if the magnitude of the oscillations in the phugoid were reduced. If the entry vehicle is designed to satisfy the dynamic pressure constraint for most trajectories, the guidance could be able to effect small changes in the vertical lift to satisfy the constraint for the remaining dispersed cases without disturbing the downrange control.

In order to do this, an analytic dynamic pressure controller was developed which reduces the oscillation by driving the dynamic pressure to a constant value. This controller is similar in design to the altitude controller in [9] and the heat rate controller in [10]. While the downrange portion of the guidance determines the bank angle, and thus the vertical component of lift, which is necessary to reach the target in downrange, the dynamic pressure controller determines a change in that vertical component of lift in order to satisfy the dynamic pressure constraints. This small change or deviation in the vertical component of lift shows up as a sinusoid on the linear bank profile due to the oscillatory nature of the dynamic pressure history.

The sign of the commanded bank angle,  $S_\phi$ , is determined by the azimuth controller, and the magnitude of the commanded bank angle is computed using input from the downrange and dynamic pressure controllers. The commanded bank angle is computed as,

$$\phi_{cmd} = S_\phi \arccos [\cos \phi_d + \delta (\cos \phi_{\bar{q}})] \quad (4.1)$$

where  $\cos \phi_d$  is the downrange lift fraction—the fraction of the currently available lift which should be in-plane in order to reach the desired downrange, and  $\delta (\cos \phi_{\bar{q}})$  is the dynamic pressure lift fraction—the change in the in-plane fraction of the currently

available lift which is desired to drive the dynamic pressure to the target value. The dynamic pressure controller determines  $\delta(\cos \phi_{\bar{q}})$ , while the downrange controller computes  $\cos \phi_d$ .

### 4.3 Downrange Control

The input of the downrange controller towards determining the commanded bank angle is  $\cos \phi_d$ , the fraction of the currently available lift which should be in-plane in order to reach the desired downrange. As explained in the previous section, downrange control is provided by a numeric predictor-corrector algorithm assuming a linear bank angle with velocity profile. The equation for the bank profile used is,

$$\phi_d = \phi_{des} \left( \frac{v - v_f}{v_{ei} - v_f} \right) + \phi_{min} \quad (4.2)$$

where  $v_{ei}$  and  $v_f$  are determined based on the expected trajectory and  $\phi_{min}$  is driven by the vehicle capabilities.  $v_f$  is chosen a little smaller than the actual expected final velocity to allow for dispersions in the final velocity.

The predictor and corrector functions work together to determine the particular bank profile to be flown. Since a particular bank profile is defined by its initial bank angle,  $\phi_{des}$ , a new control profile can be created by simply changing  $\phi_{des}$ . The corrector determines the change in  $\phi_{des}$  that will null the downrange error. This  $\Delta\phi_{des}$  is based on the currently predicted downrange error and the sensitivity of the downrange error to changes in  $\phi_{des}$ . The predictor flies out the trajectory using the current bank profile defined by  $\phi_{des}$  in order to determine the currently predicted downrange error.

The predictor also flies out a trajectory using a bank profile perturbed in  $\phi_{des}$ . The results of these two predictions are used by the corrector to determine the sensitivity of the downrange error to changes in  $\phi_{des}$ . The procedure that the predictor and the corrector follow in the process of determining a new bank profile is summarized below.

1. Set predictor desired bank angle to current desired bank angle,  $\phi_{des}$
2. Set predictor initial state to current navigation state
3. Predict downrange error at 5 km altitude
4. Set predictor desired bank angle to  $\phi_{des} + \delta\phi_{des}$
5. Repeat Steps 2 and 3
6. Using results of Steps 3 and 5, compute the sensitivity of downrange to desired bank angle
7. Compute  $\Delta\phi_{des}$  based on the results of Steps 3 and 6
8. Determine the new  $\phi_{des}$  from the old value and the result of Step 7

Once a bank profile has been chosen by the predictor-corrector, Equation 4.2 and the current inertial velocity are all that is necessary to determine the downrange bank angle,  $\phi_d$ . The downrange lift fraction is simply the cosine of this angle.

The downrange controller is executed once at entry interface to set the magnitude of the initial bank angle command. In order to save computational work, the controller

is not executed again until the aerodynamic g-load exceeds a trigger value,  $g_{begin}$ . Although the downrange controller produces a new value for  $\cos \phi_d$  each guidance cycle after this, the predictor-corrector is not executed this frequently due to the large control authority available and the short time between predictions over which dispersions act to perturb the trajectory. Early in the entry when the predicted trajectories are long and computationally intensive, the predictor-corrector execution rate is scaled back to a slower rate,  $R_{slw}$ . Later in the entry, when more frequent updates are desirable, the execution rate is increased to  $R_{fst}$ . The fast execution rate begins once the vehicle is below a given altitude,  $h_{cfst}$ , and continues until the downrange guidance is frozen at an altitude designated  $h_{cfrz}$ . The value for each of these rates and altitudes is dependent upon the vehicle and the trajectory, and is parametrically determined.

The operation of the predictor and corrector functions is the subject of the next two sections.

#### 4.3.1 Corrector

The corrector determines the sensitivity of downrange to changes in the desired bank angle, and based on this sensitivity and the currently predicted downrange error determines the proper  $\phi_{des}$ . The equations which are used to implement this strategy are derived in this section.

Expressing the downrange error in a Taylor series expansion of the desired bank angle and neglecting second order and higher terms yields,

$$\Delta DR_e = \frac{\partial DR_e}{\partial \phi_{des}} \Delta \phi_{des} \quad (4.3)$$

In order to null the downrange error, the desired change in downrange error must be equal to the negative of the predicted downrange error,

$$\Delta DR_e = -DR_e \quad (4.4)$$

The above equations combine to yield the incremental change in the desired bank angle which will null the downrange error:

$$\Delta \phi_{des} = -DR_e \left[ \frac{\partial DR_e}{\partial \phi_{des}} \right]^{-1} \quad (4.5)$$

The partial derivative in the previous equation can be approximated by the following finite difference equation,

$$\frac{\partial DR_e}{\partial \phi_{des}} = \frac{DR_e(\phi_{des} = \phi_{des\,pert}) - DR_e(\phi_{des} = \phi_{des\,cur})}{\phi_{des\,pert} - \phi_{des\,cur}} \quad (4.6)$$

where  $DR_e(\phi_{des} = \phi_{des\,cur})$  is the downrange error predicted using the current bank profile, and  $DR_e(\phi_{des} = \phi_{des\,pert})$  is the downrange error predicted using a perturbed bank angle profile.

The current and perturbed bank profiles are defined by,

$$\phi_{des\,cur} = \phi_{des}' \quad (4.7)$$

and,

$$\phi_{des\,pert} = \phi_{des}' + \delta \phi_{des} \quad (4.8)$$

where  $\phi_{des}'$  is the desired bank angle from the previous guidance execution, and  $\delta\phi_{des}$  is a small perturbation in desired bank angle.

Based upon the results of the predicted trajectories and Equation 4.5, the updated downrange guidance command is,

$$\phi_{des} = \phi_{des}' + \Delta\phi_{des} \quad (4.9)$$

Near the end of the trajectory, the downrange becomes very insensitive to changes in  $\phi_{des}$  and the partial derivative in Equation 4.5 becomes very small. Even for small downrange errors, the required incremental change in desired bank angle becomes unreasonably large, and this causes the guidance to become unstable. In order to deal with this instability, there are three options.

At some point in the trajectory prior to the development of the instability, the guidance can be frozen. Once the partial decreases below a specified value, the predictor-corrector is no longer executed, and the control profile remains constant. This avoids the instability, but the guidance loses its ability to adapt to winds—which become a major factor as the vehicle slows down—and other dispersions in the environment. Because the instability generally occurs with significant time and range remaining in the trajectory, the guidance must be frozen early—allowing the expected dispersions to cause large range errors. Since precision is critical, freezing the guidance is not satisfactory.

It is also possible to move the target aim point below the required parachute deployment altitude so that the instability is not encountered. Since control authority is lost relatively early in the trajectory, this solution would require an aim point

significantly displaced from the desired terminal location. This is undesirable because the guidance only controls to a final state and not to an intermediate state, so that the actual final conditions will differ greatly from the predicted termination conditions.

The third and chosen option is to limit the magnitude of the incremental change in desired bank angle. Although the partial is still allowed to get small, the instability that the shrinking partial causes is avoided by limiting the change in  $\phi_{des}$  each guidance cycle. This method allows the guidance to remain responsive to dispersions throughout the trajectory. However, it is not desirable to limit the change in desired bank angle until the guidance has clearly established itself on the desired trajectory. Therefore, the limiter is not implemented until the vehicle has slowed below a specified velocity,  $V_{\phi_{lim}}$ . The magnitude of the limit,  $\Delta\phi_{lim}$ , and the appropriate velocity,  $V_{\Delta\phi_{lim}}$ , are specific to the vehicle and trajectory and are empirically determined. Additionally, in the case of navigation updates, it may be desirable to allow large changes in the desired bank angle late in the trajectory. Although not implemented here, it would be possible to increase the size of the incremental limit to allow such changes based on knowledge that an update has occurred. There could be difficulties with this due to the instability of the predictor-corrector, but they might be handled with appropriate tests regarding the relative movement of the target.

Regardless of location in the trajectory, it is possible that the downrange could become completely insensitive to changes in the bank angle, and the partial derivative in Equation 4.5 will become zero. This corresponds to a complete loss of control authority. If this does occur, the incremental change in desired bank angle is simply

set to zero and the resulting desired bank angle is the same as commanded in the previous guidance cycle.

### 4.3.2 Predictor

The corrector requires predicted downrange errors, as provided by the predictor, to determine the new desired bank angle. The predictor is a simplified 3-DOF trajectory simulator. Using the current bank angle profile, it numerically integrates the vehicle equations of motion from the current time and state until encountering termination conditions. The equations of motion to be integrated are,

$$\frac{d\vec{r}}{dt} = \vec{v} \quad (4.10)$$

$$\frac{d\vec{v}}{dt} = \vec{a}_{tot} \quad (4.11)$$

where the predictor initial conditions are the current navigation estimates of position and velocity,

$$\vec{r}_o = \hat{r}(t_{cur}) \quad (4.12)$$

$$\vec{v}_o = \hat{v}(t_{cur}) \quad (4.13)$$

The total acceleration on the vehicle is the sum of the gravitational and aerodynamic accelerations,

$$\vec{a}_{tot} = \vec{a}_g + \vec{a}_{aero} \quad (4.14)$$

The gravitational acceleration, which includes the effect of the  $J_2$  term, is,

$$\vec{a}_g = -\frac{\mu_m}{|\vec{r}|^2} \vec{i}_g \quad (4.15)$$

where,

$$\vec{i}_g = \vec{i}_r + \frac{3}{2} J_2 \frac{r_{eq}^2}{|\vec{r}|^2} \left( (1 - 5z^2) \vec{i}_r + 2z \vec{i}_{pole} \right) \quad (4.16)$$

$$z = \vec{i}_r \cdot \vec{i}_{pole} \quad (4.17)$$

$$\vec{i}_r = \frac{\vec{r}}{r} \quad (4.18)$$

and,

$$\vec{i}_{pole} = \frac{\vec{r}_{pl}}{r_{pl}} \quad (4.19)$$

The purpose of the prediction is to determine downrange capability. Since the out-of-plane component of lift does not significantly contribute to the downrange capability, the acceleration due to the out-of-plane component of lift can be neglected in the prediction. Thus, the aerodynamic accelerations can be written in terms of the drag and vertical lift components of acceleration as such,

$$\vec{a}_{aero} = a_{drag} \vec{i}_{drag} + a_{lift} \vec{i}_{lift} \quad (4.20)$$

where,

$$a_{drag} = \frac{C_D \bar{q} S}{m} \quad (4.21)$$

or,

$$a_{drag} = \frac{\bar{q}}{C_B} \quad (4.22)$$

depending on the method of vehicle definition, and

$$a_{lift} = \left( \frac{L}{D} \right)_p a_{drag} \cos \phi_p \quad (4.23)$$

$$\bar{q} = \frac{1}{2} \rho_p v_{rel}^2 \quad (4.24)$$

$$v_{rel}^2 = \vec{v}_{rel} \cdot \vec{v}_{rel} \quad (4.25)$$

$$\vec{v}_{rel} = \vec{v} - (\vec{\omega}_m \times \vec{r}) \quad (4.26)$$

$$\vec{i}_{drag} = -\vec{i}_{v_{rel}} \quad (4.27)$$

$$\vec{i}_{v_{rel}} = \frac{\vec{v}_{rel}}{|\vec{v}_{rel}|} \quad (4.28)$$

$$\vec{i}_{lift} = \cos \phi_p (\vec{i}_{v_{rel}} \times \vec{i}_r) \times \vec{i}_{v_{rel}} \quad (4.29)$$

and  $\phi_p$  is the bank angle at any instant in the trajectory based on the bank angle profile,

$$\phi_p = \phi_{des} \left( \frac{v - v_f}{v_{ei} - v_f} \right) + \phi_{min} \quad (4.30)$$

where  $v_{ei}$ ,  $v_f$ , and  $\phi_{min}$  are the same values used to define the actual bank profile, and  $v$  is the prediction estimate of inertial velocity.

Current estimates of the vehicle lift-to-drag ratio,  $\left(\frac{L}{D}\right)_p$ , and the atmospheric density,  $\rho_p$ , are determined as explained in the subsection, "Density and L/D Estimation".

### Predictor Integration Step Size

The predictor uses two different integration step sizes. A large time step,  $\Delta t_{big}$ , above an altitude of  $h_{\Delta t_{small}}$  in the predicted trajectory, and a small step size,  $\Delta t_{small}$ , below this altitude. The large step size reduces computational intensity at a small price of reduced accuracy. The difference in the integration accuracy using the large and small time steps is not significant, and the only reason a small time step was used was to obtain homogeneity in the terminal altitude.

## Density and L/D Estimation

The accuracy of the predictor depends on the accuracy of the vehicle and environment models. Thus, it is important that off-nominal conditions in these models are taken into account. This section explains how the density and lift-to-drag ratio values used in the predictor are determined.

The predictor uses a table look-up implementation of a model atmosphere to determine the expected density throughout the predicted trajectory. The actual density encountered during entry will vary from this model, and to compensate for these density dispersions, the density used in the predictor is modelled as,

$$\rho_p = K_\rho \rho_{nom} \quad (4.31)$$

where  $\rho_{nom}$  is the density determined from the nominal atmosphere model as a function of altitude and  $K_\rho$  is a density scale factor which is the ratio of the measured density to the expected nominal density,

$$K_\rho = \frac{\hat{\rho}}{\rho_{nom}} \quad (4.32)$$

The actual density encountered is estimated based on the measured drag acceleration, the navigation relative velocity, and the nominal ballistic coefficient as,

$$\hat{\rho} = \frac{2|\hat{a}_{drag}|}{|\hat{v}_{rel}|^2} \left( \frac{m}{C_D S} \right)_{nom} \quad (4.33)$$

where the measured drag is determined from the inertial measurement unit (IMU)

sensed acceleration,  $\vec{a}_{IMU}$ , as,

$$|\hat{a}_{drag}| = -\vec{a}_{IMU} \cdot \frac{\hat{v}_{rel}}{|\hat{v}_{rel}|} \quad (4.34)$$

Because there will be short term variations in the density, and other error sources which will cause noise in the measured drag term, the density scale factor must be filtered, and the result of Equation 4.32 is not actually used. The actual value used in Equation 4.31 is the output of a first-order low-pass filter,

$$K_{\rho}^{+} = (1 - K_1) K_{\rho}^{-} + K_1 \frac{\hat{\rho}}{\rho_{nom}} \quad (4.35)$$

The gain used in this filter is determined using,

$$K_1 = 1 - e^{-\left(\frac{\Delta t}{\tau_{\rho}}\right)} \quad (4.36)$$

where  $\Delta t$  is the time between successive acceleration measurements, and  $\tau_{\rho}$  is the time constant selected to attenuate the high frequency noise, yet allow sufficient response to changes in the density. Also, for the first pass through the guidance, the value for  $K_{\rho}$  must be initialized to 1.

Since the equation for the measured density uses the nominal ballistic coefficient and the navigation relative velocity, errors in these values appear as density dispersions. Hence, the density estimator allows the predictor, and thus the guidance, to be responsive to errors in ballistic coefficient and relative velocity, as well as density dispersions.

The lift-to-drag ratio will predominantly be in error due to the inability to properly predict the pitch moment coefficient. Errors in determining the pitch moment

coefficient,  $C_{m_0}$ , cause the vehicle to trim at an off-nominal angle of attack which results in an off-nominal L/D. The error in L/D induced by  $C_{m_0}$ , as well as the errors in simply predicting  $C_L$  and  $C_D$ , are the drivers behind the need to estimate the vehicle L/D for use in the prediction.

The lift-to-drag ratio used in the predictor is modeled as,

$$\left(\frac{L}{D}\right)_p = K_{\frac{L}{D}} \frac{L}{D}_{nom} \quad (4.37)$$

where  $\frac{L}{D}_{nom}$  is the expected lift-to-drag ratio at the current time, and  $K_{\frac{L}{D}}$  is the ratio of sensed L/D to expected L/D,

$$K_{\frac{L}{D}} = \frac{\hat{\frac{L}{D}}}{\frac{L}{D}_{nom}} \quad (4.38)$$

The expected  $\frac{L}{D}_{nom}$  is computed in the prediction using a table look-up with linear interpolation between points to determine the vehicle aerodynamic coefficients based on the navigation estimate of trim angle of attack. The actual L/D of the vehicle can be estimated using the measured drag and lift accelerations as,

$$\frac{\hat{L}}{\hat{D}} = \frac{|\hat{a}_{lift}|}{|\hat{a}_{drag}|} \quad (4.39)$$

with the measured accelerations determined from the IMU as in Equation 4.34 and below,

$$|\hat{a}_{lift}| = \sqrt{\vec{a}_{IMU} \cdot \vec{a}_{IMU} - |\hat{a}_{drag}|^2} \quad (4.40)$$

As is the case with the density estimator, there will be short-term variations in the acceleration measurements. These high-frequency variations must not be incor-

porated into the prediction through the L/D estimation because they would cause erroneous predictions. This noise can be eliminated using a low-pass filter similar to that developed for the density estimator, and this result is used in Equation 4.37,

$$K_{\frac{L}{D}}^+ = (1 - K_2) K_{\frac{L}{D}}^- + K_2 \frac{\hat{L}}{L} \frac{\bar{D}}{\bar{D}_{nom}} \quad (4.41)$$

where the gain is determined using,

$$K_2 = 1 - e^{-\left(\frac{\Delta t}{\tau_{\frac{L}{D}}}\right)} \quad (4.42)$$

The time constant,  $\tau_{\frac{L}{D}}$ , is parametrically determined to give satisfactory response to variations in L/D, and the initial value of  $K_{\frac{L}{D}}$  is 1.

A note worth mentioning here is that the vehicle model is constant throughout the predicted trajectory because the simulator used a constant vehicle model. In actuality, the performance capabilities of an entry vehicle vary with flight regime, and the prediction would probably require several different models used along different portions of the trajectory in order to properly simulate vehicle performance. The constant vehicle modeling was deemed sufficient for the demonstration of guidance capabilities, since the objective of this study is not to develop a flight-quality algorithm.

### Final State Error Computations

The downrange error in the predictor is computed as the difference between the current surface range to the target and the currently predicted surface range to be

flown. This is graphically illustrated in Figure 4.2. Since the predicted trajectory is

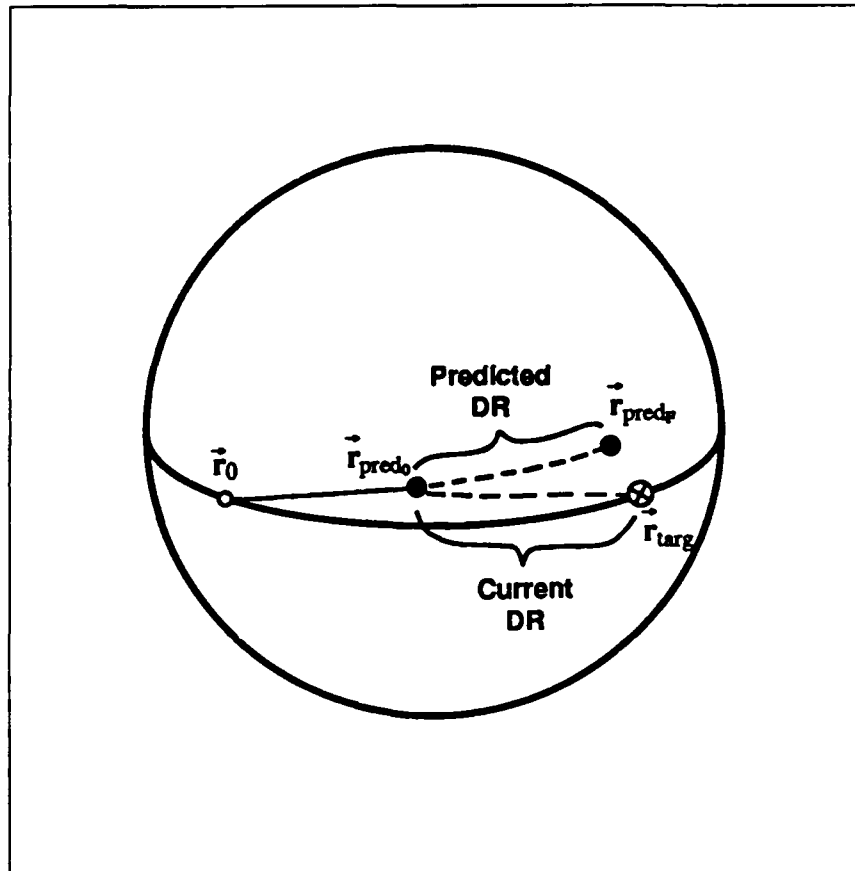


Figure 4.2. Downrange Error Definition

flown using only the in-plane or vertical component of lift, the surface range to the predicted final position represents the vehicle's downrange capability only—with no crossrange component.

In order to determine the downrange error, the current position (which is also the initial predictor position), the predicted final position, and the target position

all must be known in a planet-fixed coordinate system. Relating these vectors in the inertial frame in which they are otherwise used is not useful because of the rotation of Mars.

First, the target position vector must be determined in planet-fixed coordinates from the map coordinates and altitude. Since the map coordinates are given using  $\phi_{gd}$ , the geodetic latitude, the geocentric latitude,  $\phi_{gc}$ , must be computed using,

$$\phi_{gc} = \arctan \left( \frac{\tan(\phi_{gd})}{k} \right) \quad (4.43)$$

where,

$$k = \left( \frac{1}{1 - f_m} \right)^2 \quad (4.44)$$

and the planet-flattening term which describes the eccentricity of the planet is,

$$f_m = 1 - \left( \frac{r_{pl}}{r_{eq}} \right) \quad (4.45)$$

Based on the longitude,  $\lambda$ , and geocentric latitude, a unit vector in the direction of the target is computed as,

$$\vec{i}_{tgt} = \begin{bmatrix} \cos(\phi_{gc}) \cos(\lambda) \\ \cos(\phi_{gc}) \sin(\lambda) \\ \sin(\phi_{gc}) \end{bmatrix} \quad (4.46)$$

Then, the target vector is computed from,

$$\vec{r}_{tgt} = r_{tgt} \vec{i}_{tgt} \quad (4.47)$$

where the magnitude of the target vector is the sum of the distance to the planet surface,  $r_s$ , and the target altitude. The distance to the planet surface at the target

location is based on an ellipsoidal planet model, and is computed as,

$$r_s = r_{eq} \frac{1 - f_m}{\sqrt{1 - f_m (2 - f_m) (1 - (\vec{v}_{tgt} \cdot \vec{v}_{pole})^2)}} \quad (4.48)$$

Next, the initial and final predictor position vectors are transformed to the planet-fixed reference frame as shown below.

$$\vec{\Gamma}_{\text{PRED}_0}^{\text{PF}} = M_I^{\text{PF}} \vec{\Gamma}_{\text{PRED}_0} \quad (4.49)$$

$$\vec{\Gamma}_{\text{PRED}_f}^{\text{PF}} = M_I^{\text{PF}} \vec{\Gamma}_{\text{PRED}_f} \quad (4.50)$$

where the transformation matrix between inertial and planet-fixed coordinates is determined using  $t_{ep}$ , the time since some epoch when the orientation of Mars is known, and  $\omega_m$ , the rotation rate of Mars, as,

$$M_I^{\text{PF}} = \begin{bmatrix} \cos(\omega_m t_{ep}) & -\sin(\omega_m t_{ep}) & 0 \\ \sin(\omega_m t_{ep}) & \cos(\omega_m t_{ep}) & 0 \\ 0 & 0 & 1 \end{bmatrix} \quad (4.51)$$

The three position vectors of concern are then unitized,

$$\hat{\Gamma}_{\text{PRED}_0}^{\text{PF}} = \frac{\vec{\Gamma}_{\text{PRED}_0}^{\text{PF}}}{|\vec{\Gamma}_{\text{PRED}_0}^{\text{PF}}|} \quad (4.52)$$

$$\hat{\Gamma}_{\text{PRED}_f}^{\text{PF}} = \frac{\vec{\Gamma}_{\text{PRED}_f}^{\text{PF}}}{|\vec{\Gamma}_{\text{PRED}_f}^{\text{PF}}|} \quad (4.53)$$

$$\hat{\Gamma}_{\text{tgt}}^{\text{PF}} = \frac{\vec{\Gamma}_{\text{tgt}}^{\text{PF}}}{|\vec{\Gamma}_{\text{tgt}}^{\text{PF}}|} \quad (4.54)$$

and the results are used in the following equations which determine the predicted range angle and the current target range angle.

$$\theta_p = \arccos(\hat{r}_{\text{PRED}_o}^{\text{PF}} \cdot \hat{r}_{\text{PRED}_t}^{\text{PF}}) \quad (4.55)$$

$$\theta_{tgt} = \arccos(\hat{r}_{\text{PRED}_o}^{\text{PF}} \cdot \hat{r}_{tgt}^{\text{PF}}) \quad (4.56)$$

The difference between the predicted and target range angles is the range angle error, as shown below.

$$\theta_{err} = \theta_p - \theta_{tgt} \quad (4.57)$$

The downrange error is then the product of the range angle error and the planet equatorial radius.

$$DR_e = \theta_{err} r_{eq} \quad (4.58)$$

This equation assumes a spherical Mars. Although this is not the case, the equation works well because the error angle is small. By the definition of predicted downrange error, a negative error means that the vehicle is predicted to hit short of the target and a positive error is past the target.

## 4.4 Crossrange Control

The final crossrange is controlled by limiting the deviation of the vehicle azimuth from the azimuth to the target. If the vehicle is exceeding the azimuth error limit and the current  $\phi_{cmd}$  is causing the error to increase, a bank reversal is called for.

The magnitude of the maximum allowable azimuth error is a function of the vehicle velocity and is defined by the azimuth error corridor in Figure 4.3. Initially, the

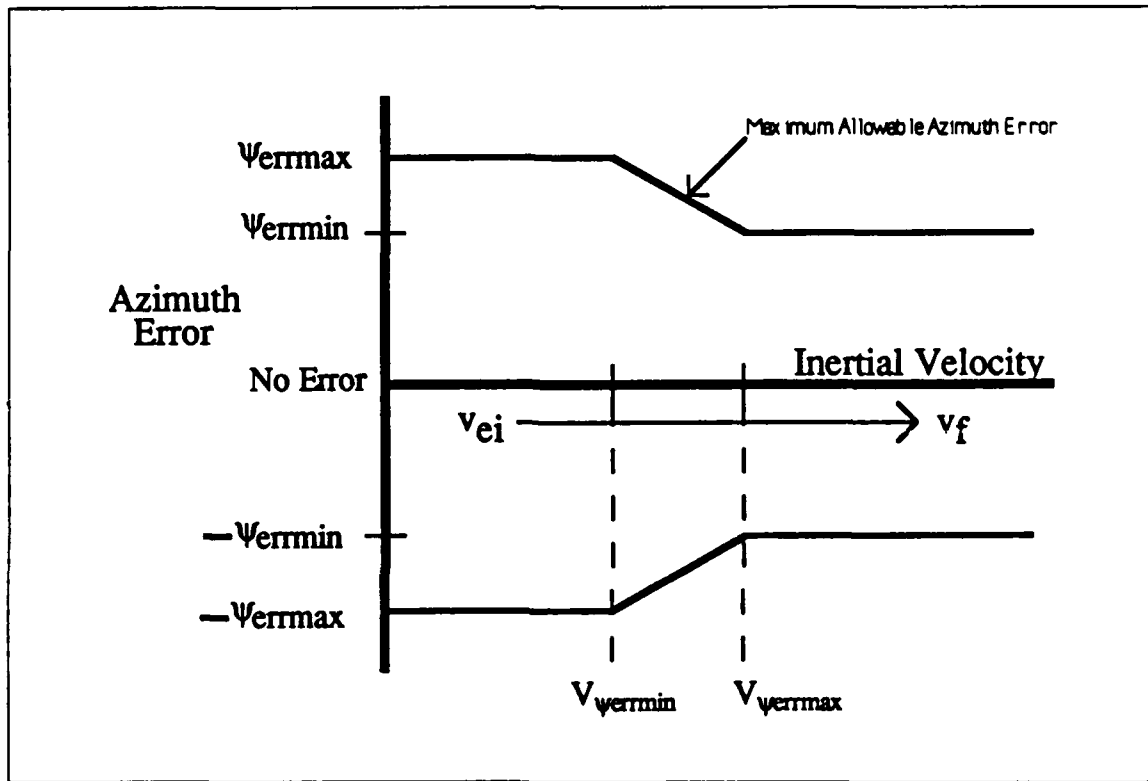


Figure 4.3. Azimuth Error Corridor

allowable azimuth error is  $\psi_{errmax}$ . This value is chosen to keep the vehicle in the general direction of the target, but not to so tightly limit the heading as to cause excessive bank reversals. As the vehicle nears the target, it is necessary to reduce the allowable error. At an inertial velocity of  $V_{\psi_{errmax}}$ , the error limit begins ramping down to a smaller limit,  $\psi_{errmin}$ , which is obtained at the velocity  $V_{\psi_{errmin}}$ . These values

which define the azimuth error corridor are constants and are empirically determined.

The crossrange controller is executed once at entry interface to ensure that the vehicle is initially turning in the proper direction, and then waits until the g-loads exceed the starting value,  $g_{begin}$ , to start running at the continuous rate of 1 Hz.

The current azimuth is determined by first converting the inertial relative velocity vector into a North-East-Down coordinate frame. This is done using,

$$\vec{v}_{rel}^{NED} = M_I^{NED} \vec{v}_{rel} \quad (4.59)$$

where,

$$M_I^{NED} = \begin{bmatrix} \frac{\vec{i}_{pole} \times \vec{r}}{|\vec{i}_{pole} \times \vec{r}|} \times (-\vec{i}_r) & \frac{\vec{i}_{pole} \times \vec{r}}{|\vec{i}_{pole} \times \vec{r}|} & -\vec{i}_r \end{bmatrix} \quad (4.60)$$

In the North-East-Down frame, the north and east components of velocity are then used to find the vehicle's compass heading from north,

$$\psi_{cur} = \arctan \left( \frac{v_{rel_x}^{NED}}{v_{rel_y}^{NED}} \right) \quad (4.61)$$

The heading to the target is found by determining the vector normal to the plane which contains both the current vehicle position vector and the target vector in planet-fixed coordinates,

$$\vec{r}_\perp = \vec{r}^{PF} \times \vec{r}_{tgt} \quad (4.62)$$

where,

$$\vec{r}^{PF} = M_I^{PF} \vec{r} \quad (4.63)$$

From this normal vector, the azimuth to the target is computed as,

$$\psi_{tgt} = \arctan \left( \frac{r_{\perp_x} r_y - r_{\perp_y} r_x}{r_{\perp_z} r} \right) \quad (4.64)$$

The current azimuth error is simply the difference between the current vehicle azimuth and the azimuth to the target as defined by,

$$\psi_{err} = \psi_{cur} - \psi_{tgt} \quad (4.65)$$

If the magnitude of the error is greater than  $180^\circ$ , then the error is in the opposite direction, and the error is corrected based on,

$$\psi_{err} = \psi_{err} - 360^\circ \text{sign}(\psi_{err}) \quad (4.66)$$

Based on the definition, a positive azimuth error for an easterly trajectory implies the vehicle will fly south of the target. In this case, a bank reversal will be commanded only if the azimuth error is greater than the allowable limit and the currently commanded bank angle,  $\phi_{cmd}$ , is positive. This second check, which determines whether the current bank angle is increasing or decreasing the azimuth error, is used to ensure only one reversal is commanded for each excursion beyond the allowable azimuth limit.

A bank reversal is commanded through the azimuth controller by multiplying the current sign of the bank angle,  $S_\phi$ , by -1.  $S_\phi$  is originally set to be the sign of the initial bank angle and then switches sign whenever a bank reversal is needed. An updated value for  $S_\phi$  is determined once per second when the guidance is cycling.

## 4.5 Dynamic Pressure Control

The dynamic pressure controller uses an analytic control law to compute deviations from the linear bank profile which will satisfy the final dynamic pressure constraints.

The output of this controller is  $\delta(\cos \phi_{\bar{q}})$  which is a desired change in the in-plane fraction of the currently available lift.

The analytic control law reduces the oscillation in the dynamic pressure by driving the dynamic pressure to a desired rate,  $\dot{\bar{q}}_{tgt}$ , and constant value,  $\bar{q}_{tgt}$ .

$$\delta(\cos \phi_{\bar{q}}) = \frac{K_{\dot{\bar{q}}}}{\bar{q}} (\dot{\bar{q}} - \dot{\bar{q}}_{tgt}) + \frac{K_{\bar{q}}}{\bar{q}} (\bar{q} - \bar{q}_{tgt}) \quad (4.67)$$

This control law feeds back dynamic pressure and the time rate of change of dynamic pressure to determine the change in the lift fraction necessary to provide a second order control response. Since a constant dynamic pressure is desired,

$$\dot{\bar{q}}_{tgt} = 0 \quad (4.68)$$

The simplified analytic dynamic pressure control law is,

$$\delta \cos \phi_{\bar{q}} = \frac{K_{\dot{\bar{q}}}}{\bar{q}} \dot{\bar{q}} + \frac{K_{\bar{q}}}{\bar{q}} (\bar{q} - \bar{q}_{tgt}) \quad (4.69)$$

The dynamic pressure controller provides inputs to the commanded bank angle at a rate of 1 Hz once the aerodynamic acceleration exceeds the trigger,  $g_{begin}$ . However, it is desirable to use the dynamic pressure controller only when necessary to reduce  $\bar{q}_f$  because the dynamic pressure controller competes with the downrange controller in determining the magnitude of the bank angle. Thus, the control law is implemented only when the predicted  $\bar{q}_f$  is near or above the desired limit. More specifically, the controller is implemented when the predicted final dynamic pressure,  $\bar{q}_{fp}$ , exceeds

some fraction of the limit, or when

$$\bar{q}_{fp} > K_{\bar{q}_f} \bar{q}_{lim} \quad (4.70)$$

where  $K_{\bar{q}_f}$  is a fraction which is empirically determined to ensure the controller is implemented when needed despite errors in the predicted final dynamic pressure.

The predicted final dynamic pressure is derived from the downrange control predictor terminal conditions as,

$$\bar{q}_{fp} = \frac{1}{2} \rho_p v_{relp}^2 \quad (4.71)$$

Additionally, the controller is not executed until the vehicle velocity has decreased below a value,  $V_{dmp}$ , which ensures that the vehicle has sufficiently entered the atmosphere. When used at low dynamic pressures the controller tries to drive the dynamic pressure too quickly and causes downrange control to be lost.

#### 4.5.1 Gain Determination

In order to obtain values for the gains in the controller, and to demonstrate that the dynamic pressure response can be described as a second-order system, we start by writing the radial position equation of motion for a point mass entry vehicle,

$$m\ddot{h} = L_v + \frac{m(\cos \gamma v)^2}{r} - mg \quad (4.72)$$

where  $L_v$  is the vertical component of the lift determined by,

$$L_v = C_L \bar{q} S \cos \phi \cos \gamma \quad (4.73)$$

Assuming a small flight path angle yields,

$$\ddot{h} = \frac{C_L \bar{q} S}{m} \cos \phi + \frac{v^2}{r} - g \quad (4.74)$$

Since the term  $\cos \phi$  represents the portion of available lift which is in the vertical direction, it can be written as the sum of the downrange lift fraction and the change in the lift fraction desired by the dynamic pressure controller as,

$$\cos \phi = \cos \phi_d + \delta (\cos \phi_{\bar{q}}) \quad (4.75)$$

Combining Equations 4.74 and 4.75 yields the radial position equation of motion containing the lift fractions from both controllers,

$$\ddot{h} = \frac{C_L \bar{q} S}{m} [\cos \phi_d + \delta (\cos \phi_{\bar{q}})] + \frac{v^2}{r} - g \quad (4.76)$$

Since the dynamic pressure controller will cause some perturbation in altitude,

$$h = h_d + \delta h \quad (4.77)$$

and by differentiating twice,

$$\ddot{h} = \ddot{h}_d + \delta \ddot{h} \quad (4.78)$$

The in-plane equation of motion becomes,

$$\ddot{h}_d + \delta \ddot{h} = \frac{C_L \bar{q} S}{m} [\cos \phi_d + \delta (\cos \phi_{\bar{q}})] + \frac{v^2}{r} - g \quad (4.79)$$

Without the dynamic pressure controller, the in-plane equation of motion would simply be,

$$\ddot{h}_d = \frac{C_L \bar{q} S}{m} [\cos \phi_d] + \frac{v^2}{r} - g \quad (4.80)$$

Subtracting the contribution of the downrange controller, Equation 4.80, from Equation 4.79 yields the perturbations which are due to the dynamic pressure controller only.

$$\delta \ddot{h} - \frac{C_L \bar{q} S}{m} [\delta (\cos \phi_{\bar{q}})] = 0 \quad (4.81)$$

Substituting the control law, Equation 4.69, into the above equation yields,

$$\delta \ddot{h} - \left[ \frac{C_L \bar{q} S}{m} \right] \left[ K_{\dot{q}} \dot{\bar{q}} + K_{\bar{q}} (\bar{q} - \bar{q}_{tgt}) \right] = 0 \quad (4.82)$$

In order to linearize this equation in altitude, the dynamic pressure and dynamic pressure rate terms must be expressed linearly in terms of altitude. This can be done by taking a Taylor Series expansion of the density term in the simple dynamic pressure equation.

$$\bar{q} = \frac{1}{2} \left[ \rho(h^*) + \left. \frac{\partial \rho}{\partial h} \right|_{h^*} \delta h \right] v_{rel}^2 \quad (4.83)$$

An expression for the dynamic pressure rate is obtained by assuming that the time rate of change of relative velocity is small compared to the change in density, and differentiating,

$$\dot{\bar{q}} = \frac{1}{2} v_{rel}^2 \left. \frac{\partial \rho}{\partial h} \right|_{h^*} \dot{\delta h} \quad (4.84)$$

Substituting these expressions for dynamic pressure and dynamic pressure rate into Equation 4.82, yields,

$$\ddot{\delta h} + K K_{\dot{q}} \dot{\delta h} + K K_{\bar{q}} \delta h = \frac{C_L S}{m} K_{\bar{q}} \left[ \frac{1}{2} v_{rel}^2 \rho(h^*) - \bar{q}_{tgt} \right] \quad (4.85)$$

where,

$$K = -\frac{1}{2} \left( \frac{C_L S}{m} \right) v_{rel}^2 \left. \frac{\partial \rho}{\partial h} \right|_{h^*} \quad (4.86)$$

An equation for the derivative of the density with respect to altitude can be formulated if an exponential atmospheric density is assumed of the form,

$$\rho = \rho_{sl} e^{-\left(\frac{h}{h_s}\right)} \quad (4.87)$$

The partial derivative is then,

$$\frac{\partial \rho}{\partial h} = -\frac{\rho_{sl}}{h_s} e^{-\left(\frac{h}{h_s}\right)} \quad (4.88)$$

so that the term K is now expressed as,

$$K = \frac{C_L S}{2m h_s} \rho_{sl} v_{rel}^2 e^{-\left(\frac{h}{h_s}\right)} \quad (4.89)$$

Since the expression for density is linearized in the equations of motion, the gain K must be reevaluated each time the controller is executed. It is computationally more efficient to group the constant terms in K together into  $K_{const}$  and to compute this only once.  $K_{const}$  is then multiplied by the variable portion of K,  $K_{vary}$ , which is evaluated each guidance cycle. The new values which form the K term are,

$$K = K_{const} K_{vary} \quad (4.90)$$

where,

$$K_{const} = \frac{C_L S \rho_{sl}}{2 m h_s} \quad (4.91)$$

and,

$$K_{vary} = v_{rel}^2 e^{-\left(\frac{h}{h_s}\right)} \quad (4.92)$$

Equation 4.85 is a second-order constant coefficient differential equation in altitude of the form,

$$\ddot{\delta h} + 2\zeta\omega_n\dot{\delta h} + \omega_n^2\delta h = f(t) \quad (4.93)$$

The response of this system can be varied by changing the damping ratio and the natural frequency. In order to determine the parameters that give the desired transient response, the homogeneous second-order differential equation in altitude is considered,

$$\ddot{\delta h} + K K_{\dot{q}}\dot{\delta h} + K K_{\bar{q}}\delta h = 0 \quad (4.94)$$

The natural frequency and damping ratio of this homogeneous system are,

$$\omega_n = \sqrt{K K_{\bar{q}}} \quad (4.95)$$

$$\zeta = \frac{K K_{\dot{q}}}{2\omega_n} \quad (4.96)$$

and since it is the gains that are desired as a function of the input damping ratio and natural frequency, the purpose is better served by rearranging as,

$$K_{\bar{q}} = \frac{\omega_n^2}{K} \quad (4.97)$$

$$K_{\dot{q}} = \frac{2\zeta\omega_n}{K} \quad (4.98)$$

A combination of damping ratio and natural frequency is empirically chosen to give satisfactory dynamic pressure damping.

## Chapter 5

# Guidance Performance

Different aspects of guidance performance are presented in this chapter. Section 5.1 analyzes the ability of the guidance to steer the vehicle to all of the targets that the vehicle is capable of reaching under nominal open-loop conditions. The next section demonstrates the ability of the guidance to reach selected targets within the vehicle footprint in the presence of dispersions. Speed brake performance is discussed in Section 5.3, and the performance of the dynamic pressure controller is demonstrated in Section 5.4. The last section examines the behavior of the lift-to-drag ratio and density filters used in the guidance predictions.

All test entry trajectories in this chapter, except for the cases which are dispersed in initial flight path angle, used the same set of state initial conditions summarized in Table 3.1. Vehicle M, described in Section 3.4, was flown for the tests at a  $33^\circ$  angle of attack which provided an L/D of 0.85 and a ballistic coefficient of 283 kg/sq m.

**Table 5.1. Guidance I-Loads — Baseline Case (Nominal Target)**

$g_{begin}$	= 0.07 g's	hs	= 18288 m
$v_{ei}$	= 3550 m/s	$v_f$	= 530 m/s
$\phi_{min}$	= 15°	$\delta\phi_{des}$	= 3°
$R_{slw}$	= 15 sec	$R_{fst}$	= 5 sec
$h_{cfst}$	= 30000 m	$h_{cfrz}$	= 10000 m
$\Delta\phi_{lim}$	= 15°	$V_{\Delta\phi_{lim}}$	= 2500 m/s
$\Delta t_{big}$	= 30 sec	$\Delta t_{sml}$	= 2 sec
$h_{\Delta t_{sml}}$	= 10000 m	$h_{pquit}$	= 5000 m
$K_\rho$	= 0.0488	$K_{\frac{L}{D}}$	= 0.0488
$\zeta$	= 1.0	$\omega_n$	= 0.05 rad/s
$K_{\bar{q}_f}$	= 0.97	$V_{dmp}$	= 0 m/s
$\bar{q}_{tgt}$	= 1000 N/sq m	$\bar{q}_{lim}$	= 1000 N/sq m
$\psi_{errmax}$	= 6°	$\psi_{errmin}$	= 3°
$V_{\psi_{errmax}}$	= 3300 m/s	$V_{\psi_{errmin}}$	= 2200 m/s

Predictor Density Model = COSPAR Northern Hemisphere Mean

## 5.1 Nominal Performance

The baseline performance of the guidance was determined in a nominal atmosphere without the dynamic pressure controller. The guidance constants, or I-loads, contained in Table 5.1 were used for these cases.

As seen in Figure 5.1, the guidance demonstrated itself capable of reaching almost all regions along the edge of the open-loop footprint that was generated using the bank profile described in Chapter 3. The short downrange part of the footprint resulted

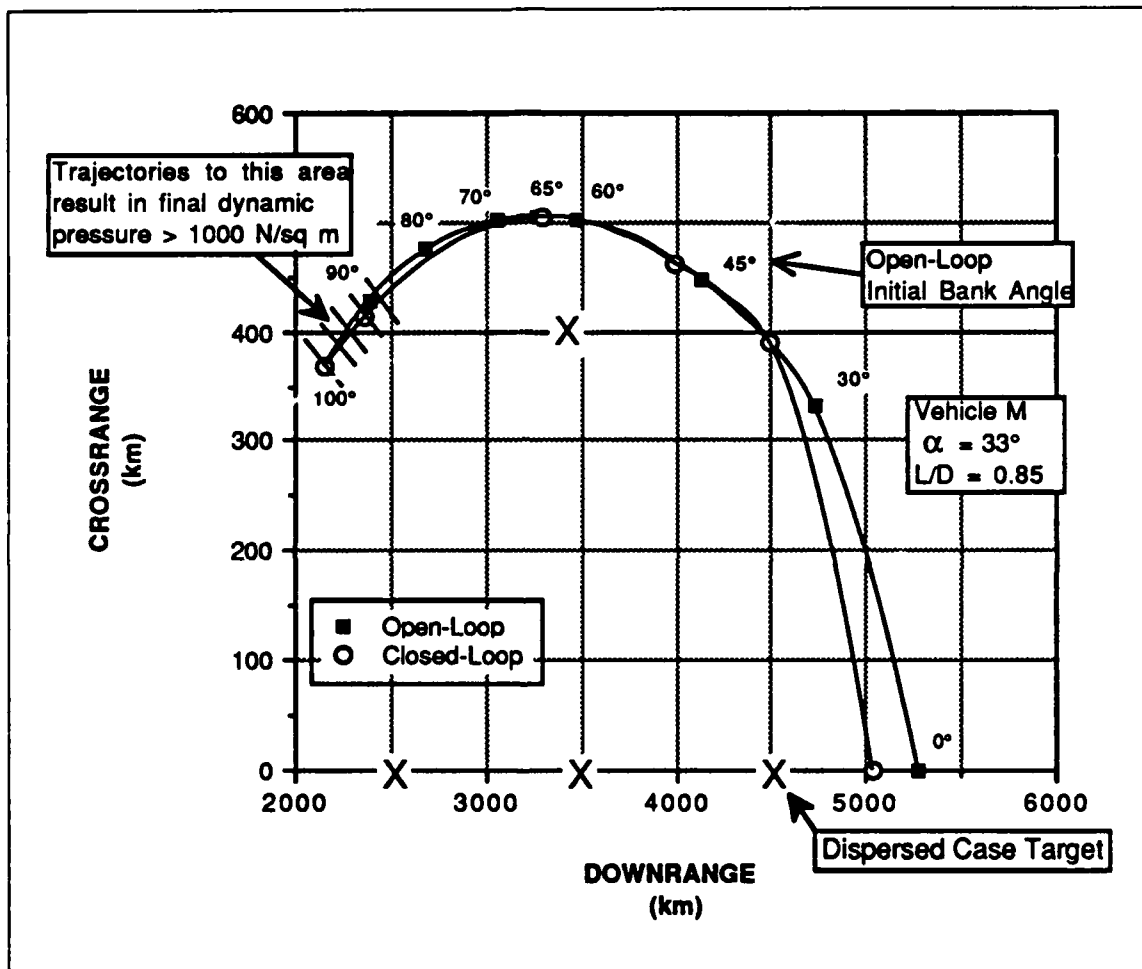


Figure 5.1. Guidance Coverage of Open-Loop Footprint

in final dynamic pressures higher than allowable, even though the vehicle was able to physically reach the target. This is a result of the trajectory simply being too short for the vehicle to dissipate the necessary energy. The long downrange portion of the footprint was physically unreachable because of the introduction in the guidance of  $\phi_{min}$ . The minimum bank angle limits the amount of vertical lift in order to ensure some component of lateral lift at all times. The trade-off is beneficial because the maintenance of crossrange authority is important while the extra downrange capability lost is negligible.

The guidance resulted in the loss of no crossrange capability. As can be seen in Figure 5.1, the guidance was able to achieve the same maximum crossrange as was possible flying open-loop. Only small portions of the open-loop footprint are lost to the guidance, and these parts are at the edge of the downrange capability which is not a major concern.

## 5.2 Dispersed Performance

To demonstrate the capability of the guidance to successfully reach different portions of the closed-loop footprint despite dispersions, four points were chosen in the footprint. The four locations are characterized as nominal, short downrange, long downrange, and maximum crossrange. The location of these targets within the closed-loop footprint is indicated in Figure 5.1. Runs were made without the use of the dynamic pressure controller to each of these points using the range of dispersions summarized in Table 5.2. These dispersions consist of those discussed in Chapter 2 and an initial

Table 5.2. Summary of Dispersions

Aerodynamic Coefficients	$C_L^\pm$	$\pm 10\% C_D$
	$C_D^\pm$	$\pm 10\% C_L$
Winds	W000	50 m/s at 0° (Northerly Wind)
	W090	50 m/s at 90° (Easterly Wind)
	W180	50 m/s at 180° (Southerly Wind)
	W270	50 m/s at 270° (Westerly Wind)
Density	$\rho^{cl}$	Revised COSPAR Cool-Low Model
	$\rho^{wh}$	Revised COSPAR Warm-High Model
	$\rho^{v1}$	Viking 1 Entry Trajectory Data
	$\rho^{v2}$	Viking 2 Entry Trajectory Data
	$\rho^-$	Constant Density Bias—50% Thin
	$\rho^+$	Constant Density Bias—100% Thick
	$\rho^{es}$	Early Density Shear—25% Thin
	$\rho^{ls}$	Late Density Shear—10% Thin
Flight Path Angle	$\gamma^\pm$	$\pm 0.5^\circ \gamma_{ei}$

flight path angle dispersion. A known flight path angle error is the only component of the state error at entry interface which can cause significant dispersions, and variations of  $\pm 0.5^\circ$  are considered.

Using the same I-loads as in the previous section, the guidance performed well with the exception of some extreme cases, and even then, the results were generally satisfactory and not unexpected. The terminal conditions for the nominal and dis-

persed trajectories to each of the four targets are contained in Tables 5.3 through 5.6 on pages 131-134.

For the nominal target, the guidance performed very well. None of the continuous constraints were violated by any of the dispersed trajectories. The maximum g-load and heating rate experienced in any of these trajectories are 0.55 g's and 13.36 W/sq cm/s, while the maximum integrated heat load was 6643.6 W/sq cm. As seen in Table 5.3, which contains the nominal and dispersed results for the nominal target, the only cases which had difficulties with the terminal conditions were the constant density bias trajectories. The 50% thin atmosphere did not provide enough drag to slow the vehicle and caused the final dynamic pressure (1012 N/sq m) to be too high. The 100% thick atmosphere bled too much energy from the trajectory early and caused the vehicle to reach the target with a flight path angle (-24.7°) that was too steep. Both of these values barely exceed their respective limits.

For the short target, the guidance did not perform as well, but the overall performance was still very satisfactory. For this target, the nominal and dispersed terminal conditions are contained in Table 5.4. There were no cases for which the g-load or heating rate exceeded their limits, and the maximum values for these parameters were 2.28 g's and 17.56 W/sq cm/s. The maximum total heat load was 4841.7 W/sq cm. The final dynamic pressure limit was exceeded in two cases. The shallow initial flight path angle and the 50% thin atmosphere, respectively, caused the final dynamic pressure to be 1202.0 and 1152.2 N/sq m. This is not unexpected because of the short length of the trajectory. The shallow initial flight path angle does not allow the vehi-

cle to experience enough drag early in the trajectory, and the thin atmosphere does not provide enough drag throughout the trajectory to sufficiently reduce the velocity.

For the same reasons as in the nominal target case, the terminal flight path angle limit is exceeded ( $-24.6^\circ$ ) in the 100% thick atmosphere. The southerly ( $0^\circ$ ) wind, which is a crosswind for most of the trajectory, caused small misses in both the crossrange (1.10 km) and the downrange (1.25 km). The crossrange miss can be directly attributed to the wind causing the vehicle to veer off its intended track late in the trajectory when the lateral component of lift is small. The downrange error is also caused by the crosswind. Although this may seem unnatural, the predictor-corrector controls downrange using predictions which are based on the navigation estimate of the relative velocity. The navigation estimate of relative velocity does not account for the wind, and this causes a small error in the prediction. The error in the prediction is not significant until late in the trajectory when the vehicle slows down. The slower velocity (a significantly shorter vector) and a crosswind (perpendicular vector which remains constant) can combine to cause a large error in the direction of the relative velocity.

The only other dispersion which caused a problem for the short target is the Cool-Low atmosphere. From Figure 2.2, it can be seen that this atmosphere is continually becoming thicker relative to the nominal atmosphere as the altitude decreases. Because of this, the downrange is controlled based on predictions which expect a thinner atmosphere than is actually encountered. The thicker atmosphere increases the available lift, and this is why the vehicle flew slightly (1.06 km) past the target.

Short targets generally pose a problem with the final dynamic pressure because of the reduced drag along the shorter trajectories. The small range errors at the short target can also be attributed, at least in part, to the short length of the trajectory. Everything happens much more quickly, and the guidance has less time to react to the dispersions. Late in the trajectory, there is not enough time with the limited control authority to completely correct the small errors.

With the exception of one case, the guidance was also very successful reaching the long target. The maximum g-load and heating rate for all of the dispersed cases to this target were 0.51 g's and 12.21 W/sq cm/s—well under the limits. In addition the maximum integrated heat load was 7846.0 W/sq cm. As seen in Table 5.5, the dispersion which caused a significant target miss is the steep initial flight path angle. The guidance commanded maximum lift-up immediately, yet the vehicle was still unable to reach the target. This is not a failure of the guidance, but a limitation of the vehicle lifting capabilities because the long target is not inside what would be the dispersed open-loop footprint. Although not demonstrated with the same vehicle, the significant reduction in ranging capability caused by a steep entry flight path angle can be seen in Figure 3.6.

For the long target, the northerly ( $180^\circ$ ) wind caused a small (1.15 km) downrange error which is again attributable to the error in the navigation relative velocity—an error largely in direction as opposed to magnitude. The 100% thick atmosphere also caused the now-expected error in terminal flight path angle ( $-24.3^\circ$ ).

For the maximum crossrange target, the guidance showed no major irregularities.

The nominal and dispersed results are shown in Table 5.6. Once again, the maximum g-loads and heating rates, 0.55 g's and 13.49 W/sq cm/s, were well within acceptable values, and the maximum heat load was only 6550.9 W/sq cm. The 50% thin atmosphere caused a small violation of the final dynamic pressure constraint (1006 N/sq m). And, just as it did for the other targets, the 100% thick atmosphere caused an error in the final flight path angle (-24.8°).

In general, the guidance reacted properly to all of the dispersions and performed very well. Most of the constraint violations are very small. Since the constraints are not very definite at this point in the mission design, these small errors are not a cause for concern. The only large miss of the target was shown to be a vehicle limitation and not a guidance problem. The guidance demonstrated the ability to achieve precision entry using bank angle control only.

In order to provide some insight into the behavior of the guidance, the bank history for all four nominal cases to each of the different targets is plotted against velocity in Figures 5.2 through 5.5 on pages 135-138. The effect of downrange on the bank profile can easily be seen. The minimum downrange target requires less vertical lift, so the bank profile in Figure 5.3 is much steeper than the profile required to reach the nominal target in Figure 5.2. Along the same lines, the profile necessary to reach the maximum downrange target in Figure 5.4 is much shallower than the nominal profile because more vertical lift is required to reach the long target. As can be seen in Figure 5.5, the maximum crossrange case flew a bank profile with approximately the same slope as the nominal case. This is because the maximum crossrange target

is nearly as far downrange as the nominal target. The difference in the two cases is in the sign of the bank angle.

The azimuth error as a function of velocity is presented for the undispersed trajectories to each of the four targets in Figures 5.6 through 5.9 on pages 139-142. In each of the cases, the azimuth error becomes very large as the vehicle approaches or passes the target. Although the error gets very large, the crossrange controller still behaves properly and only commands a reversal when the current bank angle is causing the azimuth error to increase.

Because nearly full lift-up is required to reach the maximum downrange target, the lateral component of lift is relatively small for this trajectory. Hence, as can be seen by comparing Figures 5.6 and 5.8, the azimuth error limit is exceeded fewer times in this case than in the nominal target case which has a larger lateral lift component. The azimuth error for the maximum crossrange target trajectory is initially relatively big, as shown in Figure 5.9. Once this error is reduced to within the limits, the value deadbands between the limits just as in the nominal case.

Plots of selected parameters from the nominal target, no dispersion case are contained in Figures 5.10 through 5.16 on pages 143-149. The selected parameters—altitude, velocity, dynamic pressure, heating rate, total crossrange, total downrange, and flight path angle—are plotted against time.

**Table 5.3. Nominal Target: Results of Dispersed Cases**

Dispersion	$DR_e$ (km)	$CR_e$ (km)	$\bar{q}_f$ (N/sq m)	$\gamma_f$ (deg)
Nominal	0.09	-0.48	897.4	-15.3
$C_D^+$	0.01	0.45	860.8	-16.5
$C_D^-$	0.14	0.46	937.9	-14.1
$C_L^+$	0.09	0.33	839.4	-15.3
$C_L^-$	-0.15	0.04	986.6	-15.4
W000	0.07	-0.38	916.8	-15.9
W090	0.56	-0.47	897.7	-15.1
W180	0.10	-0.42	884.3	-14.9
W270	-0.03	-0.43	901.5	-15.5
$\rho^{cl}$	-0.89	-0.54	914.2	-14.1
$\rho^{wh}$	0.55	-0.44	872.4	-18.1
$\rho^{v1}$	-0.51	-0.50	870.1	-15.6
$\rho^{v2}$	-0.38	-0.51	876.8	-15.4
$\rho^-$	0.32	0.88	1012.4	-9.1
$\rho^+$	-0.08	0.23	869.5	-24.7
$\rho^{es}$	0.11	-0.49	895.7	-15.4
$\rho^{ls}$	0.03	0.00	910.7	-13.8
$\gamma_{ei}^+$	0.14	-0.05	924.3	-15.5
$\gamma_{ei}^-$	0.25	0.55	889.1	-15.9

**Table 5.4. Minimum Downrange Target: Results of Dispersed Cases**

Dispersion	$DR_e$ (km)	$CR_e$ (km)	$\bar{q}_f$ (N/sq m)	$\gamma_f$ (deg)
Nominal	-0.25	-0.49	841.7	-15.6
$C_D^+$	0.18	-0.46	837.5	-16.9
$C_D^-$	-0.13	-0.53	862.7	-15.1
$C_L^+$	0.27	0.45	792.4	-16.6
$C_L^-$	0.07	-0.54	934.8	-15.3
W000	-1.25	1.10	840.4	-16.2
W090	0.71	-0.43	840.9	-14.9
W180	-0.79	0.27	866.8	-15.9
W270	-0.35	-0.40	850.0	-16.1
$\rho^{cl}$	-1.06	-0.54	851.2	-13.8
$\rho^{wh}$	0.47	0.15	870.6	-19.0
$\rho^{v1}$	-0.19	0.44	822.3	-15.9
$\rho^{v2}$	-0.27	-0.52	820.2	-15.9
$\rho^-$	-0.58	0.31	1202.0	-7.7
$\rho^+$	0.10	-0.28	886.3	-24.6
$\rho^{cs}$	0.41	-0.48	841.5	-15.5
$\rho^{ls}$	0.00	0.00	850.4	-13.8
$\gamma_{ei}^+$	0.32	-0.42	1152.2	-13.9
$\gamma_{ei}^-$	0.18	-0.27	922.7	-16.5

Table 5.5. Maximum Downrange Target: Results of Dispersed Cases

Dispersion	$DR_e$ (km)	$CR_e$ (km)	$\bar{q}_f$ (N/sq m)	$\gamma_f$ (deg)
Nominal	0.25	-0.55	919.9	-15.6
$C_D^+$	0.24	-0.16	876.3	-17.0
$C_D^-$	-0.17	0.07	963.2	-14.2
$C_L^+$	0.03	0.06	865.0	-15.3
$C_L^-$	0.70	0.64	976.3	-16.1
W000	0.90	-0.43	955.9	-15.5
W090	0.55	-0.54	914.5	-15.8
W180	1.15	-0.17	912.5	-14.9
W270	-0.07	-0.48	922.1	-15.4
$\rho^{cl}$	-0.75	-0.58	937.2	-14.5
$\rho^{wh}$	0.57	-0.46	893.4	-18.1
$\rho^{v1}$	-0.25	-0.55	894.7	-15.7
$\rho^{v2}$	-0.43	-0.51	897.3	-15.7
$\rho^-$	-0.16	0.41	945.6	-9.7
$\rho^+$	0.03	0.15	864.6	-24.3
$\rho^{cs}$	-0.14	-0.53	922.0	-15.5
$\rho^{ls}$	0.22	0.19	928.2	-14.1
$\gamma_{ei}^+$	-0.06	0.10	904.9	-15.8
$\gamma_{ei}^-$	85.76	4.64	916.9	-15.3

Table 5.6. Maximum Crossrange Target: Results of Dispersed Cases

Dispersion	$DR_e$ (km)	$CR_e$ (km)	$\bar{q}_f$ (N/sq m)	$\gamma_f$ (deg)
Nominal	0.05	0.28	903.6	-15.3
$C_D^+$	-0.13	0.41	861.7	-16.6
$C_D^-$	0.24	0.47	944.3	-14.0
$C_L^+$	0.10	0.39	842.8	-15.2
$C_L^-$	0.19	0.36	970.1	-15.3
W000	-0.97	1.02	859.3	-15.6
W090	0.90	0.50	905.1	-15.1
W180	0.11	-0.18	929.7	-15.2
W270	0.09	0.10	902.5	-15.5
$\rho^{cl}$	-0.92	0.33	918.1	-14.1
$\rho^{wh}$	0.61	-0.12	873.8	-18.0
$\rho^{v1}$	-0.03	0.23	874.9	-15.5
$\rho^{v2}$	-0.34	0.08	880.5	-15.4
$\rho^-$	-0.32	-0.82	1006.0	-9.2
$\rho^+$	-0.06	-0.23	867.0	-24.8
$\rho^{es}$	0.24	0.34	900.6	-15.3
$\rho^{ls}$	0.41	0.59	916.3	-13.7
$\gamma_{ei}^+$	0.17	-0.33	921.6	-15.4
$\gamma_{ei}^-$	0.25	-0.08	886.4	-15.8

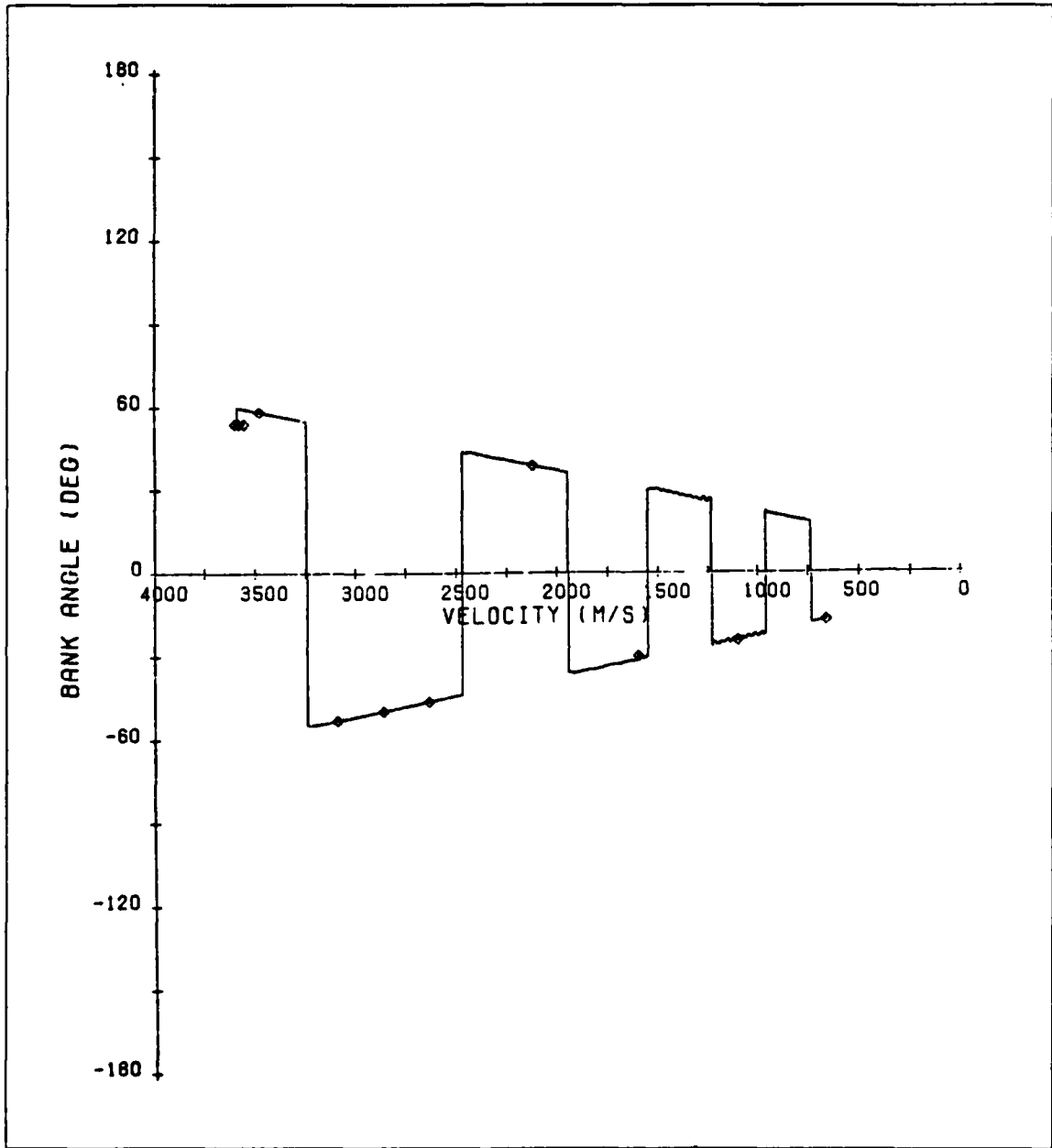


Figure 5.2. Closed-Loop Bank History for the Nominal Target — No Dispersion Case

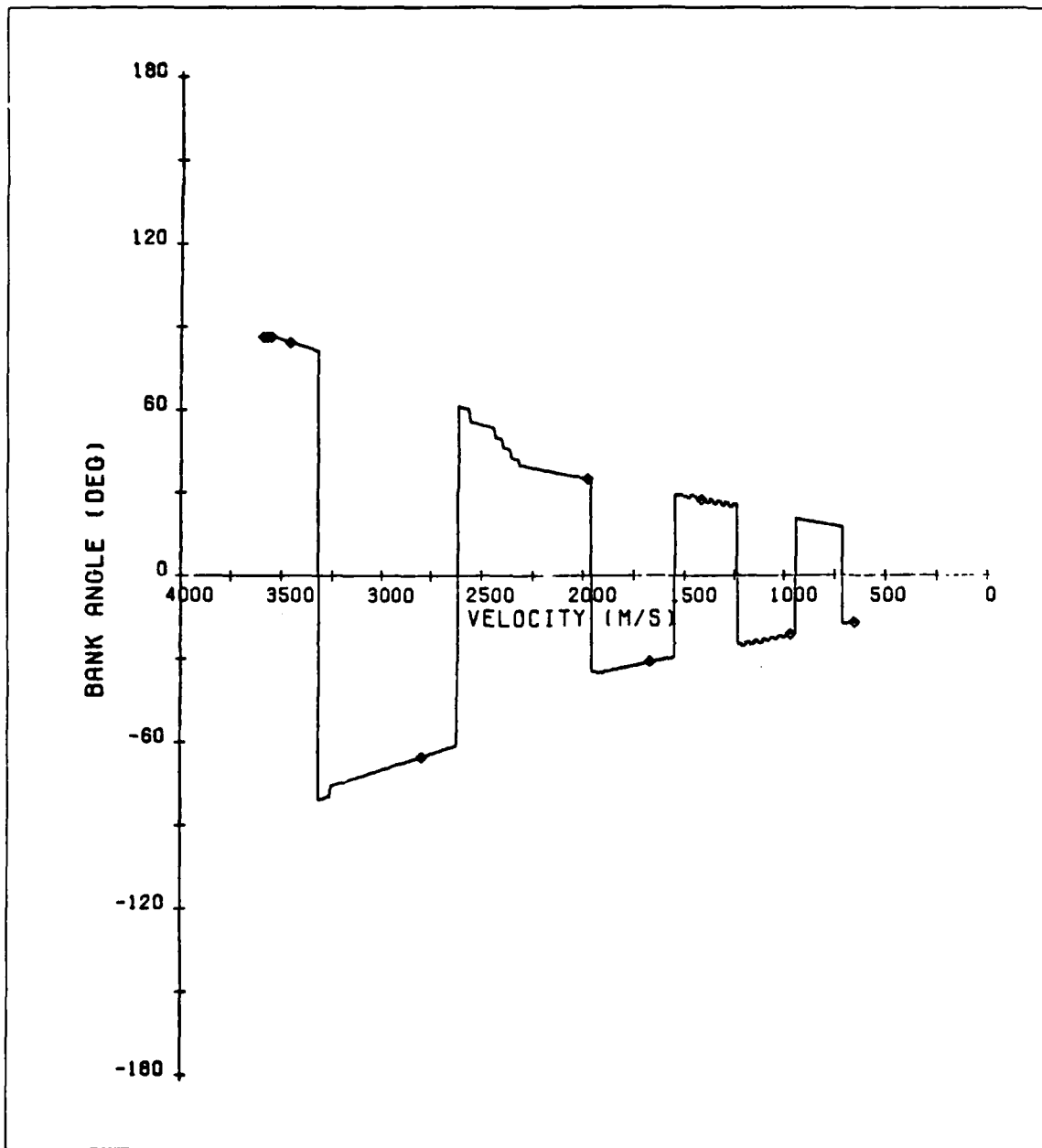


Figure 5.3. Closed-Loop Bank History for the Minimum Downrange Target — No Dispersion Case

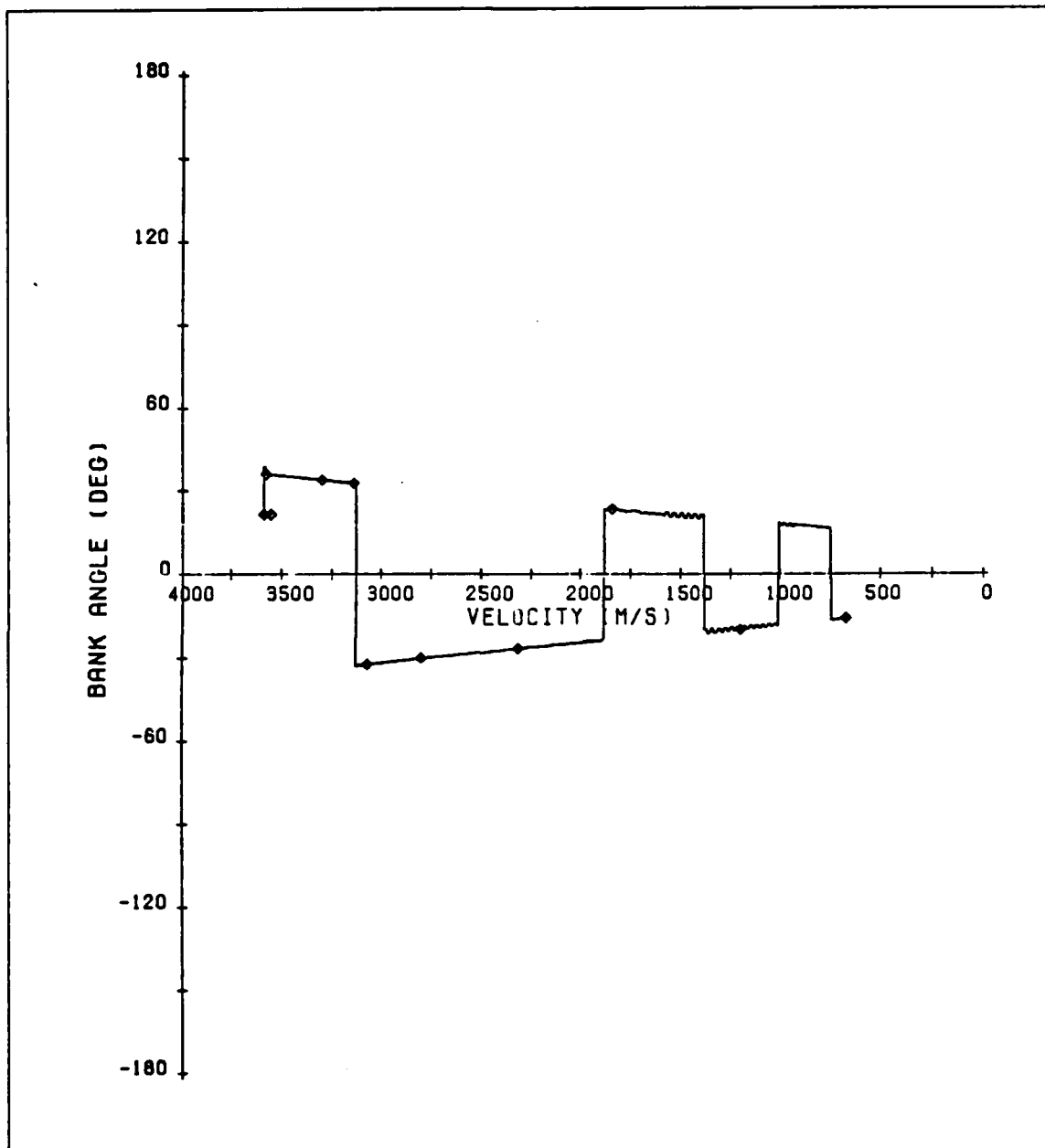


Figure 5.4. Closed-Loop Bank History for the Maximum Downrange Target — No Dispersion Case

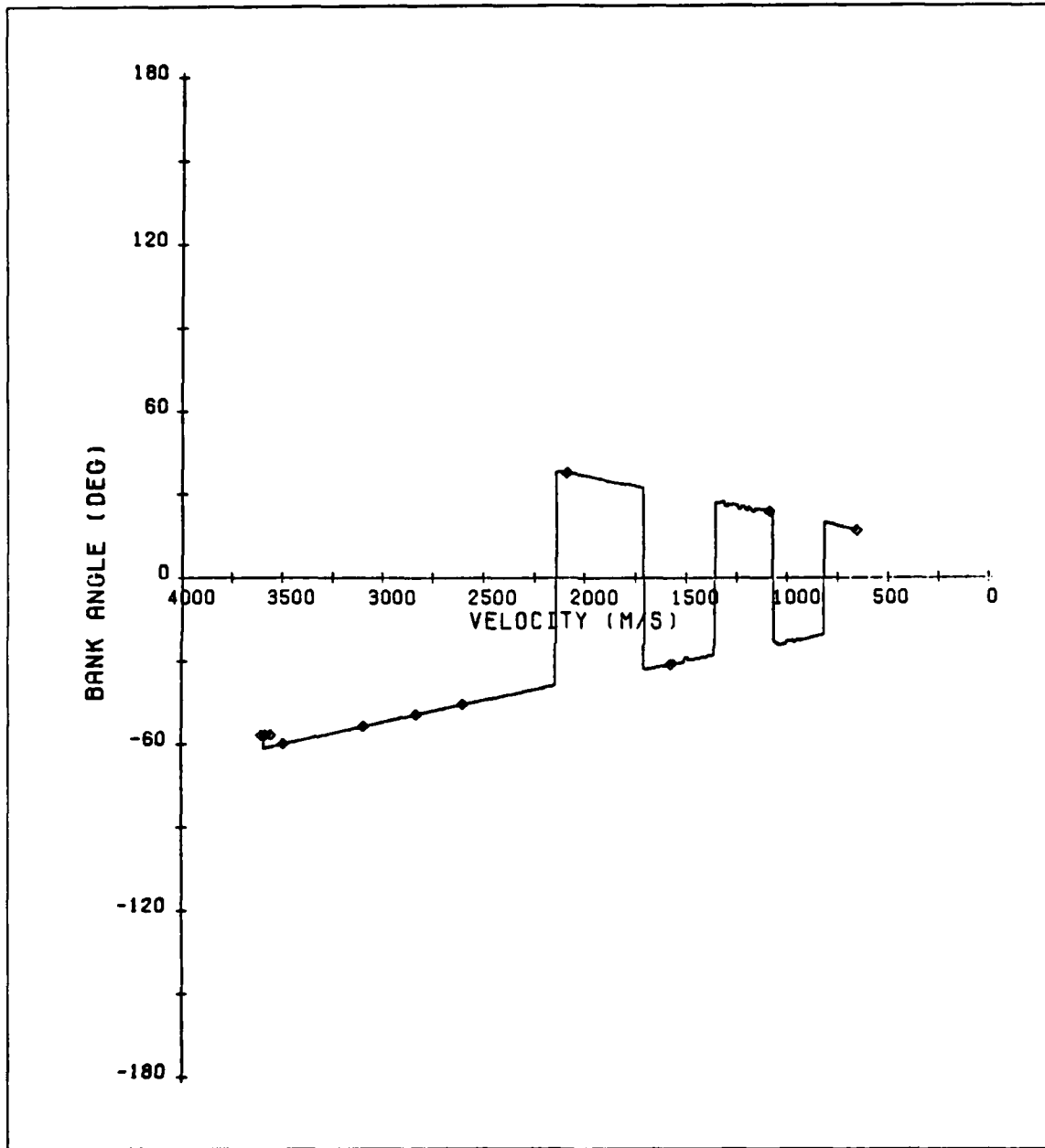


Figure 5.5. Closed-Loop Bank History for the Maximum Crossrange Target — No Dispersion Case

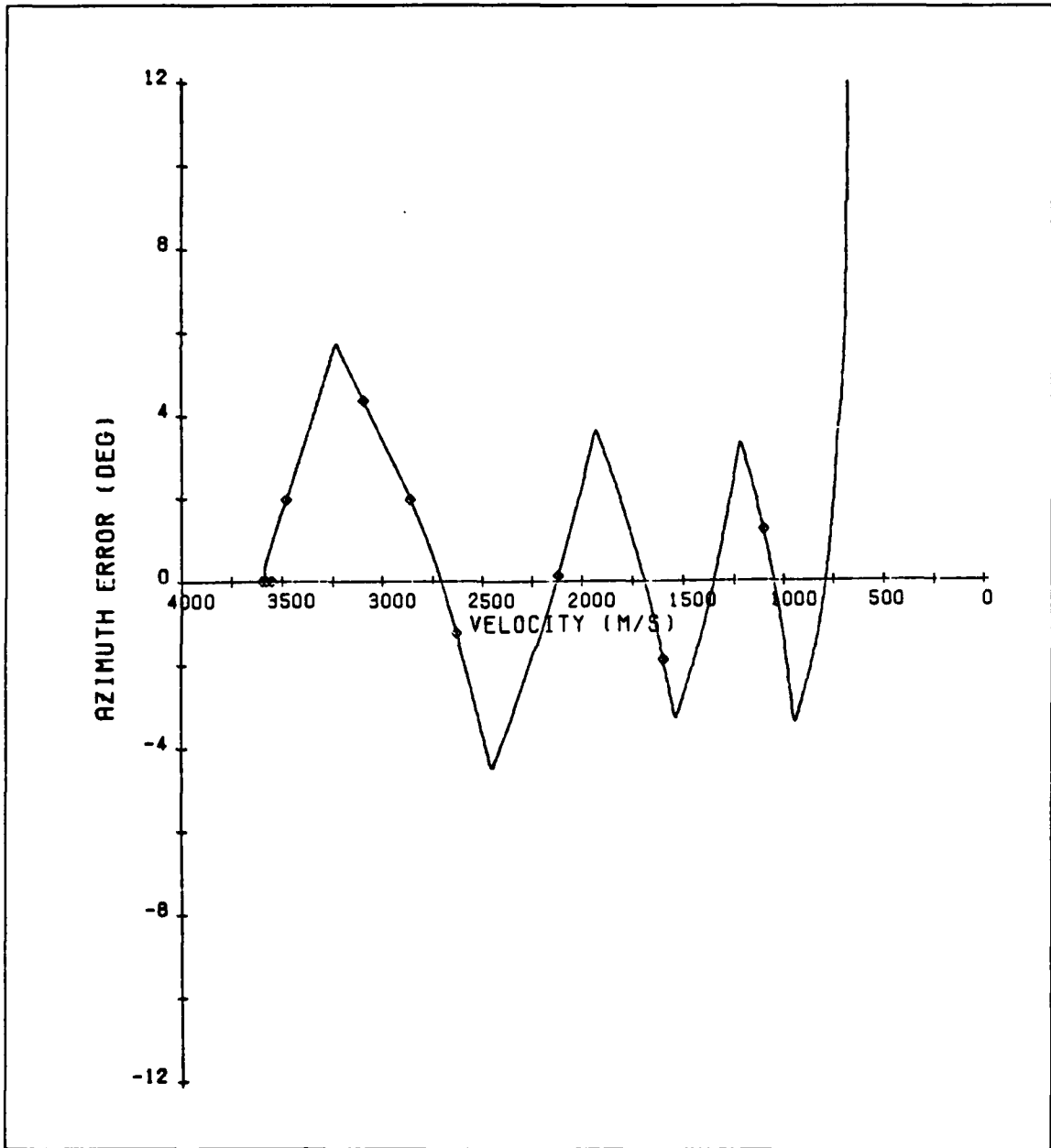


Figure 5.6. Closed-Loop Azimuth Error History for the Nominal Target — No Dispersion Case

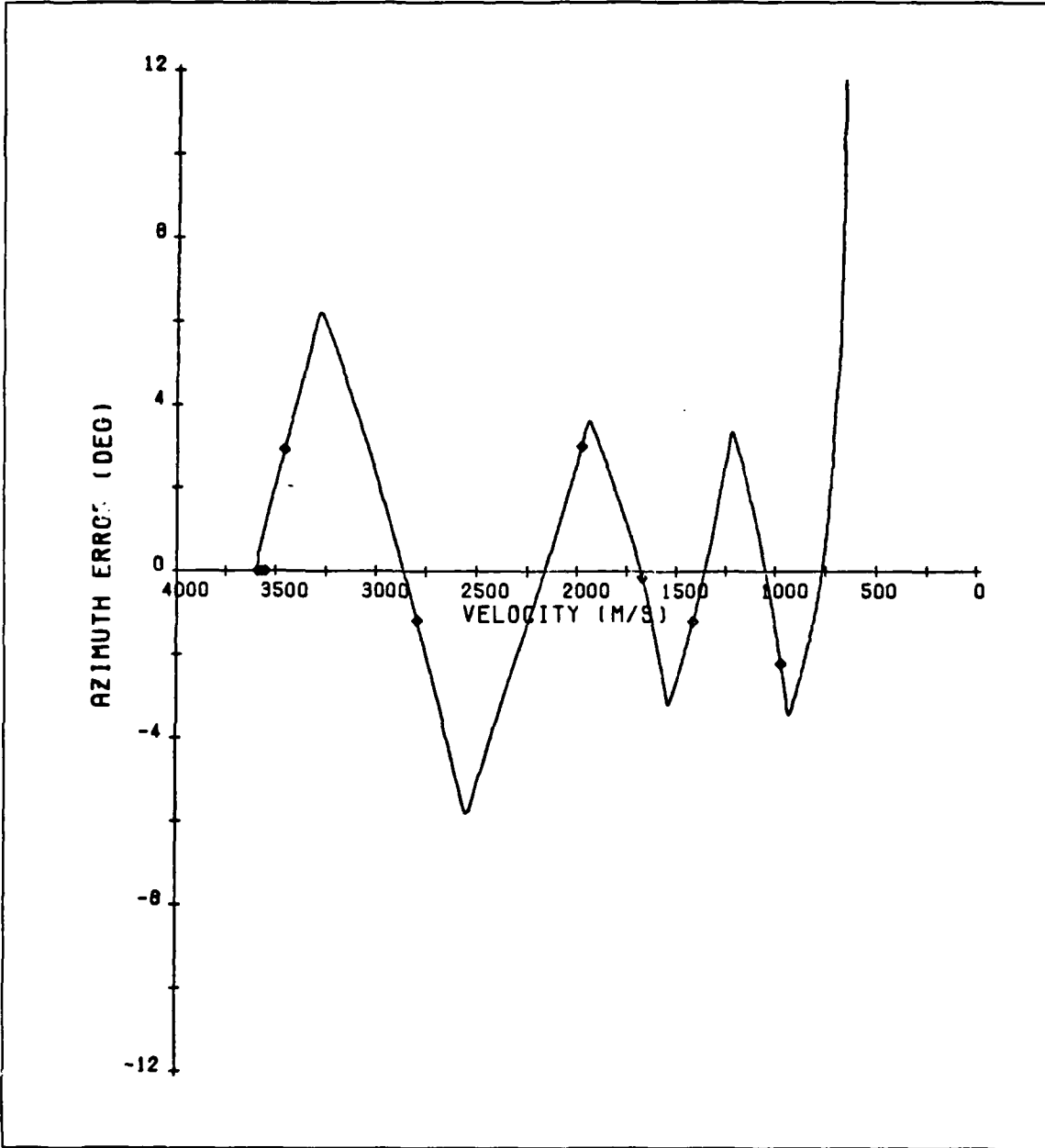


Figure 5.7. Closed-Loop Azimuth Error History for the Minimum Downrange Target  
 — No Dispersion Case

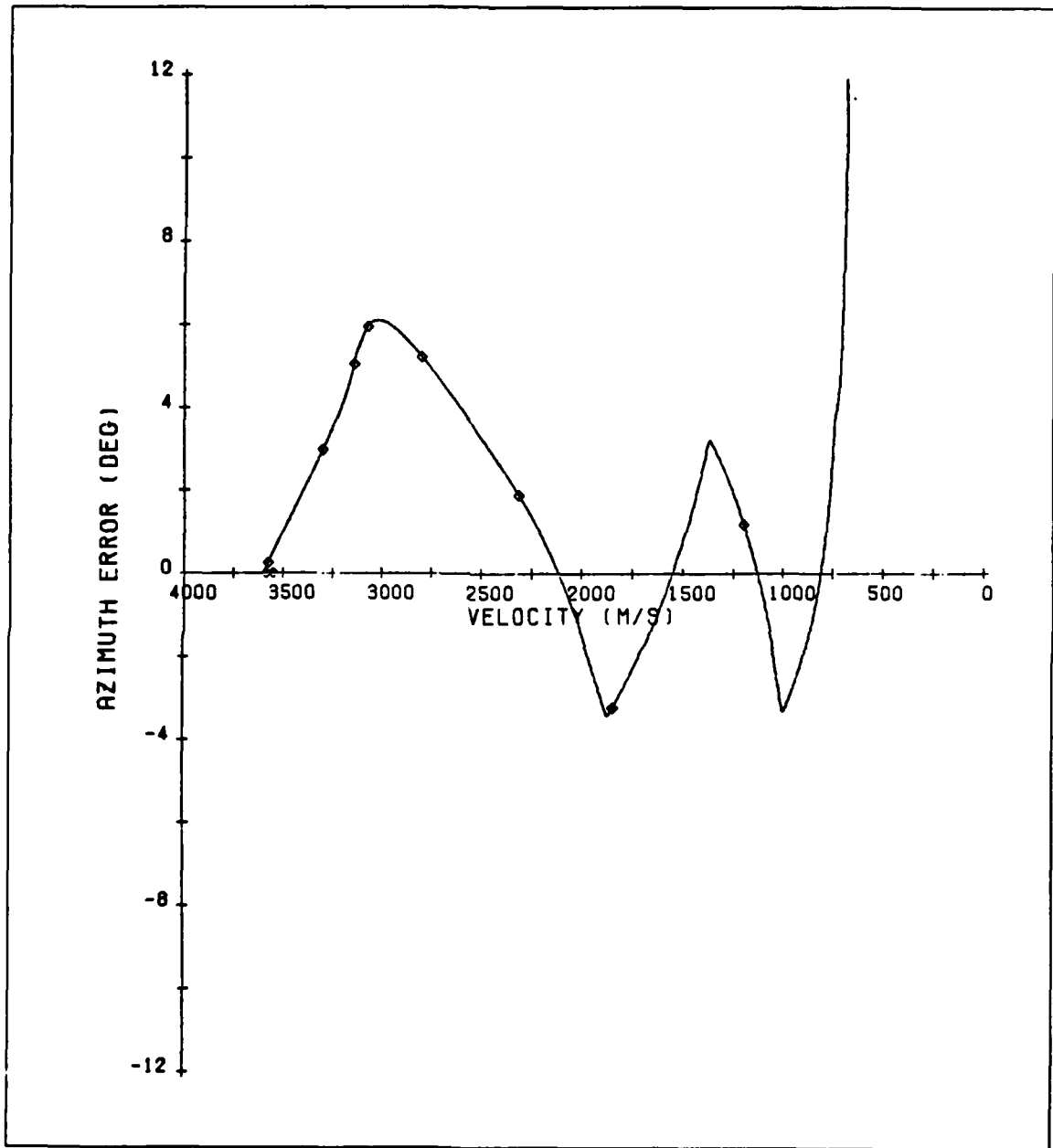


Figure 5.8. Closed-Loop Azimuth Error History for the Maximum Downrange Target — No Dispersion Case

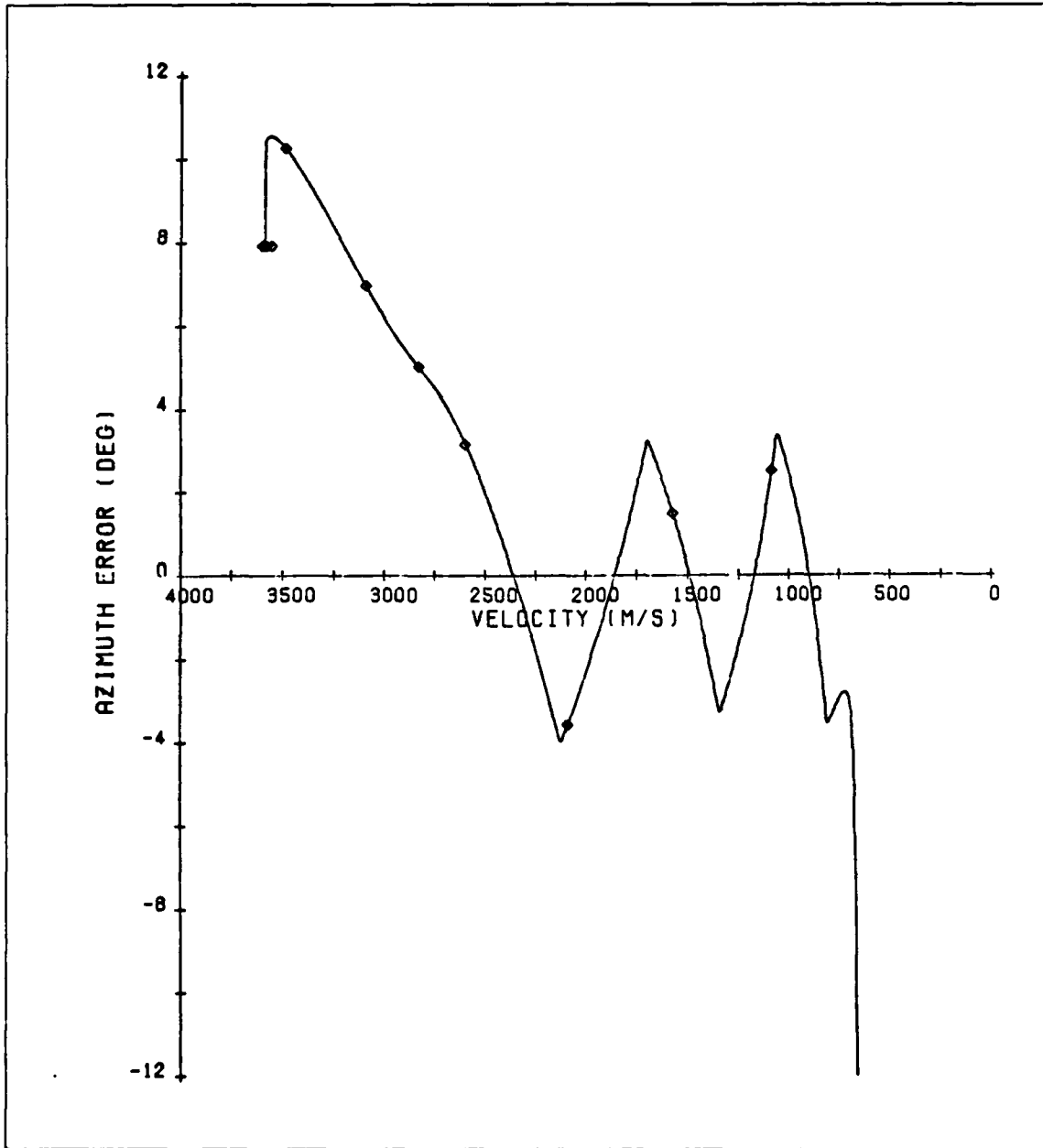
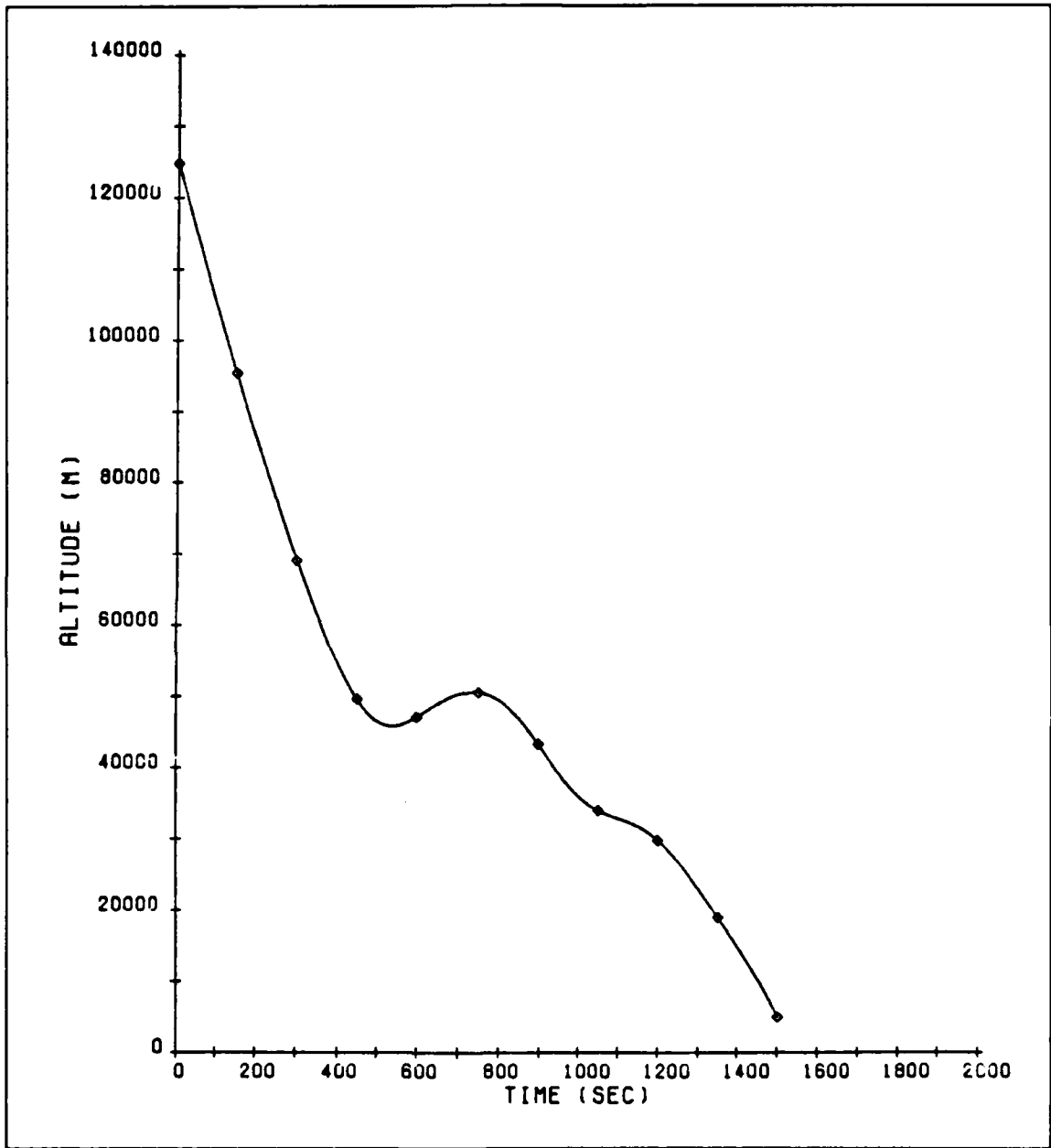


Figure 5.9. Closed-Loop Azimuth Error History for the Maximum Crossrange Target — No Dispersion Case



**Figure 5.10. Closed-Loop Altitude History for the Nominal Target — No Dispersion Case**

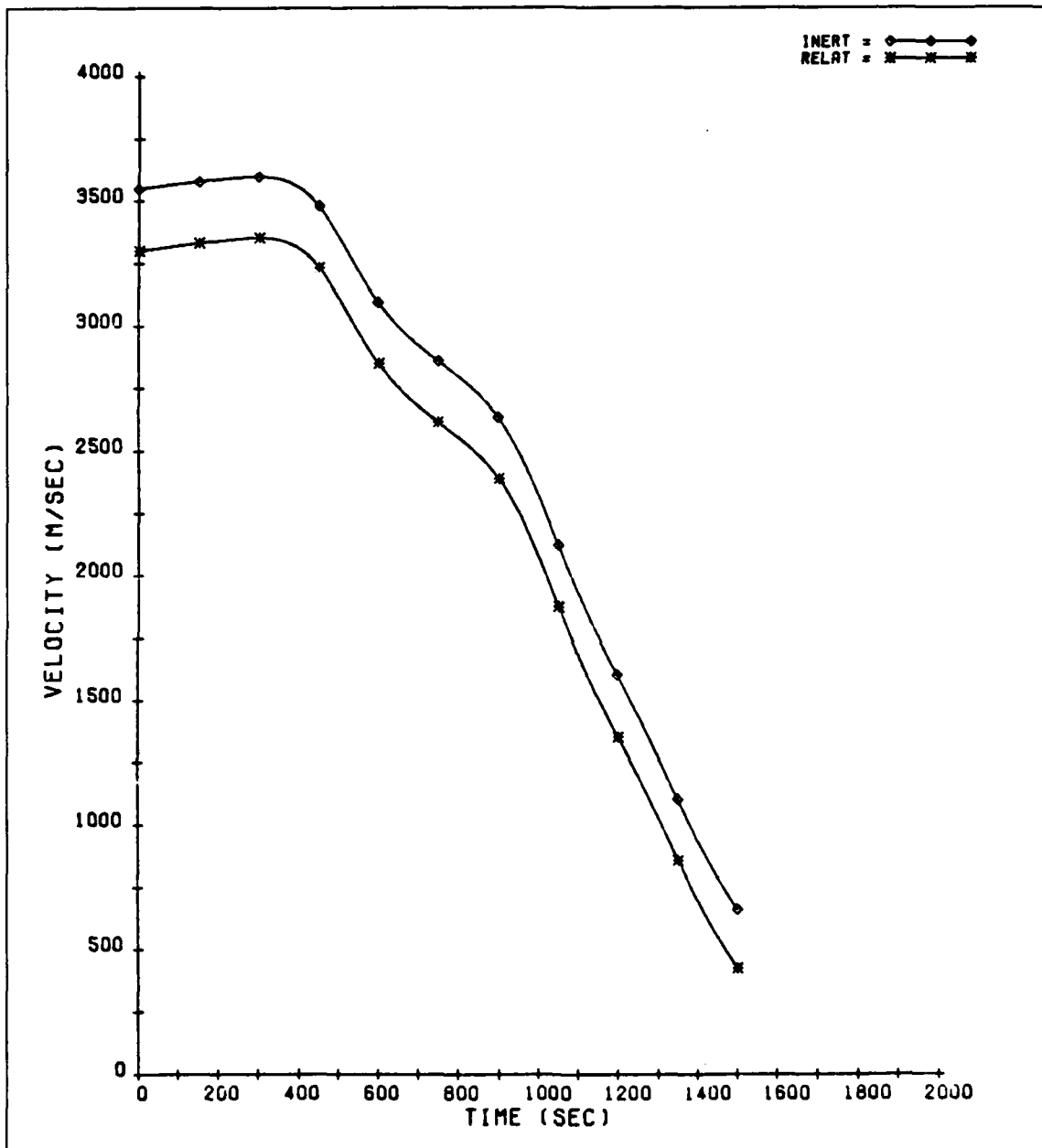


Figure 5.11. Closed-Loop Velocity History for the Nominal Target — No Dispersion Case

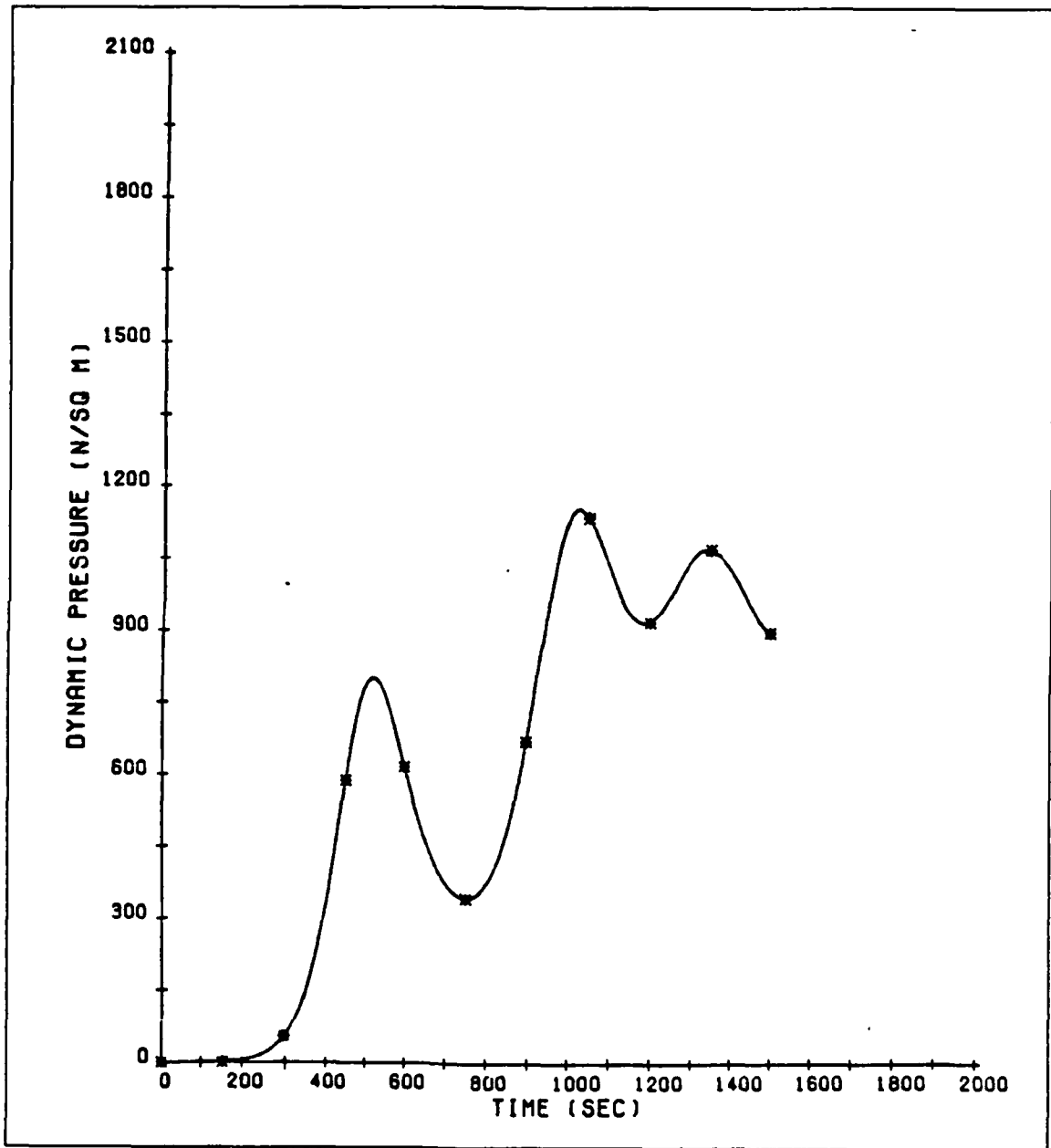


Figure 5.12. Closed-Loop Dynamic Pressure History for the Nominal Target — No Dispersion Case

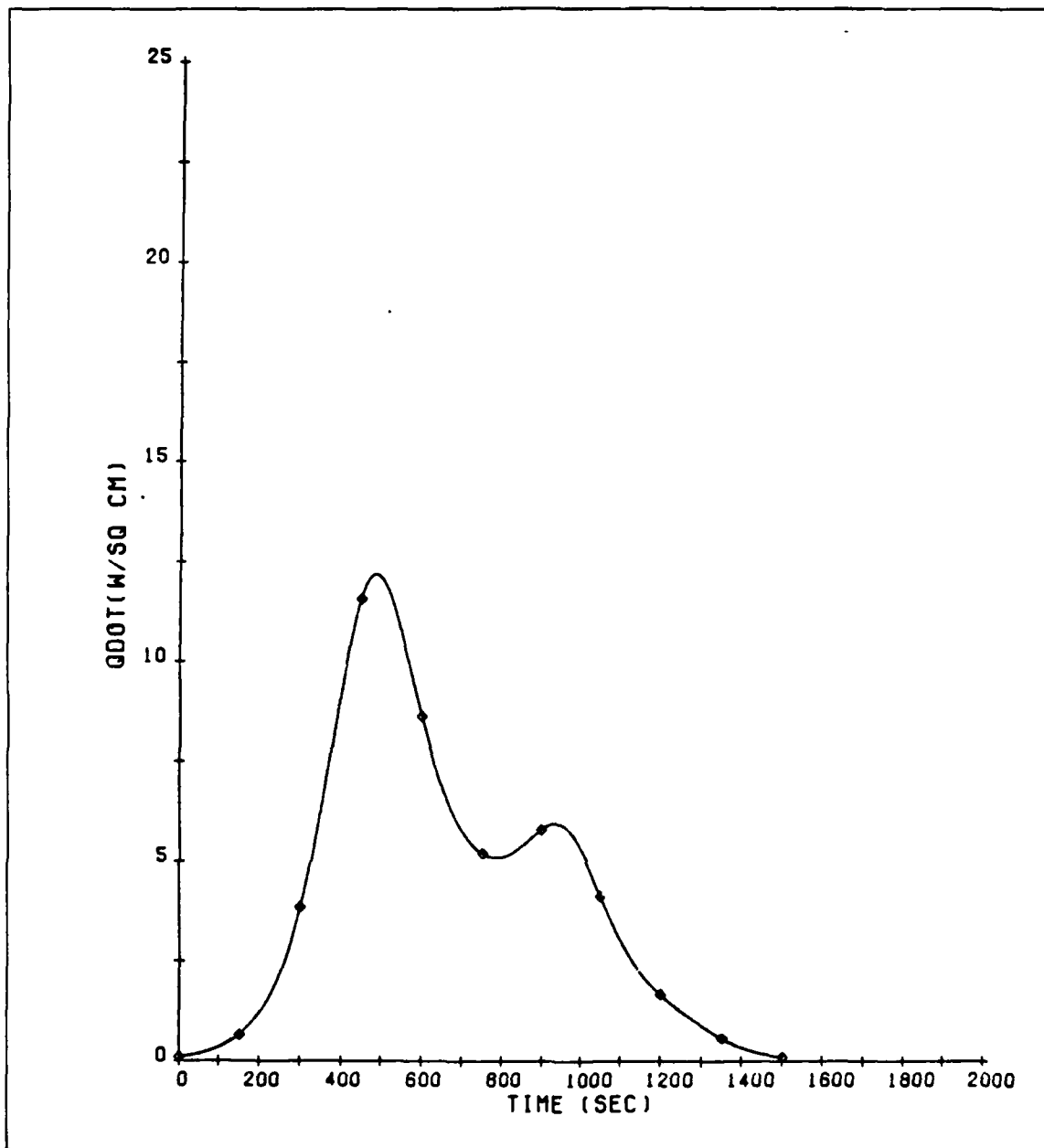


Figure 5.13. Closed-Loop Heating Rate History for the Nominal Target — No Dispersion Case

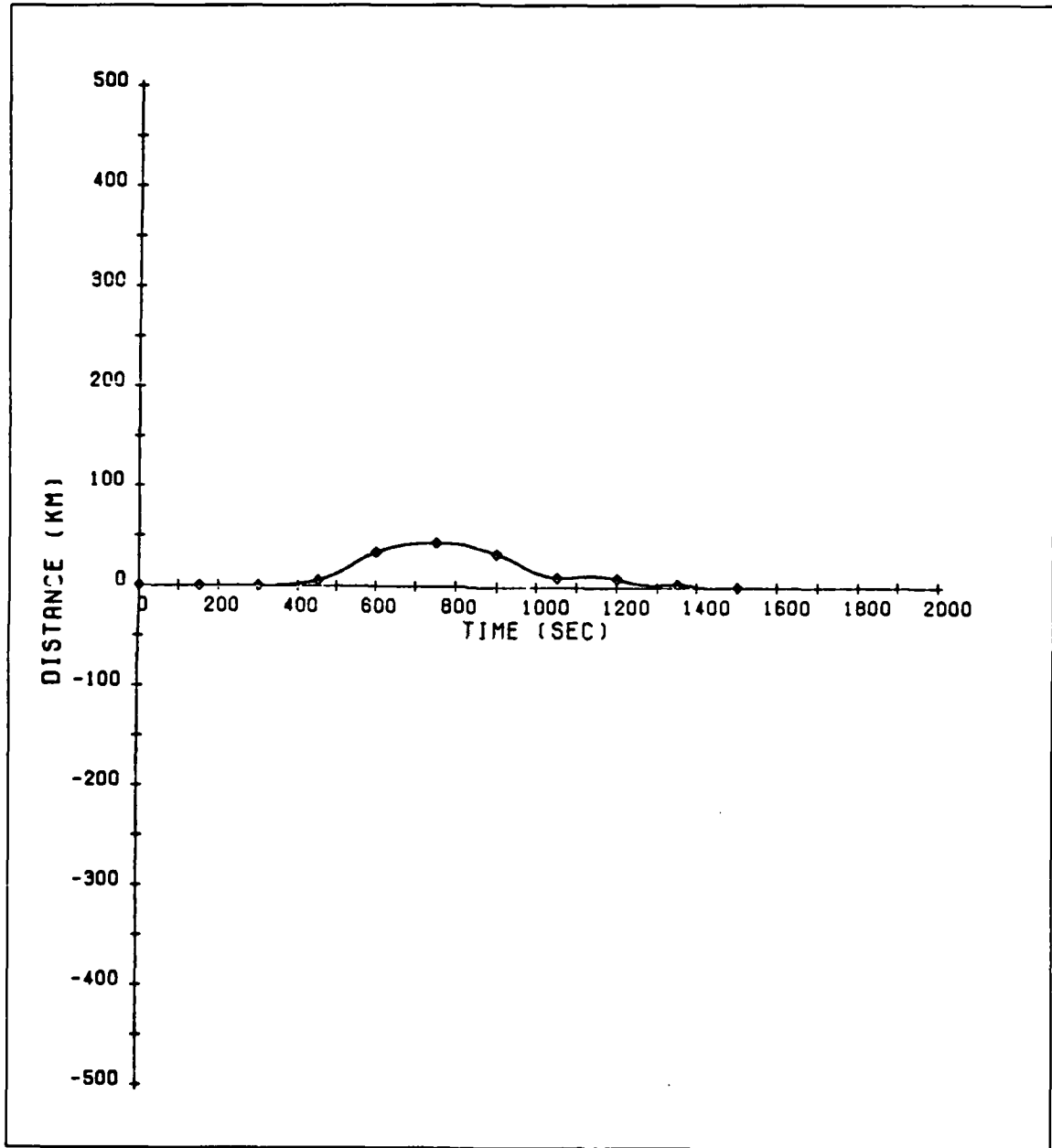


Figure 5.14. Closed-Loop Crossrange History for the Nominal Target — No Dispersion Case

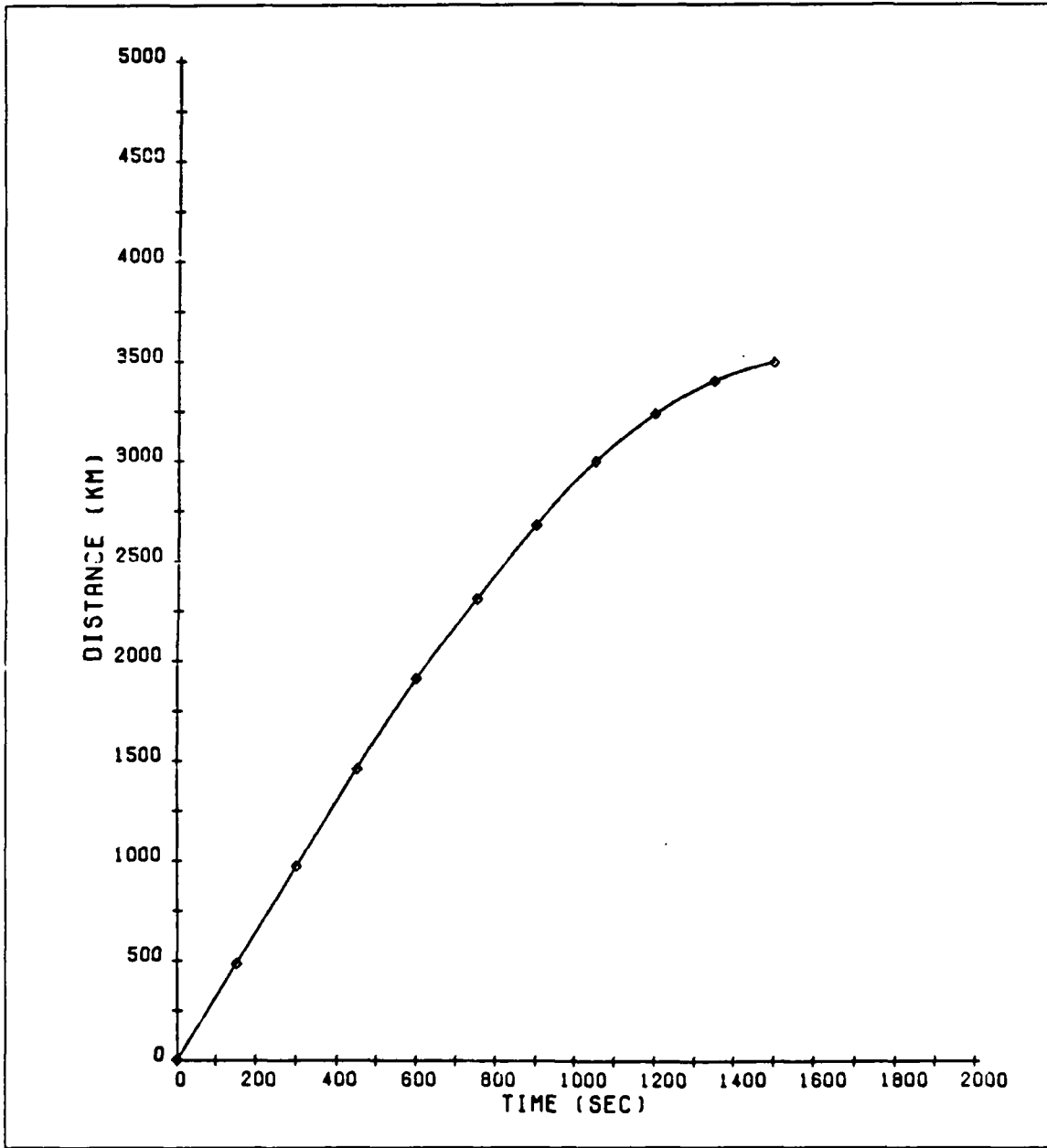


Figure 5.15. Closed-Loop Downrange History for the Nominal Target — No Dispersion Case

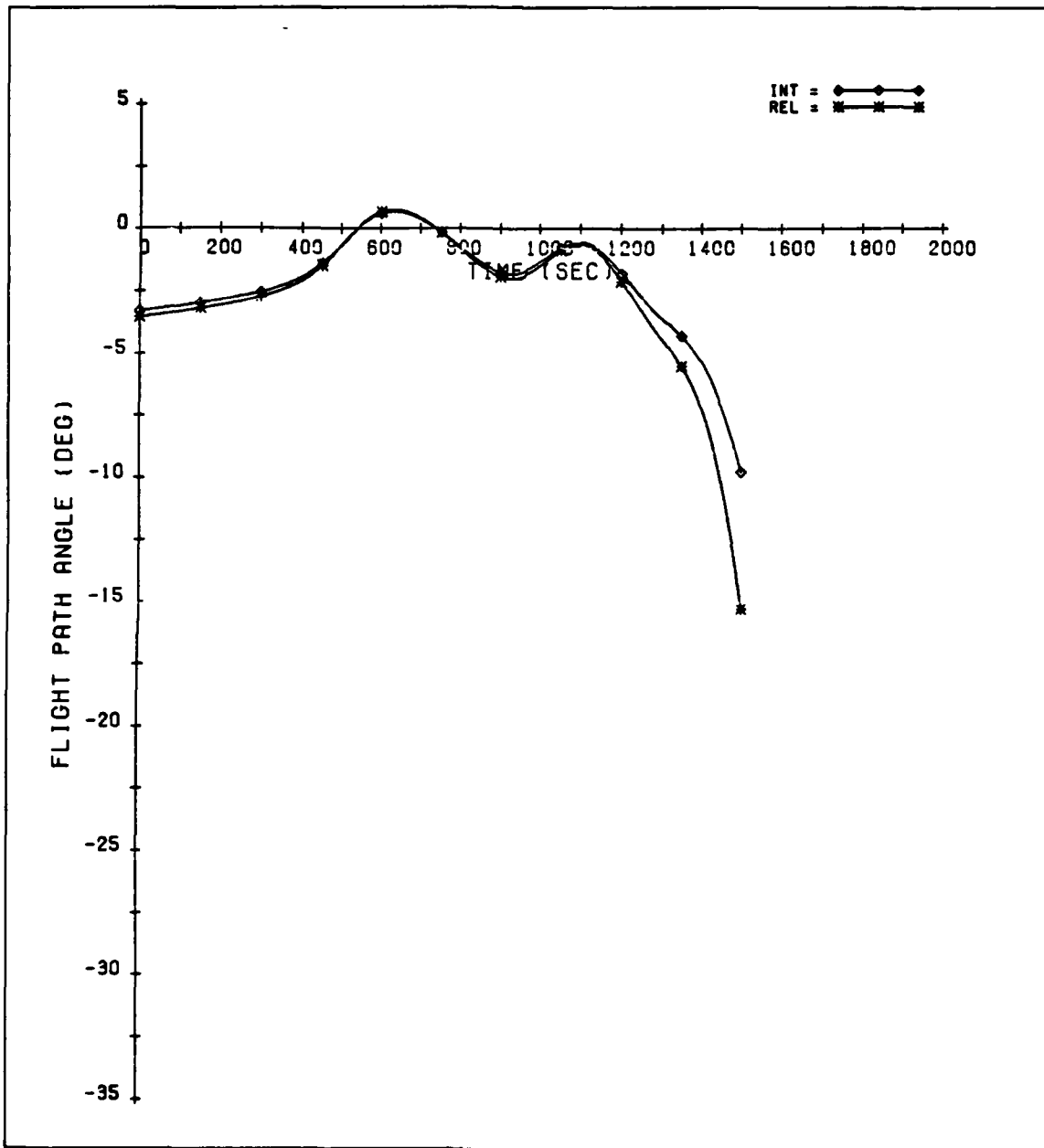


Figure 5.16. Closed-Loop Flight Path Angle History for the Nominal Target — No Dispersion Case

### 5.3 Speed Brake Performance

Since entry vehicles with a high ballistic coefficient tend to have high terminal velocities which guidance can not significantly reduce, the addition of another method of control to the vehicle was considered. The effect of a speed brake, modeled as an increase in the coefficient of drag, on  $\bar{q}_f$  was analyzed. A speed brake deployed early in the trajectory decreases the final dynamic pressure the same as simply decreasing the vehicle design ballistic coefficient. But, since a speed brake can only cause small changes in the effective  $C_B$ , the decrease in the dynamic pressure is limited.

Despite being limited, perhaps the speed brake could serve a useful purpose by cleaning up small final dynamic pressure errors in the dispersed cases. To test this hypothesis, the speed brake was deployed at various velocities in a closed-loop entry trajectory, and the effect of the speed brake on  $\bar{q}_f$  was examined. The entry trajectory was to the nominal target, and the I-loads in Table 5.1 were used.

Because of the phugoid nature of the dynamic pressure, deployment at one velocity was found to cause an increase in  $\bar{q}_f$ , while deployment 200 m/s later in the same trajectory would cause it to decrease. Thus, the sensitivity of final dynamic pressure to velocity of speed brake deployment was found to be highly nonlinear. Due to its limited capabilities and nonlinear effect on dynamic pressure, the speed brake does not appear to be a feasible means of decreasing the final dynamic pressure.

## 5.4 Dynamic Pressure Control Performance

Although Vehicle M was flown at a high angle of attack so as to provide a smaller ballistic coefficient, in the dispersed guidance tests, there were some cases in which  $\bar{q}_f$  still exceeded the limit. The ability of the dynamic pressure controller to reduce these values was tested using the same I-loads as in Table 5.1 with the exception that  $V_{dmp}$  was no longer zero, but set to 3000 m/s. The results can be seen in Table 5.7.

Table 5.7. Dynamic Pressure Controller Results

Case		Original Value		Controlled Value	
Target	Dispersion	$\bar{q}_f$ (N/sq m)	$DR_e$ (km)	$\bar{q}_f$ (N/sq m)	$DR_e$ (km)
NOM DR	$\rho^-$	1012	0.32	964	0.09
MIN DR	$\rho^-$	1202	-0.58	1040	-0.03
MIN DR	$\gamma_{ei}^+$	1152	0.32	950	3.52
MAX CR	$\rho^-$	1006	-0.32	976	0.38

Of the four dispersed cases in which  $\bar{q}_f$  was originally exceeded, the controller was successful at reducing the final dynamic pressure below the limit for three of them. To demonstrate that the controller functioned as designed, the dynamic pressure histories for the damped and undamped trajectories to the nominal target in a 50% thin atmosphere are presented for comparison in Figure 5.17. It can be seen that the controller damped out the oscillations which resulted in a lower final value.

In the third case in Table 5.7—the minimum downrange, shallow entry flight path angle trajectory—the final dynamic pressure was reduced within limits at the cost

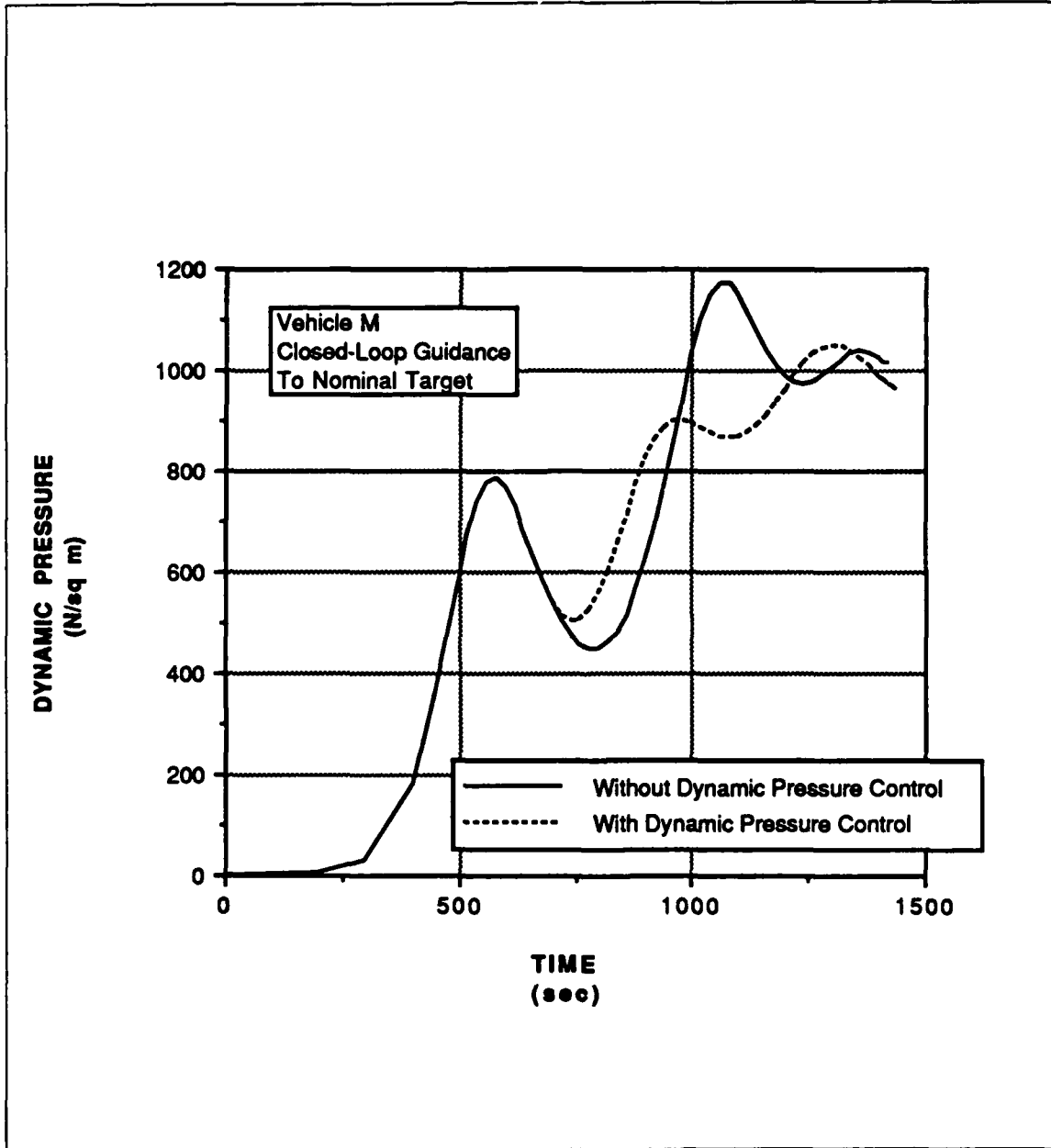


Figure 5.17. Dynamic Pressure Response: Damped and Undamped Trajectories

of violating the downrange constraint. This demonstrates the limitation of using only one variable to control three constraints. In the second and unsuccessful case—the minimum downrange, thin atmosphere trajectory—the controller was unable to bring  $\bar{q}_f$  within limits because the original final dynamic pressure was so high. The final value was reduced by over 150 N/sq m, but because final dynamic pressure is relatively insensitive to bank angle, the controller can only do so much. Further tests using different vehicles with higher ballistic coefficients produced similar results. The dynamic pressure controller was able to damp the phugoid, but the “steady-state” dynamic pressure value, which is determined by vehicle design, was not reduced, and the 1000 N/sq m limit was still exceeded.

The dynamic pressure controller is limited because it trades ranging performance for dynamic pressure control, and because it is unable to make large reductions in  $\bar{q}_f$ . The inability to greatly reduce  $\bar{q}_f$  means that vehicle design is the key to making significant reductions without resorting to some other method of control. Given a vehicle design which has a reduced ballistic coefficient, the ability of the controller to consistently hit the target while limiting  $\bar{q}_f$  is called into question by the necessary trade-off. Although the dynamic pressure controller performs as designed, active control of the final dynamic pressure using bank angle only is not promising.

## 5.5 Estimator Performance

The performance of the density and L/D estimators in the prediction is important for ensuring guidance accuracy in the presence of dispersions. A guidance which has good

estimates of its environment and vehicle performance is able to adapt to unpredicted variations. Good estimates increase the guidance margin and expand the edges of the achievable footprint in the presence of dispersions.

The performance of the two estimators is demonstrated using an entry case with +10%  $C_L$  dispersions and a Viking 1 atmosphere. The density estimator response using a time constant of 20 seconds in the low-pass filter is shown in Figure 5.18. The figure shows the actual density ratio,  $K_\rho$ , and the predictor estimate of the density ratio as a function of time. Estimation does not begin until approximately 400 seconds into the trajectory when the sensed acceleration exceeds 0.07 g's. At this point the estimated density scale factor starts driving to the actual value. After reaching the actual value, the density estimator follows all of the general trends in the density. The short-term density variations are filtered out resulting in a smooth density estimate which accurately reflects the density in the atmosphere.

The L/D estimator response in Figure 5.19 is from the same dispersed trajectory, again using a 20 second time constant. Shortly after the estimation begins around 400 seconds, the estimate reaches the actual value. Since the L/D dispersion is constant, the estimate does not vary and reflects the exact value.

Both estimators worked exactly as desired in the previous example; however, winds have an adverse effect on the density and L/D estimates. Figures 5.20 and 5.21 display the time response of the density and L/D filters for the same target and dispersions, but with the addition of 50 m/s crosswinds (0° Wind Direction). As seen in Figure 5.20, approximately halfway through the trajectory, the accuracy of the density

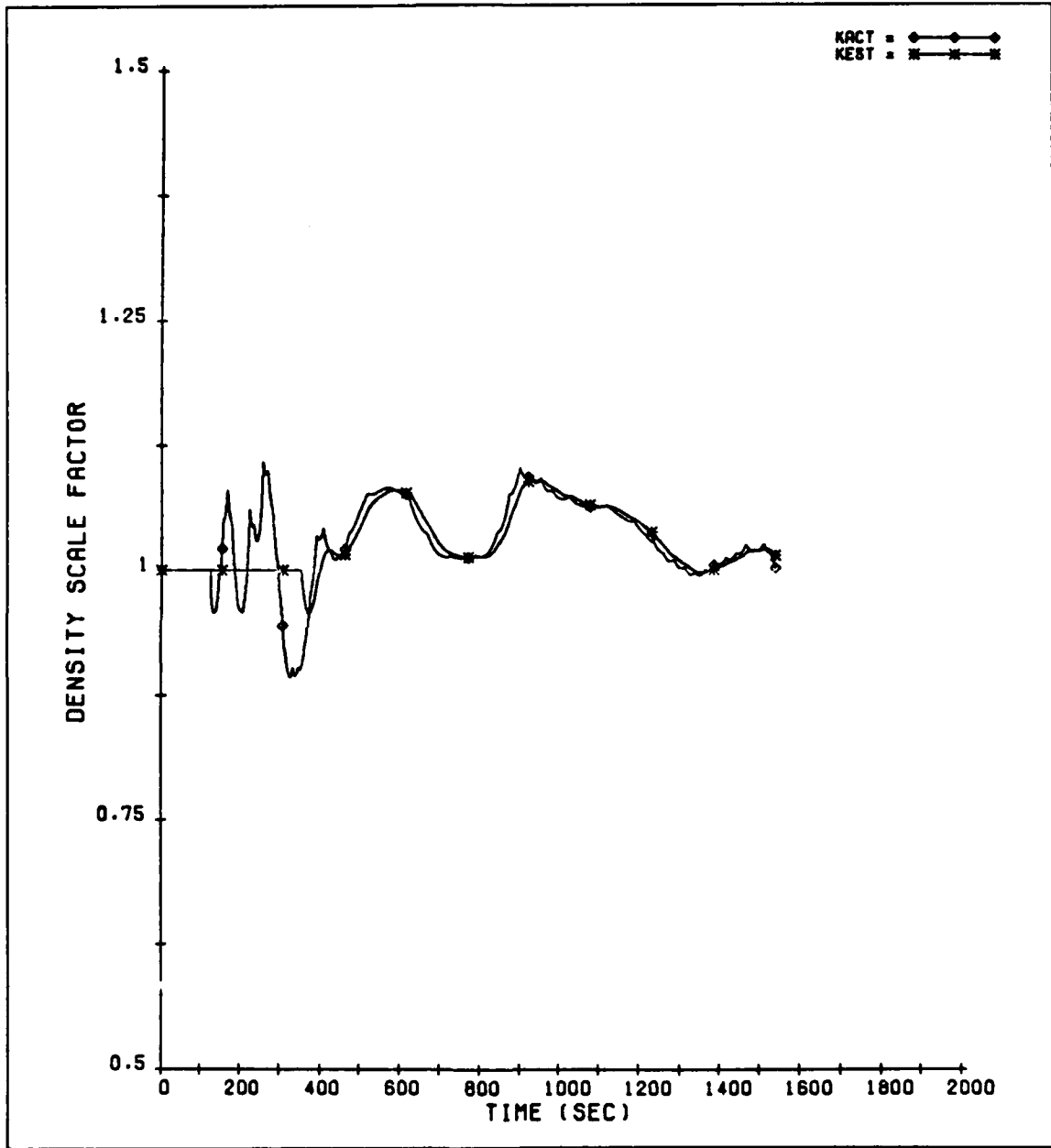


Figure 5.18. Time Response of the Density Filter: No Wind Case

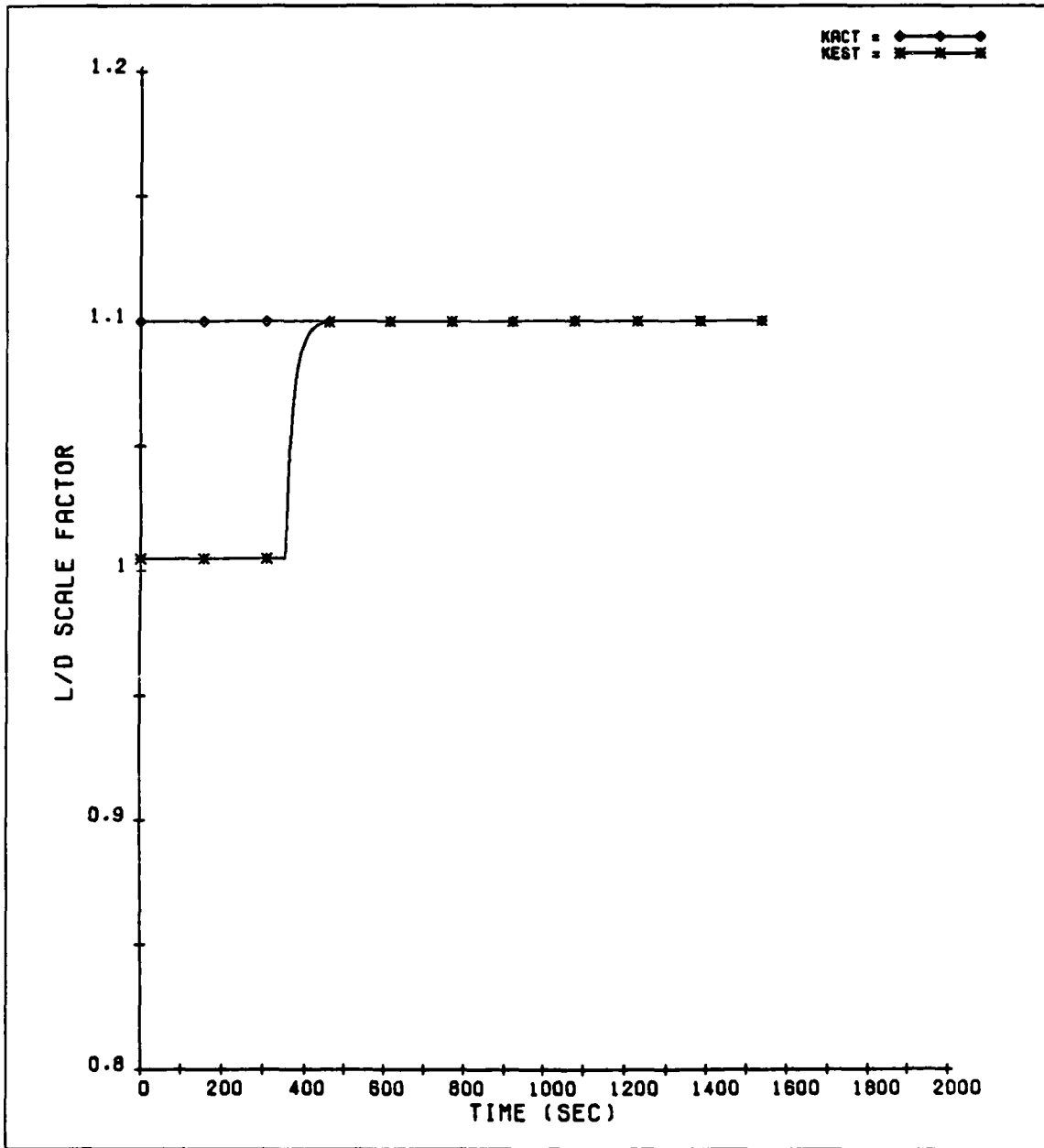


Figure 5.19. Time Response of the L/D Filter: No Wind Case

estimate begins to decrease. The estimate deviates from the actual density and alternates between being high and low. The source of this deviation is the wind, and the alternation is due to roll reversals. Wind induces an error in the navigation relative velocity because the model used to determine  $v_{rel}$  does not contain winds. Since the measured density is derived from the nominal ballistic coefficient, accelerometer measurements, and  $v_{rel}$ , wind also causes an error in the density estimates. The error in the density estimate switches sign after a roll reversal because the contribution of the wind to the relative velocity changes with the vehicle attitude. For example, the density estimate in Figure 5.20 changes from high to low around 1450 seconds as the vehicle changes direction and reduces the headwind. The error in the density estimate does not become noticeable until later in the trajectory because the relative error in  $v_{rel}$  increases as the vehicle slows down. Although the density estimate error grows, the impact of this error on downrange performance is negligible as the error is never very large and is frequently changing signs with each roll reversal.

The L/D estimator response in Figure 5.21 is for the wind dispersed trajectory, again using a 20 second time constant. Since the measured L/D is determined using the drag and lift acceleration computations which utilize  $v_{rel}$ , the error in the estimate can also be traced to errors in  $v_{rel}$ , and thus to winds. The L/D estimator performance is similar to the density estimator performance. Each roll reversal causes a change in the sign of the error in the L/D estimate, and the average error in the estimate throughout the trajectory is near zero. Also, the error in the L/D estimate grows as the velocity decreases. However, the error in the L/D estimate is more pronounced

and is exhibited earlier than the error in density estimate. This can be traced to the fact that the measured density is based on the sensed drag acceleration and  $v_{rel}$ , whereas the measured L/D is based on the sensed drag acceleration and the sensed lift acceleration. Since the measured lift acceleration requires both the magnitude and direction of  $v_{rel}$ , its error due to winds is greater than that simply present in the magnitude of  $v_{rel}$ .

If wind speed and direction could be measured using an on-board sensor and incorporated into the navigation-derived relative velocity so that  $v_{rel}$  more accurately reflected reality, the response of the two estimators with wind could be similar to the response in the no wind case.

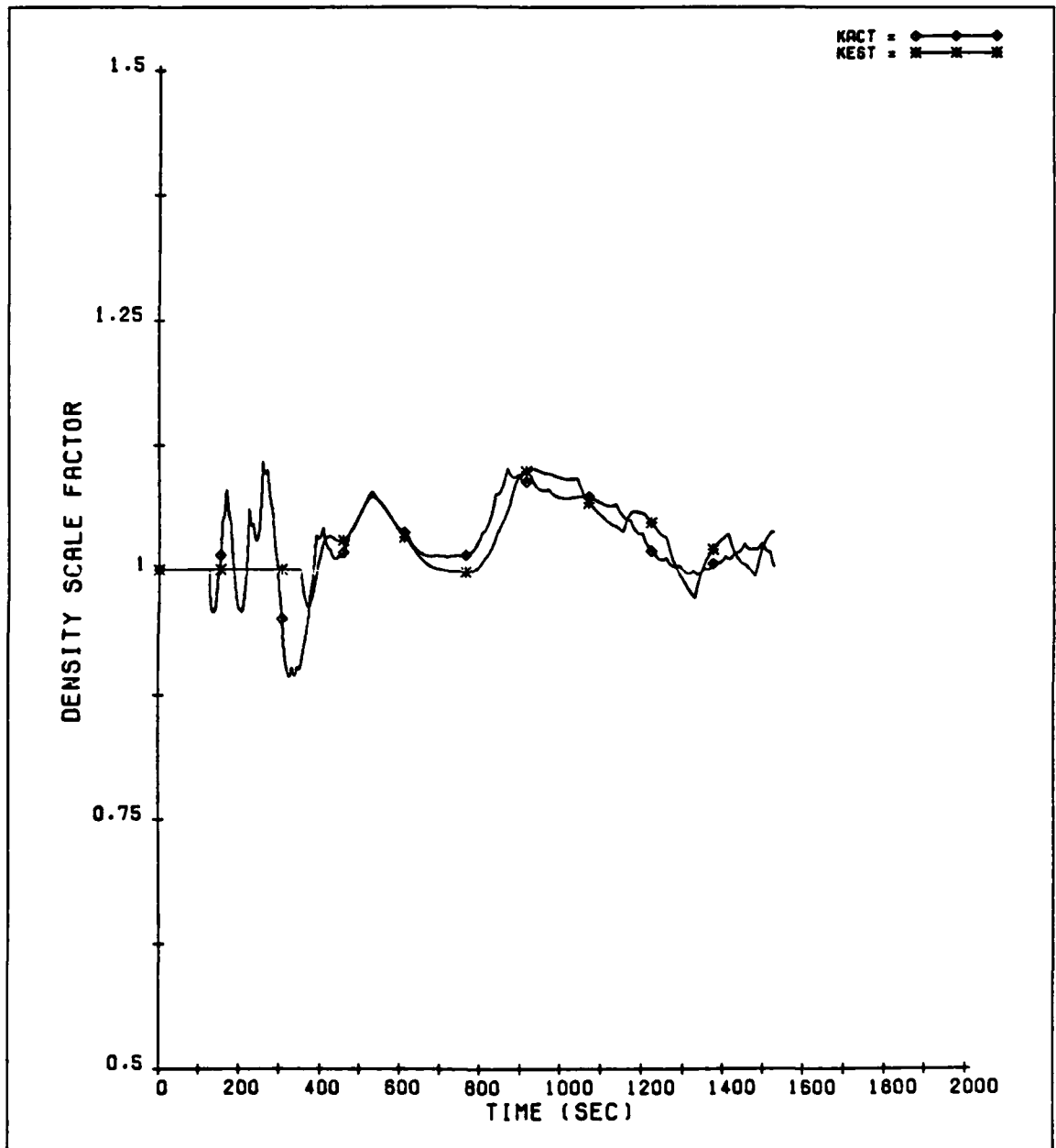


Figure 5.20. Time Response of the Density Filter: Wind Case

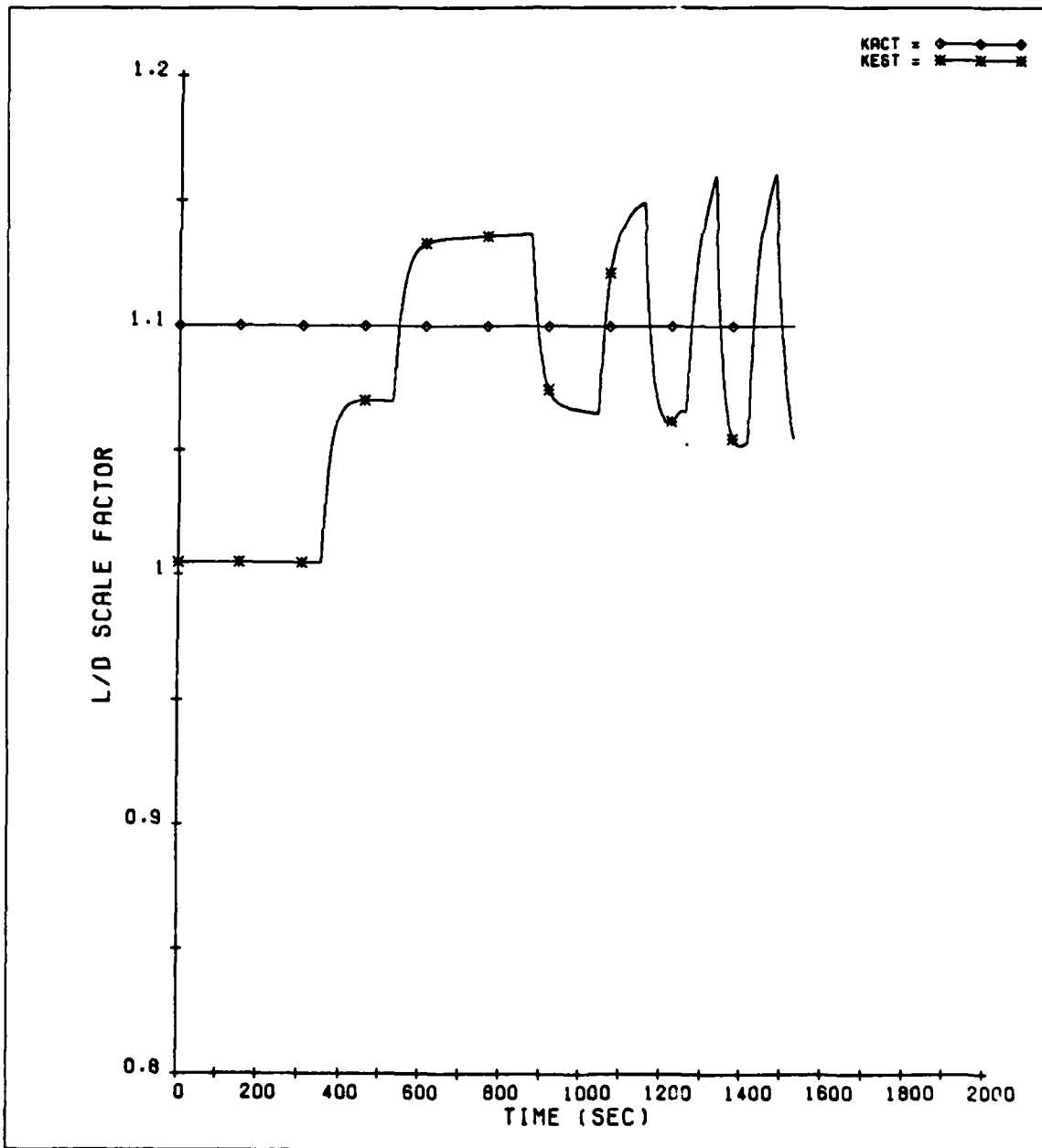


Figure 5.21. Time Response of the L/D Filter: Wind Case

# Chapter 6

## Conclusions

### 6.1 Summary of Results

The goal of this study has been to examine the precision entry problem at Mars. Various factors in entry vehicle performance at Mars were first investigated in order to determine basic vehicle design requirements. The second part of the study presented a guidance algorithm for achieving precision entry with a mid-L/D vehicle using bank angle control only.

The basic goals for vehicle design are high lift-to-drag ratio and low ballistic coefficient. A high L/D was shown to increase ranging capability as well as reduce the final dynamic pressure. While a high L/D is desired, the marginal mission flexibility gained by increasing L/D beyond 1.5 is small. An L/D of 1.4 is needed to achieve crossranges approaching 1000 km, although a lower value is sufficient to reach an in-plane landing site.

The final dynamic pressure was found to be almost linearly dependent upon the vehicle ballistic coefficient. For a vehicle with an L/D of 1.0, a ballistic coefficient less

than 300 kg/sq m is necessary to keep the final dynamic pressure below 1000 N/sq m. Because of the thin Martian atmosphere, the ballistic coefficient which will ensure that the final dynamic pressure limit is not exceeded at Mars is significantly less than the necessary ballistic coefficient for Earth entry. Since decreasing the ballistic coefficient generally involves decreasing the L/D, a trade-off must be made between range and final dynamic pressure.

The same trade-off must be made once a vehicle has been chosen. Given a vehicle, it is possible to significantly alter performance by changing the trim angle of attack, as this varies the effective lift-to-drag ratio and ballistic coefficient. It was shown that a vehicle should not necessarily fly at the trim angle of attack providing maximum L/D if final dynamic pressure is a concern. The ranging capabilities must be sacrificed to reduce the final dynamic pressure.

The conclusion drawn from the short divert study was that there is sufficient control margin to divert an entry vehicle to reasonable alternative sites if the decision to divert is made early enough. This study was done with a low performance (L/D = 0.85) vehicle, and higher lift-to-drag ratios will increase the divert footprint. This conclusion must be tempered with an understanding that the study assumed nominal conditions, and adverse density dispersions will reduce the divert capability of the vehicle.

Entry flight in the thin Martian atmosphere with a low-to-mid L/D vehicle was shown to exhibit a large phugoid response in dynamic pressure which makes continuous and final constraint control difficult. The entry guidance presented here steers the

vehicle based on a reference bank profile which is linear with velocity. The particular reference bank profile that will allow the vehicle to reach the target in downrange is determined by a numeric predictor-corrector algorithm. The guidance also utilizes roll reversals based on the vehicle heading in order to control the final crossrange. Additionally, an analytic control law is superimposed on the linear bank profile to reduce the oscillations in the dynamic pressure, and thus reduce the final dynamic pressure.

The guidance was shown to provide near-maximum crossrange performance and almost complete coverage of the possible footprint. It was tested in the presence of dispersions and demonstrated the ability to handle them well. This adaptability is achieved by using in-flight measurements to increase the accuracy of the predictions.

Through the guidance testing, an entry vehicle with  $L/D = 0.85$  and  $C_B = 282$  kg/sq m was shown to have the control authority necessary to reach the target with high precision. With this vehicle, the other major constraint, final dynamic pressure, was kept within limits in most all cases. However, it must be noted that if a higher ballistic coefficient vehicle is used, the guidance is able to damp the oscillations in dynamic pressure, but it is unable to significantly reduce the final value. Therefore, the necessity for a second method of control, specifically angle of attack modulation to reduce the final dynamic pressure, depends on the vehicle design. If the vehicle design passively reduces the final dynamic pressure through the proper selection of ballistic coefficient and trim angle of attack, then no other method is necessary. But, if the vehicle design is driven solely by factors other than guidance—such as weight

and packaging—resulting in a relatively high ballistic coefficient, bank angle control alone is limited and a second method of control will probably be required.

## 6.2 Future Research

Much more research is necessary prior to the development of a flight-quality Mars precision entry guidance algorithm. One of the major steps that must be taken is the definition of specific mission requirements. Once specific requirements have been defined, further work should address possible improvements and testing of the proposed algorithm.

There are several areas in which guidance performance could be enhanced. The incorporation of wind measurements into the navigation estimate of relative velocity would provide better estimates of the L/D and density, and result in more accurate predictions. Better predictions would increase the guidance accuracy, or allow the guidance to be run at a slower rate. Crossrange and dynamic pressure control would also be strengthened by the wind measurements because relative velocity is used in these computations, too. The effect that such measurements, provided by an air data system, have on performance must be analyzed to determine whether the expense of adding the system is worthwhile.

Additionally, the computational requirements of the algorithm can be decreased. The predictor step size and the corrector execution rate should both be optimized to provide reduced computational loads.

The analysis in this thesis could be improved by using the only recently available

Mars GRAM 89 atmosphere [20], as it provides wind and density shear models which are much better than the models used here. The guidance could also be further tested by undertaking a complete guidance-navigation systems study. In this study, the interaction of the guidance with navigation updates from external aids such as beacons, as well as the sensitivity of the guidance to navigation errors, would be investigated.

Prior to the development of a specific vehicle or mission, work can be done regarding the effectiveness of modulating angle of attack in reducing final dynamic pressure. If angle of attack can effectively control the final dynamic pressure, the vehicle designers may choose to provide a means of varying angle of attack so that the vehicle can be built with a high ballistic coefficient.

Additionally, a separate, more complete, study focusing on divert capabilities should be accomplished. Using different vehicle configurations, the ability to divert would be tested with various targets in the presence of dispersions.



# Bibliography

- [1] Gamble, J.D. (ed.), *JSC Pre-Phase A Study: Mars Rover Sample Return Mission Aerocapture, Entry, and Landing Element*, Johnson Space Center, Houston, Texas, May 1989.
- [2] *Human Exploration Study Requirements*, NASA Technical Study Group Report, September 8, 1989.
- [3] Euler, E.A., Adams, G.L., and Hopper, F.W., "Design and Reconstruction of the Viking Lander Descent Trajectories", *Journal of Guidance and Control*, Vol. 1, No. 5, September-October 1978.
- [4] Kerzhanovich, V.V., "Mars 6: Improved Analysis of the Descent", *Icarus*, Vol. 30, 1977.
- [5] Tigges, M.A., and Ling, L.M., "A Predictive Guidance Algorithm for Mars Entry", AIAA Paper 89-0632, AIAA 27th Aerospace Sciences Meeting, Reno, Nevada, January 1989.
- [6] Cruz, M.I., and Mease, K.D., "Generic Aerocapture: Trajectory Guidance and Navigation", Jet Propulsion Laboratory, Pasadena, California, presentation to Inter-NASA Centers Review Panel, February 25-26, 1982.
- [7] *Final Report: Mars Rover Sample Return (MRSR) Program Aerocapture, Entry, and Landing (AEL) Conceptual Study*, Martin Marietta Aerospace Group, Denver, Colorado, September 1988.
- [8] Kaplan, David (ed.), *Environment of Mars, 1988*, NASA Technical Memorandum 100470, October 1988.
- [9] Fuhry, D.P., *A Design Study of Onboard Navigation and Guidance During Aerocapture at Mars*, S.M. Thesis, Dept. of Aeronautics and Astronautics, Massachusetts Institute of Technology, May 1988.

- [10] Spratlin, K.M., *An Adaptive Numeric Predictor-Corrector Guidance Algorithm For Atmospheric Entry Vehicles*, S.M. Thesis, Dept. of Aeronautics and Astronautics, Massachusetts Institute of Technology, May 1987.
- [11] Wagner, W.E., "Roll Modulation for Maximum Re-Entry Lateral Range", *Journal of Spacecraft*, Vol. 2, No. 5, September-October 1965.
- [12] Zondervan, K., Bauer, T., Betts, J., and Huffman, W., "Solving the Optimal Control Problem Using a Nonlinear Programming Technique Part 3: Optimal Shuttle Reentry Trajectories", AIAA Paper 86-0270, AIAA 24th Aerospace Sciences Meeting, Reno, Nevada, January 1986.
- [13] Wingrove, R.C., "Survey of Atmospheric Re-Entry Guidance and Control Methods", *AIAA Journal*, Vol. 1, No. 9, September 1963.
- [14] Ess, R.H., and Munday, S.R., "Aerodynamic Requirements for a Mars Rover Sample Return Aerocapture Vehicle", AIAA Paper 89-0630, AIAA 27th Aerospace Sciences Meeting, Reno, Nevada, January 1989.
- [15] Bauer, S., "Deorbit/Entry Navigation Performance", *1989 Lunar/Mars Initiative Guidance, Navigation, and Control Final Report*, CSDL-P-2932, February 1990.
- [16] Morth, R., *Reentry Guidance for Apollo*, MIT Document R-532, January 1966.
- [17] Harpold, J.C., and Graves, C.A. Jr., "Shuttle Entry Guidance", *The Journal of the Astronautical Sciences*, Vol. XXVII, No. 3, July-September 1979.
- [18] Gamble, J.D., Cerimele, C.J., Moore, T.E., and Higgins, J., "Atmospheric Guidance Concepts for an Aeroassist Flight Experiment", *The Journal of Astronautical Sciences*, Vol. 36, Nos. 1/2, January-June 1988.
- [19] Ingoldby, R.N., "Guidance and Control System Design of the Viking Planetary Lander", *Journal of Guidance and Control*, Vol. 1, No. 5, September-October 1978.
- [20] Justus, C.G., Chimonas, G., and Johnson, D.L., *The Mars Global Reference Atmospheric Model (MARS-GRAM)*, Georgia Tech Project G-35-685, July 1989.